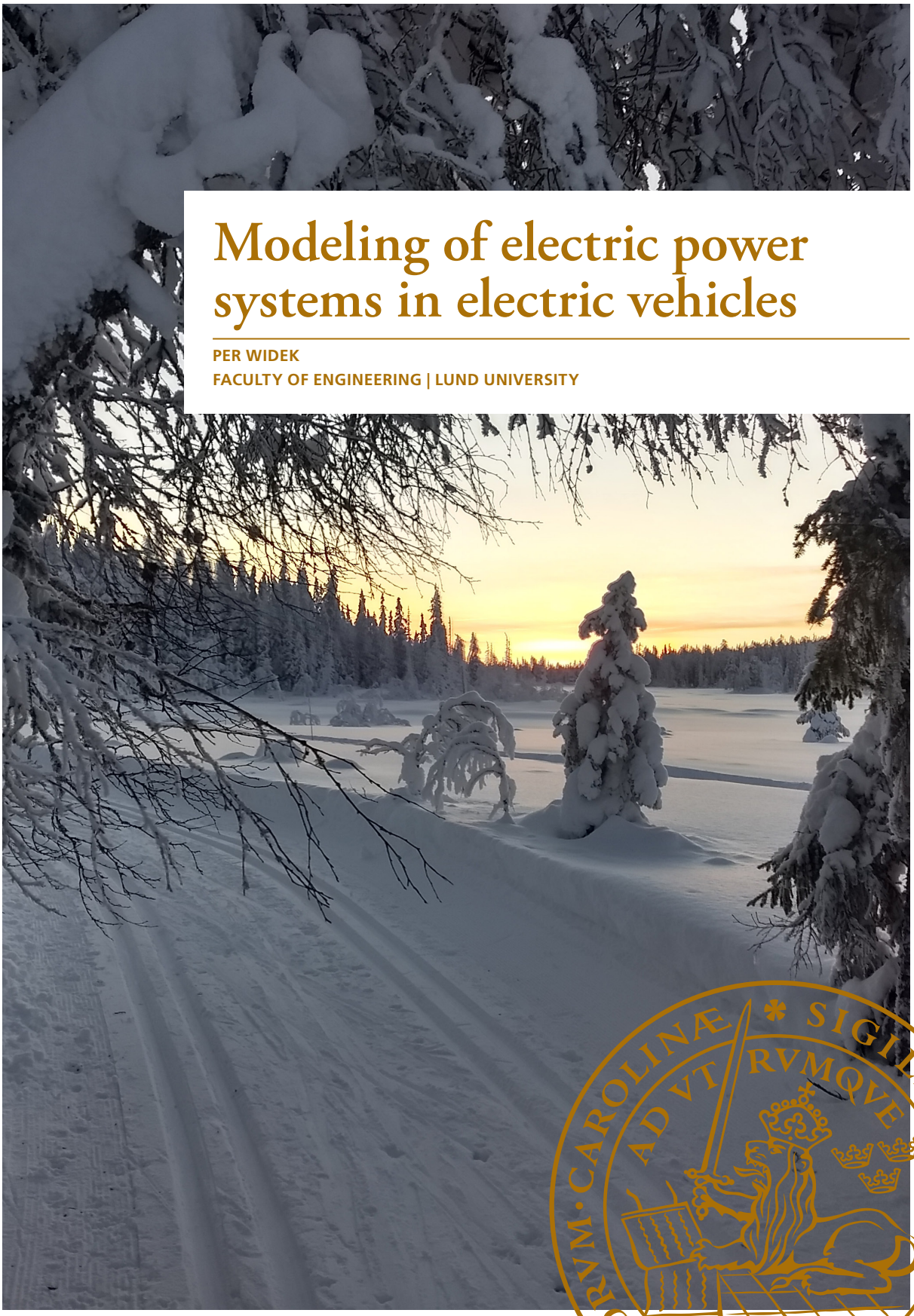

Modeling of electric power systems in electric vehicles

PER WIDEK
FACULTY OF ENGINEERING | LUND UNIVERSITY

Modeling of electric power systems in electric vehicles

Modeling of electric power systems in electric vehicles

by Per Widek

LUND
UNIVERSITY

Licenciate Thesis
Thesis advisors: Prof. Mats Alaküla, PhD Hans Bängtsson
Faculty opponent: PhD Urban Lundgren

Akademisk avhandling om 120 poäng som för avläggande av Teknisk Licentiatexamen i Industriell Elektroteknik vid tekniska fakulteten vid Lunds Universitet kommer att presenteras i sal KC:A, K-huset, Sölvegatan 39, Lund, Fredagen den 4 februari, 2022, kl. 10:15.

Organization	Document name
LUND UNIVERSITY Department of Biomedical Engineering Box 118 SE–221 00 LUND Sweden	**LICENTIATE DISSERTATION** Date of disputation 2022-02-04 Sponsoring organization Volvo Group
Author(s) Per Widek	

Title and subtitle

Modeling of electric power systems in electric vehicles:

Abstract

The market for partly or fully electrified vehicles is expanding fast. The number of sources and loads that are connected to the vehicles traction voltage systems (TVS) increase and thus also the ElectroMagnetic Compatibility (EMC) requirements on these sources and loads. These requirements should make sure that neither function nor lifetime of any source or load is severely affected by another. The EMC requirements include both Common Mode (CM) and Differential Mode (DM) voltages and currents created by the modulation of the various power electronic converters involved as well as intentional and parasitic impedances of the TVS and reach up to at least 10MHz for CM and 100kHz for DM. This paper presents a theory for the dimensioning of CM-capacitances in an Electric Machine Drive (EMD) that is confirmed by measurements on a commercial electrical Volvo truck. The conclusions point out a recommendation for selection of the CM-capacitances of the EMD vs. the CM capacitance of the Electrical traction Machine (EM). As a rule of thumb the recommendation is that the CM-capacitance of the EMD is around 50 times the CM-capacitance of the EM and mounted inside the EMD to avoid big loops of CM currents in the vehicle.

Key words

DC-AC power converters, Electromagnetic compatibility, Electromagnetic interference, Electromagnetic modeling, Harmonic analysis, Harmonic filters, Parasitic capacitance.

Classification system and/or index terms (if any)

Supplementary bibliographical information	Language
	English
ISSN and key title	ISBN
	978-91-985109-2-8 (print) 978-91-985109-3-5 (pdf)
Recipient's notes	Number of pages: 125 / Price
	Security classification

Modeling of electric power system in electric vehicles

by Per Widek

LUND
UNIVERSITY

Cover illustration front: Myrflodammen in Sälen
(Credits: Per Widek).

Funding information: The thesis work was financially supported by
Volvo Group Trucks Technology AB.

Faculty of Engineering
Department of Biomedical Engineering
Division of Industrial Electrical Engineering and Automation

ISBN: 978-91-985109-2-8 (print)
ISBN: 978-91-985109-3-5 (pdf)
CODEN: LUTEDX/(TEIE-1094)/1-125/(2022)

Printed in Sweden by Media-Tryck, Lund University, Lund 2022

Om du inte kan förklara det enkelt, så förstår du det inte tillräckligt bra.
If you can't explain it simply, you don't understand it well enough.
Albert Einstein

Contents

Acknowledgements

Finally, when Christmas approaches it is time for the final words in my thesis. I started this day shoveling 20 cm of snow, not a common Friday in Gothenburg. It is a great Christmas gift to me, that the thesis is finalized, and I can spend time with my family and friends without feeling stressed, change focus, go skiing, bottle the glögg, and make other preparations for Christmas. Looking back at the last three and a half years the time just disappeared. Having the opportunity to meet a lot of people in the same area, surprisingly many acquaint from old times from ASEA and Adtranz. We are not so many working in this area. We meet occasionally and it is an honor to share experiences. I am looking forward to many years together on the road ahead towards the green conversion to electromobility.

I would like to express gratitude to all those who helped me with my thesis.
Mats Alaküla, professor at LTH, has been and will continue as my main supervisor. Mats has been at my side from day one even though we were colleges since before. Mats is positive, solution-oriented, and most importantly, always encouraging. Thank you Mats, I look forward to continuing working with you.

Hans (Trisse) Bängtsson, an old college from Adtranz. I spent a few years in Philadelphia with a suburban tram delivery to a customer. Many challenging problems to solve and Trisse always supported me from Sweden. ”Per, this is how it works!” A mine of knowledge, and I am so grateful to have Trisse as my co-supervisor.

The reference group is a fantastic group of people and I cannot wish for a better one. Different personalities that contribute in different aspects. Sabine (Mäthäxan) Alexandersson is an EMC specialist working at FMV. I was honored when she accepted to be part of my reference group and she has contributed a lot with expertise. Sabine has been as important for keeping the scope concrete. I am also grateful for all her telephone calls when she realized that I felt low. Anders Lasson, system is a specialist at Volvo cars. Anders is encouraging and has the most tricky yet very valid questions. Jonas Ottosson, specialist within power electronic converter. Jonas is always helpful and contributes with ideas and questions. A small question from Jonas resulted in a patent application. Zhe Huang, specialist within electrical machines. Zhe is always positive and has taken my ideas into the projects at Volvo which I am truly grateful for.
I am also grateful to my manager Martin Norén for supporting with everything around that is necessary. Without my colleagues at Volvo, I would not have come to the (these?) results. Marinko Culjak who always arranged a slot in the back to back rig even when not possible. Tommy Strömborg who supported me with the vehicle measurements but also with the new measurement system. Marco Lind, previous manager at Volvo Buses and at Volvo GTT, he encouraged me to start studying ”Chalmers professionals” which later led to that I dared to take the step to become a PhD student. David Hellstedt, previous head of Volvo Electromobility. David encouraged me to start the PhD study and gave me the

prerequisites in terms of financing from Volvo.
Clas Nender at KEMET has supported me in my thoughts of system aspects when connecting one subsystem with many and how they interfere with each other. During the covid-19 short term layoff I wrote an internal report of the life-length effect on capacitors from current ripple. Clas supported me with his expertise in the area.
The entire staff in Lund should of course be acknowledged. Without Carina Lindström I would have missed many important things. Fransisco Marquez who invited me as speaker to interesting meetings at Swedish Electromobility Center. Philip Abrahamsson who was the co-supervisor for my first master thesis workers. Anton Karlsson, Ulf Jeppsson and all other colleagues who make me feel welcome every time I am in Lund.

Magnus Pihl is a former classmate from Chalmers, former college from ABB but most importantly a good friend. We had many fruitful discussions and, as he is working for Micropower, a potential supplier, he contributed with new insights from the supplier point of view.
Maria Hammarquist and Tobias Bergsten at RISE supported me with knowledge in the sensor area. Urban Lundgren at RISE has always been supportive and helped med discussing cable models as one example.
Torbjörn Thiringer, professor at CTH, frequently invites me to interesting meetings and sometimes as guest speaker. Torbjörn has also supported me with master thesis workers from CTH.
Lisa Alaküla, Mats' wife, who let me spend time in their home to work with Mats, and who also became a good friend.
Jonas Cognell, Bengt Norberg, Tomas Borlid, Chalmersgänget, old skydiving friends and many more friends are so important to me. Skiing, kayaking, dinners and visiting theaters are some activities I enjoy doing with you.

Finally. My lovely children, Ida och Tor. *Ni betyder allt för mig. Ni skulle bara veta hur mycket jag älskar er och inget är viktigt i jämförelse med er. Jag hoppas att få spendera mer tid framöver med dig Ida. Älskar dig!*. My sister Eva who supports me with everything.
With love to my father Bertil who passed away, at the age of 95, between the licentiate presentation and the printing of this book. He encouraged me all the time. He translated my first paper with google translate and was looking forward to translate this book as well. The last weekend we met, we celebrated with champagne. My mother Gunvor died during my first year as PhD student. Love you!

Nomenclature

BB	Body Builders
BEV	Battery Electric Vehicle
BoB	Break Out Box
BW	Band Width
C	Capacitance
CAN	Controller Area Network
Ch	Channel
CM	Common Mode
CMDC	Common Mode DC
DCDC	Converter from DC to DC
DM	Differential Mode
DUT	Device Under Test
DYNO	Dynamometer
EM	Electrical Machine
EMC	Electromagnetic compatibility
EMD	Electrical Machine Drive
EMI	Electromagnetic Interference
ePTO	electrical Power Take Out
EV	Electric Vehicle
Gen	Generator
HEV	Hybrid Electric Vehicle
HF	High Frequency
HV	High Voltage
HVAC	High Voltage Air Condition
IAI 2	Impedance Analysis Interface 2
IGBT	Insulated Gate Bipolar Transistor
IP	Intellectual Property
JB	Junction Box
L	Inductance
LCR	Inductance Capacitance Resistance
OEM	Original Equipment Manufacturer
OnBC	On Board Charger
PCI	Peripheral Component Interconnect
PEC	Power Electronic Converter
PHEV	Plug-in Hybrid Electric Vehicle
PMSM	Permanent-Magnet Synchronous Machine
PSM	Phase Sensitive Multi-meter
PXI	PXI (PCI eXtensions for Instrumentation)
R	Resistance

SC	Short Circuit
SiC	Silicon Carbide
TVS	Traction Voltage System

Chapter 1

Introduction

The evolution of hybrid vehicles (HEV), plug-in hybrid electric vehicles (PHEV) and battery electric vehicles (BEV) is accelerating. New models are developed at an increasing rate and to reduce development time it is necessary to be able to predict the functioning of the electric power system, not least from an Electro Magnetic Interference (EMI) point of view. In the simplest form the drive-train consists only of some power electronic converters (PEC) supporting the electrical traction machine (EM), the traction battery and possibly a compressor in commercial vehicles. There also exists more advanced system layouts with multiple traction machine drives, DC/DC converters supplying power to the 24V system, electrically driven auxiliary equipment and chargers connected to the grid. Merging the included subsystems, that here is referred to as the Traction Voltage System (TVS), to a common system is a challenge as system knowledge is crucial for predicting the performance. The individual subsystems should not create a DC link current ripple, e.g., Differential Mode (DM) currents, and should not create Common Mode (CM) currents high enough to disturb other subsystems or decreasing other subsystems life length.

The included subsystems are in general sourced from different suppliers. A good traction voltage system knowledge is therefore needed at the OEM to set the correct requirements on the subsystems to safeguard the system properties.

The purpose with the study presented in this thesis is to, by modeling, simulation and measurements, build understanding and confirm models to predict the traction system behavior from a High Frequency electric viewpoint. This understanding can be used in the design phase of the vehicles electric power systems and then ensures that the vehicle is properly designed and works as intended as a re-design of a vehicle takes time, a lot of resources and is expensive. Comparing electric cars and electric commercial vehicles, there are two main differences in the power-train: power level and the number of installed nodes. The electric power system of a battery electric commercial vehicle has multiple energy sources and loads. Examples of such are several different traction battery packs, multi traction machine drive-trains (maybe with several driven axles), DC/DC converters, connections to

the grid via on board or off board charging systems, connections to electric road systems, to body builder equipment, to AC power outlets in ”island mode”, to other vehicles etc. All commercial vehicle manufactures needs to meet the challenge of designing large electric power systems and make these function properly in any operating condition. However, no company publish their design and simulation models of the electric power system as it is an intellectual property (IP). This thesis is sharing some of the knowledge and experiences drawn from building and by measurements calibrating a traction voltage system model library of the DM and CM behavior of a very large traction voltage systems in full electric commercial vehicles as indicated above. The ambition is that the simulation models should be valid up to at least a few MHz. The level of detail needed to represent the electric behavior well up to the MHz range is high and make the simulation time consuming if e.g., a significant part of a drive cycle, like an acceleration, needs to be simulated. In is shown in this thesis that the detailing of the DM and CM models may have to be different to facilitate reasonable simulation times.
The validation through measurements sets high demands on the measurement system both in terms of bandwidth and number of channels. At the time of doing the work behind this thesis, no system was available on the market and a development of an extensive measurement system is included in this thesis. The speed of electrification is accelerating and the demand on time to market as well as many new models of vehicles sets demands on the engineering process. It is necessary to be able to perform simulations rather than full vehicle measurements to ensure the EMC performance.

1.1 Goal, Objective and Scope

The goal of the work presented in this thesis is to build a solid understanding of how DM and CM voltages and currents are generated in the traction voltage system of a class B vehicle, how they spread and make different subsystem interfere and how this interference can be limited to a level that do not endanger the intended functionality of the vehicle.

The Objective is to share the understanding by providing design rules and software tools that can be used in predicting the TVS functionality from an EMC/EMI point of view already at the vehicle design stage, before a vehicle is built.

One Scope is to build simulation models of the electric power system that represent DM in the frequency band 1 kHz-100 kHz and for CM 1 kHz-10 MHz, and to calibrate these models with measurements on a commercial vehicle.

Another Scope is to develop a measurement system that is capable of providing all the measurements needed for the simulation model building.

1.2 Content of the thesis

This chapter 1 presents a brief introduction and the scope of the thesis.
Chapter 2 describes the Traction Voltage System (TVS) in the electric vehicle and the included subsystems, definition of Common and Differential Mode (CM and DM) and how they occur. An important chapter for understanding the thesis as whole.
The concept of modeling from measurement technique to extract the model from measurement is described in chapter 3.
The developed models are used in simulation and the result is presented in chapter 4. The results are compared to theoretical analyze of the cause and effect.
The thesis includes development of a measurement system described in chapter 5.
Chapter 6 shows some results from CM measurements on a truck. The results are compared with the theory from chapter 4. The measurement system has a potential to measure a lot more than it is used for. That will be performed after this thesis towards doctoral thesis.
Chapter 7 is the last chapter in this with thesis and contains conclusions, discussions and the future work after this thesis.

1.3 Previous work (with references)

The included subsystems are in general sourced from different suppliers. A good traction voltage system (TVS) knowledge is therefore needed at the Original Equipment Manufacturer (OEM) to set the correct requirements on the subsystems to safeguard the system properties. The purpose with the study presented in this thesis is to, by modeling, simulation and measurements, build understanding and confirm models to predict the TVS behavior. This understanding ensures that the vehicle is properly designed and works as intended as a re-design of a vehicle takes time, a lot of resources and cost. Comparing cars and commercial vehicles there are two main differences in the power-train; power level and the number of installed nodes. A full electric commercial vehicle has multiple energy sources and loads. Examples of such are several different traction battery packs, multi traction machine drivetrains (maybe with several driven axles), DC/DC converters, connections to the grid via on board or off board charging systems, connections to electric road systems, to body builder equipment, to AC power outlets in ”island mode”, to other vehicles etc. All commercial vehicle manufactures needs to meet the challenge of designing large systems and handle that in a proper way. However no company publish their models as it is an intellectual property (IP). The novelty of this thesis is in sharing some of the knowledge and experiences drawn from a traction voltage system model library built to simulate the CM behavior of very large traction voltage systems in full electric commercial vehicles as indicated above. During development of the models, validation through measurements are performed.

In [13] recommendations for for CM filters upon experimental tests. Return path of Common mode ElectroMagnetic Interference (EMI) noise currents in the motor drive

system in hybrid electric vehicle is shown in [14]. An active common mode voltage compensation device for induction motor drives is shown in [18]. Damping of high frequency leakage currents in Pulse Width Modulation (PWM) inverter Fed AC motor drive system is explained in [17]. Two different models are shown, one is valid for zero sequence. The impact of CM currents in motor bearing currents is discussed in [21] with models of the EM. Effects on common mode active filters in induction motor drives is discussed in [19]. Shielding is an important area and is discussed in [7] if it is necessary or not. This paper shows how the common mode EMI is affected outside the motor drive system between subsystems in the vehicle and recommendations on common mode capacitances and their ratios in the system, affecting the variation of the common mode voltage at the subsystem during switching. Estimation of parasitic components in a system with two conductors and a ground plane [2]. The switching interaction in the power electronics results in ripple causing electromagnetic fields, disturbing other electronics and degradation of components. An overview of this can first be obtained when a physical system is built which could lead to unintentional over- or under dimensioning of HV components [22]. Papers discussing CM EMI and the interactions in electric vehicles are rare.

1.4 Publications and contributions

During the studies, two papers are written where one is presented at the SPEEDAM conference and published [25] and one is under review at IEEE for possible publication [26]. The content of the papers is developed by the author of this thesis. The authoring of the papers is made in cooperation with Mats Alaküla.

Chapter 2

Electric power systems in electric vehicles

Commercial electrified vehicles are available in different variants as hybrid electric vehicle (HEV), plug-in hybrid electric vehicle (PHEV) and pure battery electric vehicle (BEV). This thesis describes only BEV class B voltage system with different charging solutions. The 24V system is not included.

2.1 Traction Voltage System (TVS)

The Traction Voltage System (TVS) is the DC, class B [11], voltage system that connects all traction batteries, electric machines, charging systems, compressor drives, DC/DC converters etc. that are involved in the main power conversion processes on board a commercial electric vehicle. The TVS system operates in the range of 600-700 VDC but varies from system to system depending on the intended battery system voltage but also depending on the state of charge (SOC), the temperature and the power loading of the vehicle. The base for measurements and analysis is a Volvo truck FE280, shown in figure 2.1, which represents the DC system. The power levels of the included systems varies from 5kW to more than 200kW with switching frequencies from a few kHz up to almost 100kHz. Depending of the vehicle the 600V cables can be from 1m to more than 20m in an articulated bus. Using modeling to understand and predict the behavior of the TVS in all operating conditions requires detailed modeling of all subsystems, both with respect to DM and CM aspects. The purpose of the work described in this thesis is to build understanding in the relationship of disturbances as well as giving guidelines to prevent harmful disturbances. This results also in the development of a simulation model library with all relevant subsystems as well as interconnections that are represented in a LEGO ® way, such that a multitude of TVS configurations and parameters can be modeled. The models that are investigated shall be

able to be built with support from suppliers before a delivery to save time.
In the following subsections the most important loads and sources, in figure 2.1, are described. In figure 2.1, the models denoted BP1...4 are battery packs, the DC/DC are converters to 24 VDC, the OnBC are on board chargers, the JB are "Junction Boxes" that are joint connection points, the EMD's are the traction motor converters and the ePTO is an electrically driven mechanical PTO.

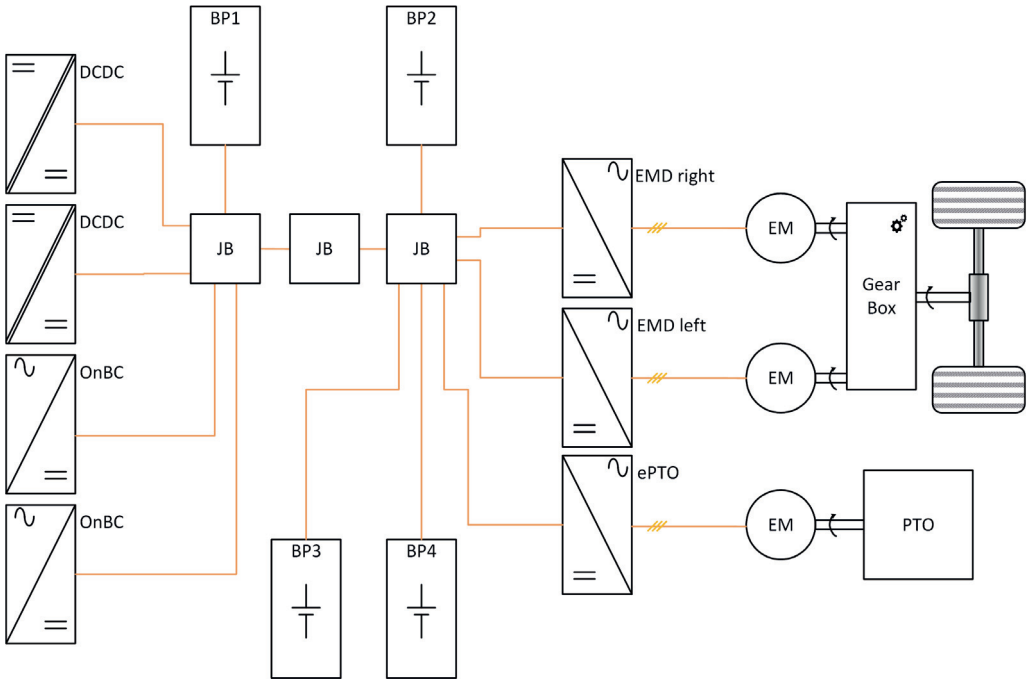

Figure 2.1: Volvo truck FE280 system layout

2.2 Other system

This thesis includes only a standalone vehicle in operation and the corresponding electrical dynamics on the TVS. The vehicle can be connected to the grid via the on- board or off-board chargers. The charger can, but must not, be galvanically isolated from the grid. Galvanic isolation is used to break the electrical potential between two systems, for example between the grid and the vehicle, to increase the electric safety level. With galvanic isolation in the On Board charger, the TVS system is electrically separate with respect to the ground of the grid supply.
Vehicles can also be used for power supply in an island operation, i.e. supplying electric energy where there is no connection to a electric grid. This can also be done with or without galvanic isolation between the vehicle TVS and the externally driven load that can be a DC-load or a 1- or 3-phase AC load.

Body builders (BB) have in the past on conventional vehicles connected loads mechanically to the combustion engine PTO or transmission PTO for supply of hydraulic pumps or air conditioning. In a BEV an alternative to providing a mechanical PTO is to supply the loads directly with electric energy. However, the vehicle manufacturer has no knowledge of the BB system and how the external load will interfere with TVS. This implies that an electric supply to a BB load needs a safety level, maybe galvanic isolation.
This thesis focuses entirely on the vehicle TVS without any connections to other vehicles, to the power grid or to BB loads.

2.3 Important sources and loads

The most relevant sources and loads are those directly connected to the TVS, i.e. 600 VDC loads and sources.

- The electric traction machine drive (EMD) converts DC to AC for the electric machine (EM) and vice versa.
- The 600V cables that connect all sub systems. There are both coaxial and twin axial cables.
- Battery chargers supplying the vehicle with power from the grid. These exist in several versions, isolated or non-isolated, separate or integrated and conductive or inductive etc. All need a unique model.
- The load from the 600 VDC/24 VDC converter. The loads on the 24 VDC side are not considered in this thesis more than the load from the 600 VDVC/24 VDC converter, called DCDC.
- The 600 VDC battery that supplies the vehicle with energy or receives energy at braking.

With the exception of the batteries and the cables that connect the sources and loads, all loads connected to the TVS are built with a Pulse Width Modulated (PWM) converter as an interface between the TVS and the load. These PWM modulated converters are sources of both DM and CM harmonics that spread throughout the TVS, the cables, the batteries and all other connected sources and loads. The choice of switching frequency of these converters is a balancing between, but not limited to, switching losses and size of the DC-link capacitor on the TVS side of every converter. The switching frequencies used by the different converters spread in a large wide between 1kHz to 100kHz.

2.3.1 Electric Machine Drive - EMD

The EMD is the most powerful converter in the vehicle and is in power range of 150kW and higher. The TVS contains at least one EMD that converts power between DC and

AC, the sign of which depends on the sign of the wheel torque. The EMD is a three phase converter with insulated-gate bipolar transistors (IGBT) but can be expected to use faster switches (SiC type) in the future making it a potentially bigger source of harmonic disturbances. The power of the EMD is above 200kW and has a switching frequency below 10kHz. Depending on size of the vehicle it can use one or more EMDs operating in parallel on the TVS but with one electrical traction machine per EMD. Other combinations can be conceived with multiple EMDs per EM, or more than one or two traction machines, but such are not considered in this particular case.

2.3.2 Electric traction Machine - EM

The electric traction machine (EM) is a permanent magnet synchronous machine (PMSM). However other types of EM as induction machines or reluctance machines can also be used but PMSM is the choice here due to the high torque to volume ratio. In this thesis the EM is referring to as the electric traction machine since the electric traction machine(s) have a special role in the harmonics analysis. There are of course EMs in the air compressor, the air condition unit and possibly also as a mechanical PTO interface for body builders (BB) to supply mechanical power to external loads not related to the propulsion of the vehicle.

2.3.3 Energy Storage - Batteries

The traction batteries are the main energy storages supplying or receiving electric energy. Batteries are available in many different chemistries and power types, as energy or power optimized batteries. For EVs the energy optimized batteries are the normal type of batteries as high energy content is vital and the large number of parallel batteries still can deliver the requested power. In a hybrid vehicle the installed energy is relatively low, but the instantaneous power requirement can be high and therefore power optimized batteries are preferred. In this thesis the battery itself will not be considered at all, only the electrical characteristics of the battery. It is a common concern if the batteries can withstand the current ripple in a vehicle and to what magnitude. It has been shown, [3], that Li-Ion batteries are generally not negatively impacted by the ripple current.

2.3.4 Charging systems

Chargers are available in many different types with very different properties. The most common are:

- Offboard DC chargers, supplies the traction battery directly with DC power that is galvanic isolated from the grid.
- Isolated OnBoard Chargers (OnBC), that are supplied with AC power from the external AC grid and transfers this power via a galvanically isolating interface and subsequently rectifies it to DC to supply it to the traction battery.

- Non-isolated OnBoard Chargers, that are supplied works like the Isolated version but does NOT provide galvanic isolation. Thus, there is a low impedance path between the grid and the TVS.

Charging and the connection to the grid is not included in this thesis but the DC side of the OnBC still connected to the TVS system while driving. Thus, the impedance of the DC side of the OnBC must be represented in a simulation model representing the electric dynamics of the TVS.

2.3.5 24 V DC/DC

The DC/DC refers to a converter that supplies the 24VDC system from the traction batteries. The power consumption varies a lot depending on the type of vehicle and the loads but is normally rated from 7kW and higher.

2.3.6 Air Condition (HVAC)

The HVAC refers to a converter that drives the air condition unit. The power in the HVAC is from 10kW and higher depending on size of vehicle and climate zone for operation.

2.3.7 Air compressor

The Air Compressor refers to a converter that drives air compressor that provides air to the brake system. In the Volvo vehicles some compressors are supplied from the 24V system and some from TVS.

2.3.8 ePTO

The ePTO is the abbreviation for electric Power Take Out and origin from conventional trucks PTO with a mechanical interface. ePTOs exists in a few variants:

- Mech. ePTO, a mechanical interface with a shaft that supplies mechanical power.
- DC ePTO, an electric DC interface that supplies electric power.
- AC ePTO, an electric AC interface that supplies electric power.

The mechanical ePTO is a solution where the BB can request speed of the shaft from a predefined control interface. The DC ePTO is more complicated, as the BB subsystem is unknown and thus it cannot be predicted how it will affect the TVS if connected directly. A way to take care of the uncertainty is to have a galvanic isolated 600VDC/600VDC converter as the interface. If the BB generates a fault or electric interference the TVS can stay operational and protected. For AC ePTO there is a need of a power electronic converter, but it can be either galvanic isolated or not but for the same reason as for the DC ePTO a galvanic isolated is recommended.

2.4 CM and DM

There are two different types of currents flowing in the TVS, Common Mode (CM) and Differential Mode (DM) currents. DM current is the desired current that supports the loads with energy. A DM current flows from the energy source, battery, to the converter and back, see figure 2.2. There is, usually, an un-wanted portion of the DM current that is a superimposed current ripple. This is caused by the switching in the converters. DM current causes losses in capacitors and inductors and if the current is higher than nominal the life length will be reduced or in worst case an immediate failure. The DM currents higher than nominal are most likely caused by current ripple between converters.

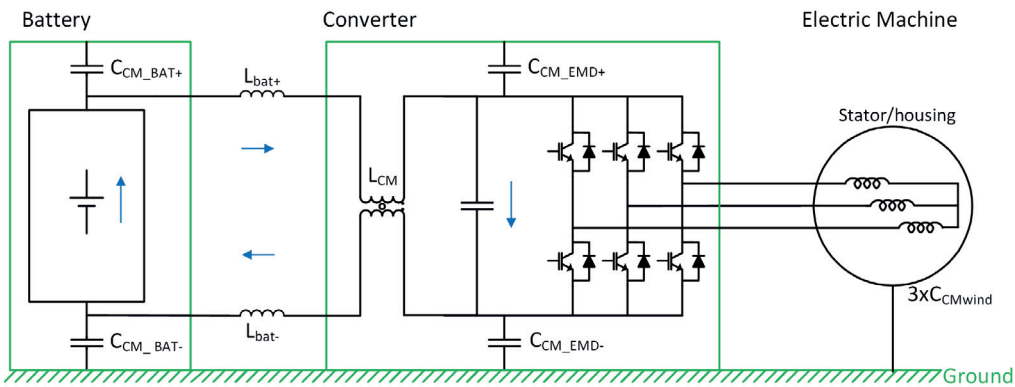

Figure 2.2: Differential Mode (DM) current

A CM current is an un-wanted current caused by switching of the converters and conducted by parasitic capacitances in the TVS. CM current leaks out via e.g. the parasitic capacitances between the EM windings and the EM core, represented in this case by the red capacitors in figure 2.3. The CM currents flows in the main conductors from the EMD to the EM and return both in the ground plane and in the cable shields, via intentional pole to chassis capacitors in the battery pack and in the EMD.

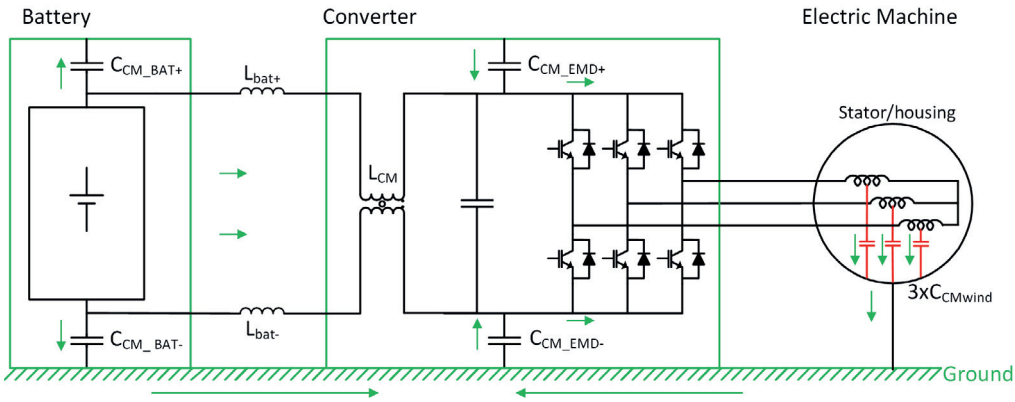

Figure 2.3: Common Mode (CM) current

It is found that the paths and distribution of the CM current and voltage is complicated. The CM currents can be divided in two different current paths, see figure 2.4.

1. A CM current path mainly involving the EMD, and EM driven by the charge/discharge of the parasitic capacitances in the EM, C_{CMwind}, that are reconnected in several different asymmetric states relative to the DC link depending on the switch state of the EMD, and

2. A CM current path involving the Battery and the EMD indirectly driven by the varying voltage drop across the CM capacitances of the EMD due to the currents of path 1

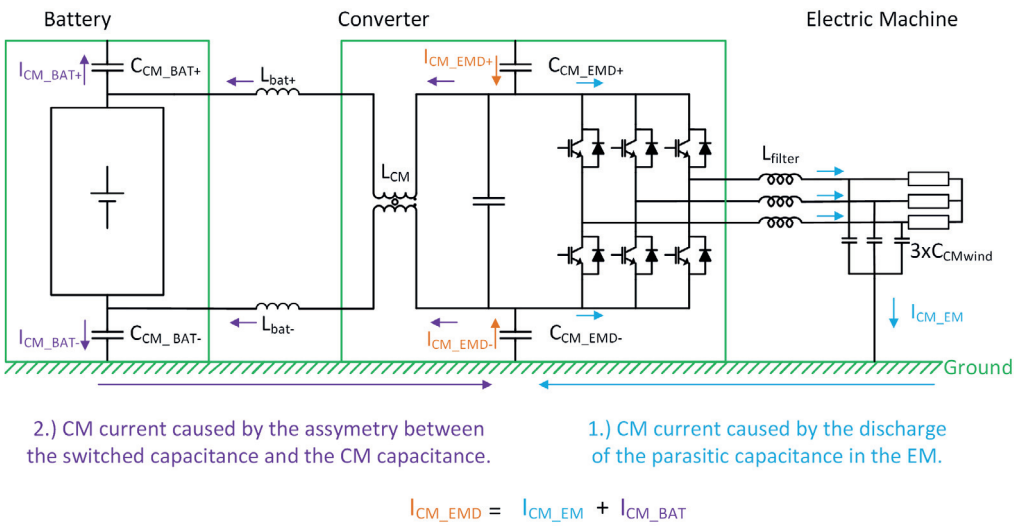

Figure 2.4: Two different CM currents and paths.

It shall be clear that none of the CM current caused by the asymmetry exist without the asymmetric parasitic capacitance C_{CMwind} in the EM, but with good system design the I_{CM_BAT} can be decreased or almost eliminated. It shall also be clear that there are other asymmetric capacitances in the system, but since the electric traction machines are the largest electric machines that thus also have the largest parasitic capacitances, the C_{CMwind} is used as example in the following explanations.

The supplier of a subsystem does not necessarily have knowledge of other subsystems. It is necessary that a vehicle manufacturer has the complete system knowledge to ensure that the system is designed with proper characteristics for DM and CM. To achieve proper characteristics means that requirements have to be set towards the suppliers.

2.4.1 CM capacitance unbalance

This subsection shows the unbalance of the asymmetric capacitances. The converter switches with the 8 combinations (0,0,0), (1,0,0), (1,1,0), (0,1,0), (0,1,1), (0,0,1), (1,0,1) and (1,1,1). Each switching combination will create an unbalance of the common mode capacitance as the parasitic capacitance in the EM will connect to the positive or negative side of the EMD DC terminals. This unbalance is shown in the following eight figures.

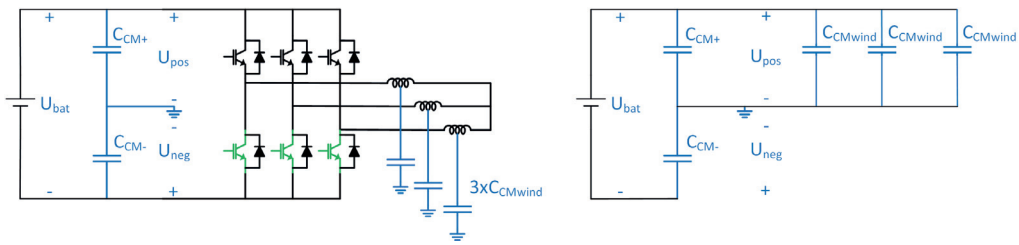

Figure 2.5: Unbalance when the converter is in the switching combination (0,0,0).

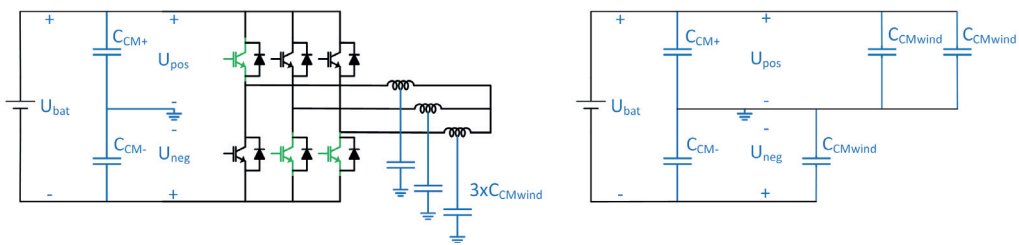

Figure 2.6: Unbalance when the converter is in the switching combination (1,0,0).

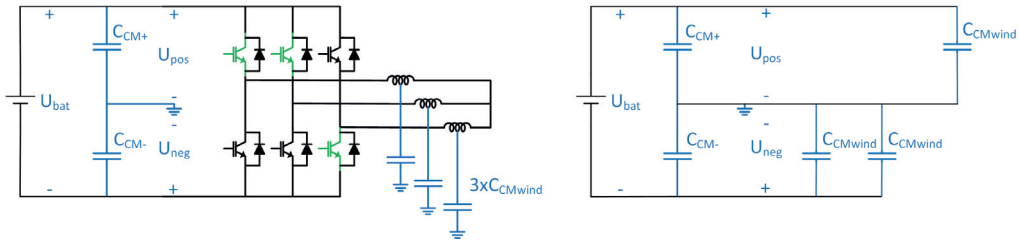

Figure 2.7: Unbalance when the converter is in the switching combination (1,1,0).

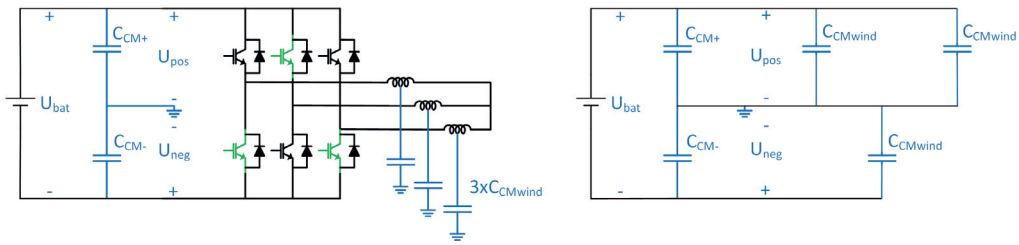

Figure 2.8: Unbalance when the converter is in the switching combination (0,1,0).

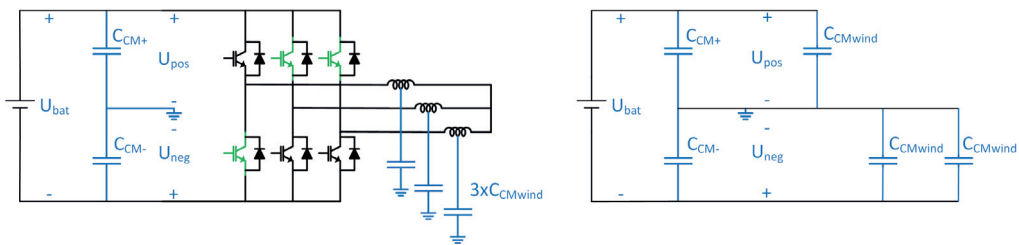

Figure 2.9: Unbalance when the converter is in the switching combination (0,1,1).

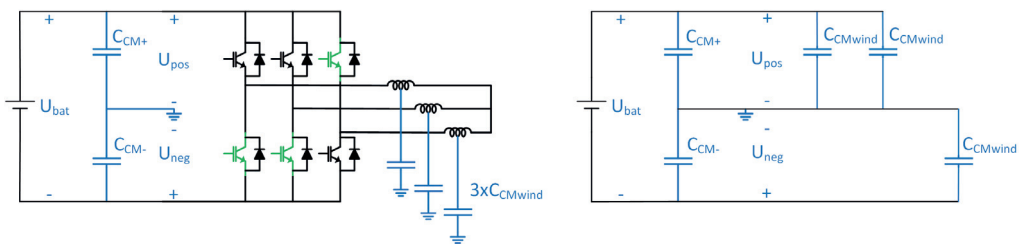

Figure 2.10: Unbalance when the converter is in the switching combination (0,0,1).

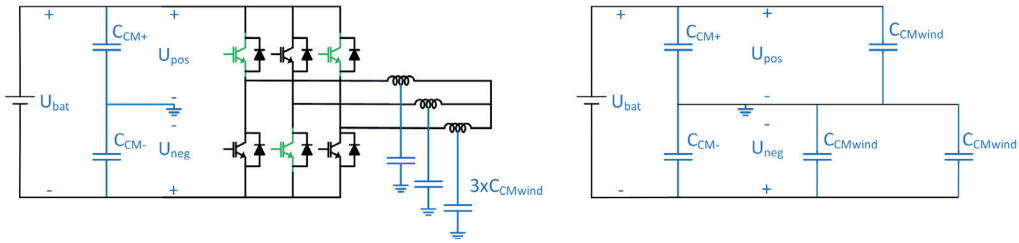

Figure 2.11: Unbalance when the converter is in the switching combination (1,0,1).

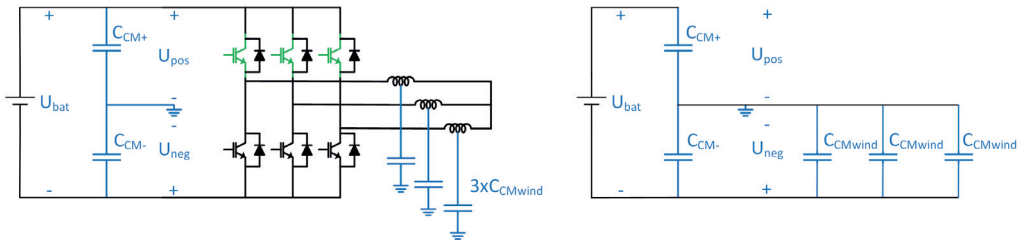

Figure 2.12: Unbalance when the converter is in the switching combination (1,1,1).

Note that with normal PWM the switching takes normally place between any consecutive state of the figures 2.5 to figure 2.12, and that in that case a switching always means that the asymmetry of the winding capacitors of the EM is changed at every switching of the EMD.

2.4.2 Asymmetric parasitic capacitances

In this thesis the EM parasitic capacitance C_{CMwind} is used in the study of the dynamic effects on the TVS of a asymmetric parasitic capacitance. Some more examples of asymmetric capacitances are shown below, but not limited to them.

- Between the winding and core in the transformer, which is used in a H-bridge in a DCDC converter.
- Between any semiconductor of a converter and the heat sink.
- Between the main conductors and the shield in three phase cable.
- Between the windings and the core of all other electrical machines connected to the TVS, like the machines driving the HVAC compressor, the Air compressor of a potential ePTO. These electric machines are generally smaller than the main electric traction machines and the corresponding parasitic capacitances of those can be expected to be smaller too. In this thesis, no effort is made to validate this statement

and the parasitic capacitances of these machines must be expected to be relevant. However, they are not modeled in this thesis.

The parasitic capacitance will create an unbalance of capacitance during switching and the parasitic capacitance will be charged/dis-charge during each switching, see 2.4.3.

2.4.3 Common Mode DC voltage (U_{CMDC})

When the EMD switches the EM winding-to-core capacitances are alternating between two asymmetric positions in the circuit diagram, that also means that the electric potentials of the battery terminals varies slightly depending on which asymmetric state the EMD+EM is in. This small variation is hereafter referred to as a CMDC voltage of the battery.

The CM voltage is defined as:

$$u_{cm} = \frac{u_{pos} + u_{neg}}{2} \tag{2.1}$$

Where u_{pos} is the positive potential of the battery and u_{neg} is the negative potential of the battery, both related to e.g., chassis. Generally, when the EMD switches one phase at a time, the U_{CM} becomes a quasi-square wave. The works case appears however when the EMD switches all phases simultaneously, which happens when the output voltage is zero. At standstill, with a zero output voltage to the EM, the CM voltage U_{CM} forms a square wave with the amplitude of U_{CMDC}, see figure 2.13, and becomes quasi square wave when the EM rotates or with a system with more than one EM with non-synchronized modulation of the EM drivers. The said CMDC square or quasi square voltage is referred to as the CMDC voltage in this thesis. The definition of the CMDC voltage and wave form is explained in this subsection.

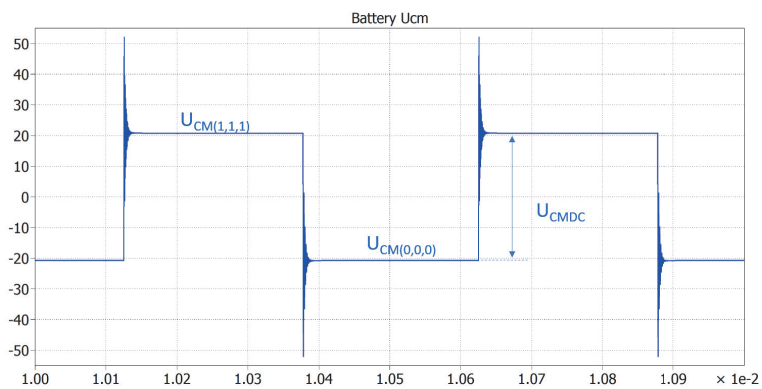

Figure 2.13: References for CM voltages and CMDC voltage.

The cause for the CMDC voltage is the switching between asymmetric states of the parasitic winding-to-core capacitance of the EM, denoted as C_{CMwind}.

The common mode capacitances that are symmetrical, C_{CM_BAT+}, C_{CM_BAT-}, C_{CM_EMD+} and C_{CM_EMD-} are denoted as C_{CM+} and C_{CM-}, according to equation 2.2 and 2.3 shown in figure 2.14.

$$C_{CM+} = C_{CM\_BAT+} + C_{CM\_EMD+} \tag{2.2}$$

$$C_{CM-} = C_{CM\_BAT-} + C_{CM\_EMD-} \tag{2.3}$$

At standstill, with a zero output voltage, the three C_{CMwind} are asymmetric to either the positive or the negative pole of the TVS. The sum of C_{CM+} and C_{CMwind} is asymmetric relative to C_{CM-} with references to (A) in figure 2.14.

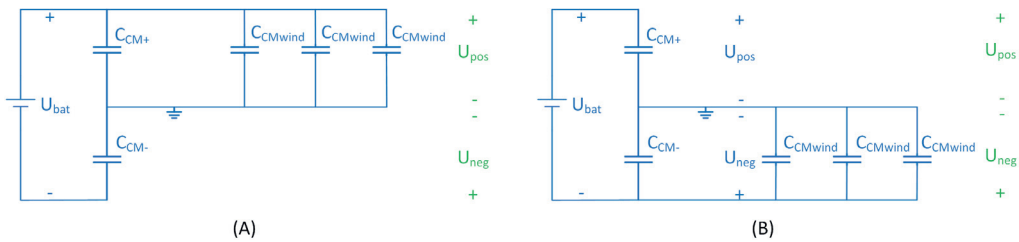

Figure 2.14: Equivalent circuit for the parameters included in the U_{CMDC} definition. In (A) the switch state is (0,0,0) and in (B) (1,1,1).

C_{CM+} and C_{CM-} are assumed to be symmetrical in this thesis and denoted C_{CM} according to equation 2.4. However, the shown cause and effect will be the same if it was asymmetrical.

According to equation 2.4 and 2.5, figure 2.14 is re-drawn to figure 2.15.

$$C_{CM} = C_{CM+} = C_{CM-} \tag{2.4}$$

$$C_{CMasym} = 3 * C_{CMwind} \tag{2.5}$$

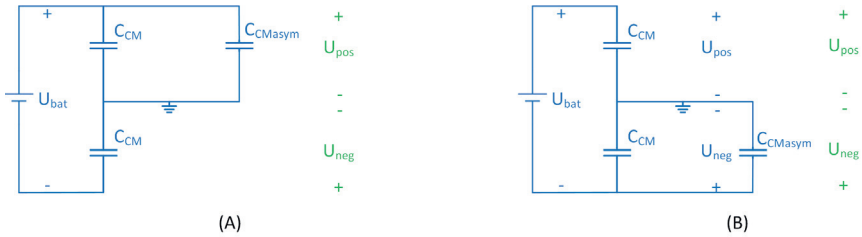

Figure 2.15: Equivalent circuit for the parameters included in the U_{CMDC} definition. In (A) the switch state is (0,0,0) and in (B) (1,1,1). The three C_{CMwind} is replaced with C_{CMasym}

The ratio between the asymmetrical capacitance C_{CMasym} and the C_{CM} is defined as:

$$X = \frac{C_{CM}}{C_{CMasym}} \tag{2.6}$$

From figure 2.15 following equation is obvious:

$$U_{bat} = U_{pos} - U_{neg} \tag{2.7}$$

The charge of a capacitor is:

$$Q = C * U \tag{2.8}$$

The charge is equal between serial connected capacitors.

$$Q = C_1 * U_1 = C_2 * U_2 \tag{2.9}$$

When the switches are in the state (0,0,0), according to (A) in figure 2.15, the total capacitance towards positive pole is C_{CM} + C_{CMasym} and towards negative pole C_{CM}. From figure 2.15 and equation 2.9 it is found that:

$$U_{pos} * (C_{CMasym} + C_{CM}) = -U_{neg} * C_{CM} \tag{2.10}$$

Combine equation 2.6, 2.7 and 2.10 and the following equation is derived:

$$U_{pos(0,0,0)} = \frac{U_{bat}}{2 + \frac{1}{X}} \tag{2.11}$$

The same equations apply for U_{neg}

$$U_{neg(0,0,0)} = -U_{bat}\frac{1 + \frac{1}{X}}{2 + \frac{1}{X}} \tag{2.12}$$

In the opposite state, when the switches are in the state (1,1,1) the total capacitance towards positive pole is C_{CM} and towards negative pole C_{CM} + C_{CMasym}. The voltages U_{pos} and U_{neg} will now change due to the asymmetry:

$$U_{pos(1,1,1)} = U_{bat}\frac{1+\frac{1}{X}}{2+\frac{1}{X}} \tag{2.13}$$

$$U_{neg(1,1,1)} = -\frac{U_{bat}}{2+\frac{1}{X}} \tag{2.14}$$

The Common Mode voltage at the switch state (0,0,0) is calculated from equation 2.1, 2.11 and 2.12.

$$U_{cm(0,0,0)} = -\frac{U_{bat}}{2(2X+1)} \tag{2.15}$$

The Common Mode voltage at the switch state (1,1,1) is calculated from equation 2.1, 2.13 and 2.14.

$$U_{cm(1,1,1)} = \frac{U_{bat}}{2(2X+1)} \tag{2.16}$$

The Common Mode DC voltage is defined as the difference in voltage when the switches changes, in this case from $U_{pos(0,0,0)}$ to $U_{pos(1,1,1)}$, see figure 2.13. From equation 2.15 and 2.16

$$U_{CMDC} = U_{cm(1,1,1)} - U_{cm(0,0,0)} = \frac{U_{bat}}{2X+1} \tag{2.17}$$

It is obvious from equation 2.17 that the U_{CMDC} will decrease with increasing X. Increasing X means that C_{CM} is made bigger in relation to C_{CMasym}. An example of this is shown in figure 2.16 with three different X values, 6.67, 20 and 50.

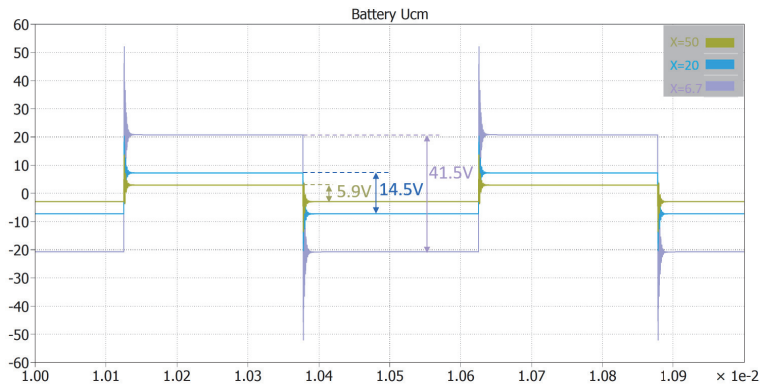

Figure 2.16: Increasing X decreases the U_{CMDC}. The X values in the graph are 6.67, 20 and 50

Using the equation 2.17 will give the same values for U_{CMDC} as in figure 2.16.

2.4.4 CM currents cause and effect

The CM current can be divided in two different current paths, as mentioned in 2.4 and shown in figure 2.4. For convenience the same figure is repeated below in figure 2.17.

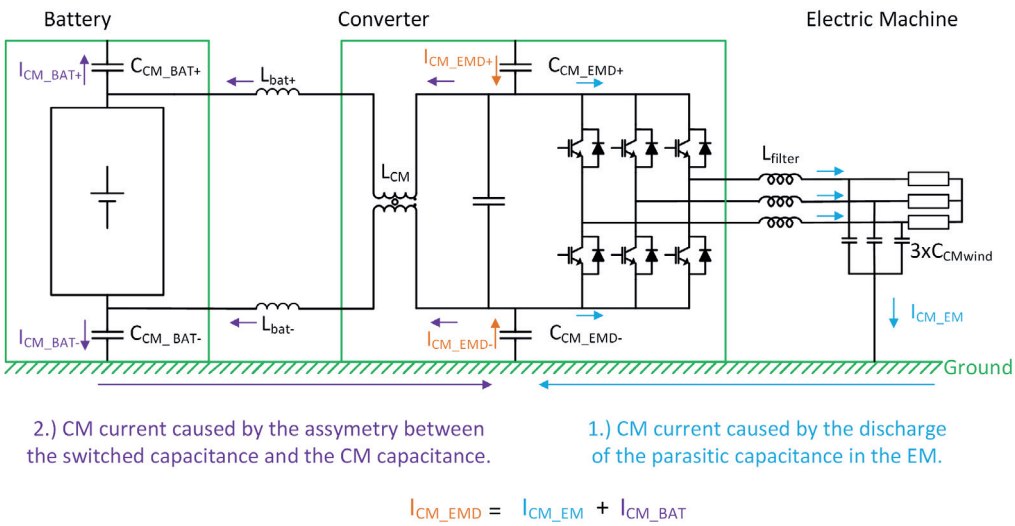

Figure 2.17: Two different CM currents and paths.

Cause and effects of I_{CM_EM}

Starting with the I_{CM_EM} this current will always flow and cannot be avoided as the C_{CMwind} will alternate between positive and negative pole. The only ways to reduce this current is:

- the size of C_{CMwind}
- the voltage derivative of the phase output voltage, limited by the semiconductor's loss dissipation
- the voltage derivative at the phase winding due to the impedance in the circuit
- to some extent by modulation, by avoiding switching between (0,0,0) and (1,1,1) directly.

The size of the parasitic capacitance in the EM is caused by laws of physics. It shall be requested by the suppliers to keep C_{CMwind} as low as possible. However, to reduce this capacitance the winding insulation has to be made thicker, which contributes to lower cooling capability of the phase winding losses. The C_{CMwind} can also vary by time due to wear of the insulation material but will not be discussed in this thesis.

The current is determined by equation 2.18 where the voltage derivative over the C_{CMwind} is.

$$i_{CM\_EM} = C\frac{du}{dt} \tag{2.18}$$

The voltage derivative, at the EM, is normally limited by an inductive CM filter after the EMD, represented by L_{filter} in figure 2.17. It shall also be noted that there are parasitic capacitances within the semiconductors that will only be limited by the dv/dt in the semiconductor.
Finally, the modulation does not really limit the current but at zero output voltage when the switch state is (0,0,0) or (1,1,1) all three C_{CMwind} will change polarity in the same direction and increase the total I_{CM_EM} resulting in the highest CM current. When the output voltage to the EM is greater than zero the switches can be connected according to subsection 2.4.1. This has the effect that when switching between active states (all states but (0,0,0) and (1,1,1)) one of the C_{CMwind} can recharge another C_{CMwind} and the result is a lower total I_{CM_EM}.

In figure 2.18 it is shown how the I_{CM_EM} is changed by lowering du/dt which is done by decreasing the inductance L_{filter} to a third.

The ratio of the frequencies, $f(L_{filter})$ and $f(0.33xL_{filter})$ shown in the lower graph in figure 2.18, of the two currents is 3.1.
In figure 2.17 it is shown that there is a LC circuit formed by C_{CMwind}, C_{CM_EMD} and L_{filter}.

The resonance frequency of a LC circuit is:

$$f_{res} = \frac{1}{2\pi\sqrt{LC}} \tag{2.19}$$

When the ratio of L is changed 1/3 the ratio of f is change with $\sqrt{1/3}$=0.58, the same factor that is measured in figure 2.18.

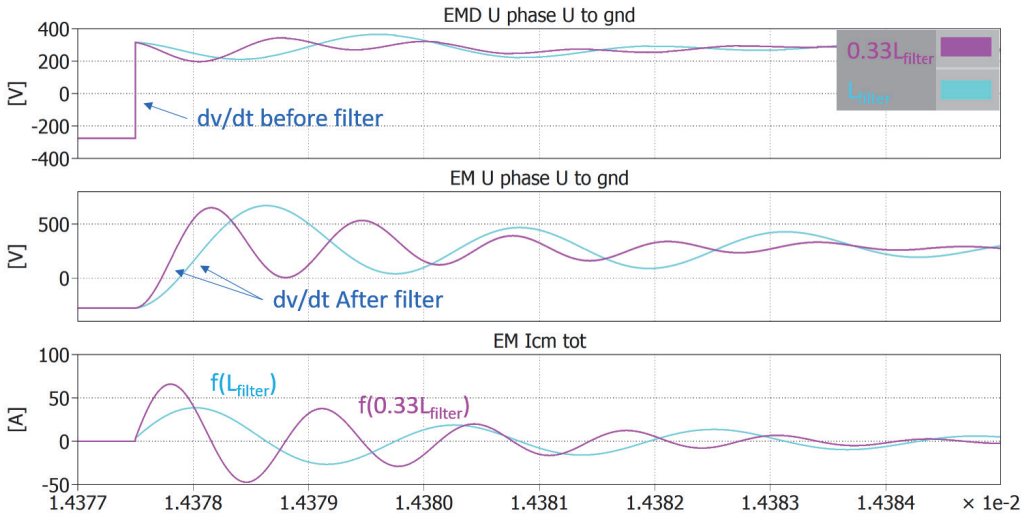

Figure 2.18: CM current from the EM when the inductance is decreased to 1/3.

The rise- and fall time of the IGBT, t_r and t_f, can also be changed to lower the current derivative but in this example, it has to be changed to at least 50 times longer to give an effect in this example. That long t_r and t_f is unrealistic, due to high switching losses that causes high temperature in the IGBT, but also shows the importance of a CM filter after the 3-phase bridge in the EMD.
The conclusion is that the CM filter is important to keep the peak current low as well as lowering the frequency. The frequency of I_{CM_EM} is formed by the circuit, in figure 2.17, C_{CM_EMD}, L_{filter} and C_{CMwind}.

Cause and effects of I_{CM_BAT}

The only change of potential in the system occurs when the EMD switches. Looking at the same occasion as in figure 2.18 with the graph for the battery CM voltage and current included, see figure 2.19, it is shown that the frequency f_{bat} for the battery CM current I_{CM_BAT} does not change in frequency or amplitude due to the change of current derivative in the CM current in the EM. The frequencies are also completely different. It is found that the frequency of I_{CM_BAT} is formed by the circuit, in figure 2.17, C_{CM_BAT}, L_{BAT}, L_{CM} and C_{CM_EMD}.

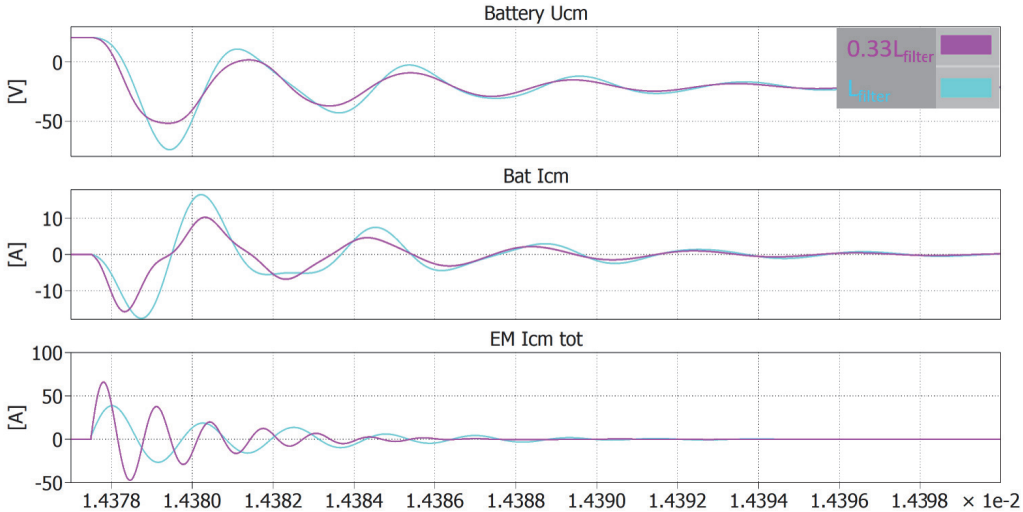

Figure 2.19: CM current from the the battery when the dv/dt is changed to the EM by changing the inductance.

The CMDC voltage can be changed according to equation 2.17. The CMDC voltage is changed by changing the X factor, see equation 2.6. X can be changed by C_{CM_EMD}, C_{CM_BAT} or a combination of both. In figure 2.20 there are three combinations of capacitances, C_{CM_EMD} is increased 5 times, C_{CM_BAT} is increased 5 times and finally unchanged values as reference. Once again it is clear that the I_{CM_EM} is unchanged, middle graph, when C_{CM_EMD} and C_{CM_BAT} is changed. In the top graph it is shown that U_{CMDC} decreases when X is increased. In the lowest graph it is shown that I_{CM_BAT} is increased when C_{CM_BAT} is increased and contrarily decreases when C_{CM_EMD} is increased.

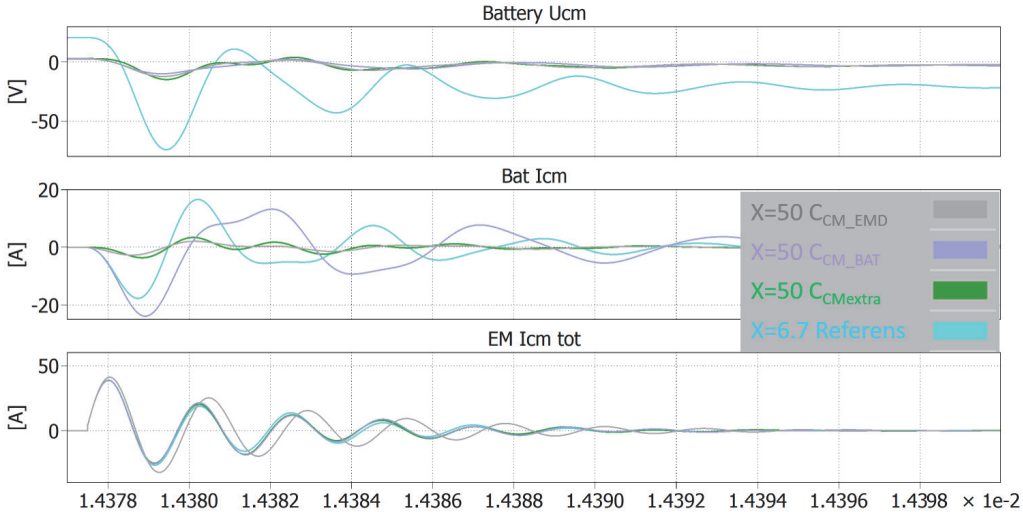

Figure 2.20: CM current from the the battery when the CM capacitances are varied to achieve X=50.

The obvious conclusion is that X shall be as high as possible to reduce U_{CMDC} and that the capacitance shall be increased in the EMD to avoid CM currents in the system. Unfortunately, there are constrains in the standards. The total capacitance from the poles to ground/chassis is limited during charging by the standard [12]. An alternative solution is to add the capacitance outside the EMD and connect the capacitance after the charger is connected. That is done by $C_{CMextra}$ in figure 2.20. The same solution can be achieved if a controlled CM capacitor can be place within the EMD after the CM filter. This will give a good system if the CM capacitances in the system, for example in the batteries, cannot be kept low and the ratio of X=50 cannot be achieved without the mentioned solution.
This can be solved by a CM capacitance that is connected when the EMD is activated and in operation, the EMD is not in operation during charging. There are three possible ways to mount the extra CM capacitances, see figure 2.21

1. Inside the EMD.
2. Outside the EMD but with connection to the poles after the inductive CM filter.
3. Outside the EMD with connection to the poles before the inductive CM filter.

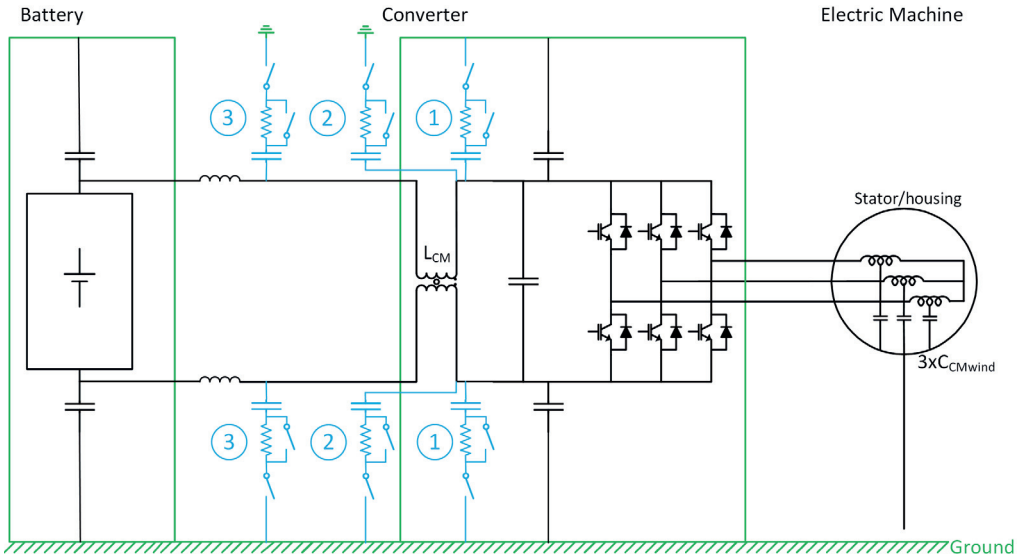

Figure 2.21: Possible solutions to mount the extra CM capacitance.

The advantage of having the filter inside is to minimize the risk of oscillations due to an extra LC circuit that is formed. The extra CM capacitance is connected via a pre-charge circuit and a switch that disconnects the circuit when the EMDs not are in operation.

2.4.5 DM current

All subsystems in TVS are switching apart from the battery. The switching causes voltage ripple at the DC link of the converter. Depending on filters and TVS impedance, a current ripple will flow between the subsystems in the TVS. It is impossible to tell what can happen if current ripple flows between the converters but following can be stated:

- Current ripple in the DC link capacitor causes heat and decreased lifetime. Suppliers dimension the capacitor for the load current and not for extra ripple from the system.
- current ripple in the inductive filters causes heat and can change the inductance as well as decrease the lifetime.
- current ripple is worst at duty cycle 0.5, see [1]

The DM behavior is a part of future work

2.4.6 DM filter

It is normal that the subsystems are sourced from different suppliers and there is no clear requirement on the TVS voltage quality. One way to protect the subsystem itself and ensure low disturbance to the other subsystems is to have a DM filter at each converter. Filter

always have a resonance point. As the frequencies in TVS not always are known by the suppliers, the filter is recommended to be damped.
In the following to figures, figure 2.22 and figure 2.23 a series damped filter and an undamped filter is shown.

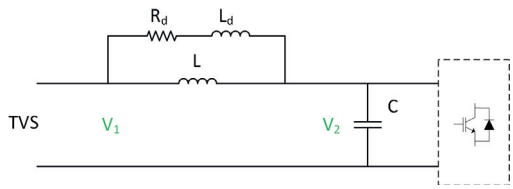

Figure 2.22: Series damped filter.

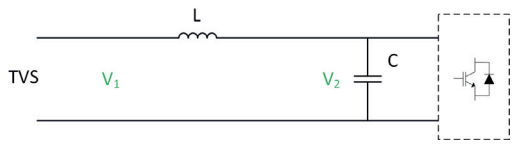

Figure 2.23: Undamped filter.

The resonance point for the filter is:

$$f_0 = \frac{1}{2\pi\sqrt{LC}} \tag{2.20}$$

In [23] optimal damping parameters are described. The transfer function for the series damped and undamped circuit is shown in figure 2.24.

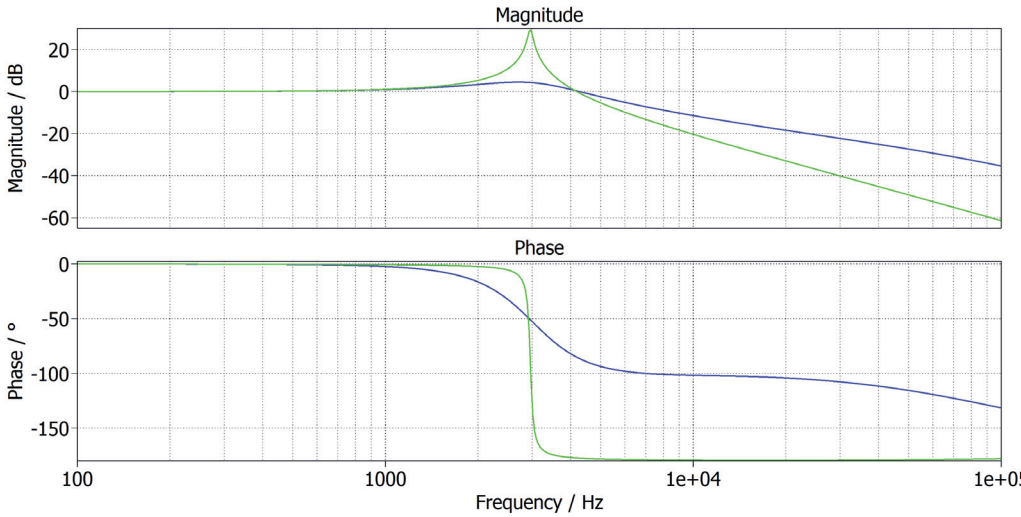

Figure 2.24: Transfer function for a series damped and undamped filter is shown.

If a converter has the switching frequency f_s, TVS experiences the frequency $2xf_s$. In the transfer function in figure 2.24 the resonance frequency is 3 kHz. Imaging that a neighboring converter is switching at 1.5 kHz and the filter is undamped, the DC-link capacitor C in figure 2.23 will be exposed for a high ripple current that potentially can destroy it. If the filter was damped according figure 2.22 the series damped filter will make sure to attenuate the resonance.

If there is no filter at all, the resonance can be almost anything depending on the inductance TVS, mainly in the cable between the source and victim.

Even though damped filters are recommended precautions has to be taken for the contactor or fuse in the system in case of a short circuit. It must be able to break the inductive current.

Chapter 3

Sub system simulation model and calibration

The purpose of the concept modeling is to produce a vehicle simulation model in order to be able to predict the EMC characteristics of the system. In order to accomplish this each subsystem is measured, equivalent circuits are derived from the measurement, including 600V battery packs, and finally implemented in a proper simulation tool. The intention is that the models shall be appendix A.

The aim with the complete model is to replace the number of vehicle measurements with simulation. This will save cost and lead time.

In laboratory setup frequencies for the common mode current has been seen up to 7MHz and with this in mind the target frequency range of the CM models is set DC-30MHz. However practical measurements on the components shows that reliable results are hard to get above 10MHz.

The frequency, of the differential mode current is multiples of the switching frequency and the target frequency range of the DM models is set DC-100kHz. The difference between the CM and DM models is that the complexity of the DM model can be reduced compared to the CM models.

The models presented in this chapter are shown as generic schematics of the converters as the detailed schematics of the models is an IP of the supplier.

In this chapter different measurement methods are described. Followed by measurements on subsystems that are compared with the graph obtained from the simulation model that is derived from measurements and circuit diagrams.

3.1 Measurement methods required

To obtain measurements of the impedances that make up a simulation model of a subsystem it is convenient to use an LCR-meter. It is an instrument made to analyze frequency characteristics of various types of sub systems. Given the intended validity of the frequency range of the sub system models (CM: 0Hz – 10MHz, DM: 0Hz-100kHz), the chosen LCR meter is a PSM3750 Frequency Response Analyzer [16] with an IAI2 Impedance Analyzer [15], see figure 3.1. The involved instruments are calibrated within the Volvo "calibration program", e.g. the instruments are sent to an approved calibration center regularly. But even more important is that the measurement setup is calibrated before each measurement setup. The important values are at low impedance and therefore the setup is calibrated towards a short circuit. This will remove the impact of the cables in the measurement setup. But still a small change in the "loop" of the measurement cables will impact the result. The result in the frequency above 5 MHz can always be questioned. Is the resonance caused by the measurement setup or is it from the Device Under Test (DUT)?
The section describes how the LCR measurements are performed and the results from the measurements is an impedance and phase graph vs. frequency graph. This graph can be analyzed to form an equivalent circuit, see subsection A.1. A tool to build this equivalent circuit is Zview [27].

Figure 3.1: PSM3750+IAI Impedance Analysis Package is able to perform impedance measurement up to 35MHz. Picture from https://www.newtons4th.com/.

3.1.1 Kelvin Fixture

Accurate and consistent impedance-based measurements of not least very low or very high impedance situations require that the impedance introduced by the connectors are properly

accounted for. The connections would be optimized in a manner that consistently minimizes the introduced impedance as well as contact resistance without damaging the terminals of the DUT. Measurement solutions made for this are called 4-wire measurements, meaning that two probes provide the excitation signal, and another two probes measure the voltage of the DUT. The exact arrangement of the probe connection to the DUT affects to some degree the accuracy.The most accurate method is when using the the Kelvin Fixture, see figure 3.2, attached to the IAI2 Impedance Analyzer, see figure 3.3. The advantage with the Kelvin fixture is that the DUT is mounted between the "circuit boards" which implies that the stray inductance and parasitic capacitance induced together with the DUT is minimized. In the figure a cylinder shaped capacitor is attached in the Kelvin fixture. The Kelvin fixture is unfortunately too small to be used for 600 V cables or converters.

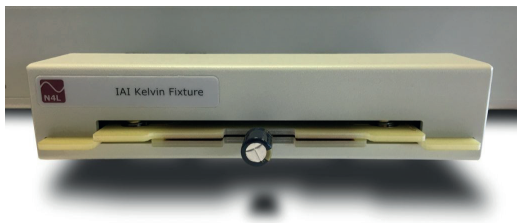

Figure 3.2: This fixture features four contact plates providing true four wire impedance measurement. A cylindrical capacitor is the DUT in this example. Valid frequency range for this this method is DC-35MHz. NB! A frequency is always needed for the LCR measurements and DC shall here be interpreted as 10µHz.

Figure 3.3: IAI Kelvin Fixture. DC-35MHz

3.1.2 Kelvin leads

Cables are needed and for some measurements long cables. One common method is the 4-wire Kelvin method with Kelvin leads, see figure 3.5 and 3.4. It is, during test, found

that the method is not accurate above 4-5MHz as the wires introduces capacitance and inductance in the circuit. This method is not used in this thesis for HF measurements.

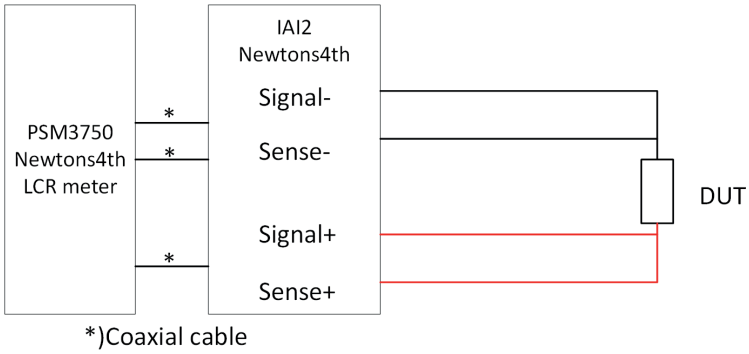

Figure 3.4: 4-wire Kelvin method is a straightforward method valid up to 5MHz

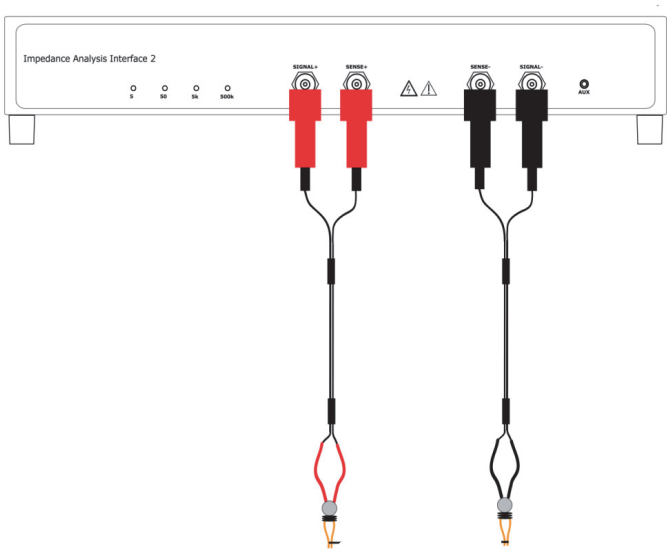

Figure 3.5: 4-wire Kelvin leads

3.1.3 4-wire method with separate current probe.

A new test method was developed for the measurements reported in this thesis. The test method is a 4-wire method with a high bandwidth current probe, see figure 3.6. The voltage of the DUT is measured directly on the DUT but the current is measured via a Pearson current monitor model 2877 [6] with a BW of 300Hz-200MHz is used. The method gives good accuracy up to 10-20 MHz in the impedance measurements. Good accuracy is not a

precise value. However, it can be seen that depending on test object, no unexpected resonance point is obtained up to 10-20MHz. The drawback is the lack of functionality in the lower frequency band and at "DC". Kelvin leads introduces impedance in the measurement leads and an alternative 2-wire method (not described) is also affected by the impedance in the measurement leads. The 4-wire method with separate current probe has been tested towards a known test DUT and compared with the other methods and found to be the best alternative. The DC properties are of most interest for the 600V cables which will be measured with a high current supply instead, see subsection 3.1.5.
This method with the Pearson probe will be referred to as the "4-wire method with separate current probe".

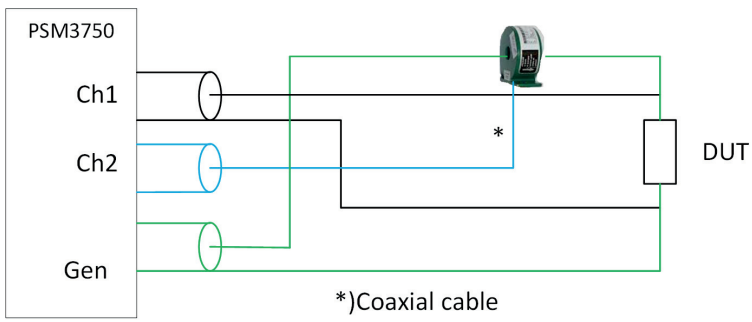

Figure 3.6: 4-wire method with separate current probe is a straight forward method valid up to 10-20MHz

3.1.4 Measuring on high voltage batteries with a HV interface.

Measurements on a battery or DC source is not possible with the LCR instrument since the DUT in that case has a (way to high) internal DC voltage source. It is not possible at AC sources either. The normal procedure is to measure on passive circuits as resistors, capacitors, inductors or a mix of them. If measurements shall be made on devices with an internal DC voltage, the DC voltage needs to be blocked. There are no HV LCR interfaces for voltages around 750VDC available on the market, or at least not found by the author of this thesis. A development has been performed of a HV LCR interface, a principal schematic is shown in figure 3.7.
The BW of the interface is estimated to 100Hz to 1MHz.
A measurement current is supplied from the PSM3750 Gen output and runs through a measurement resistor, 49.9Ω, to the DUT. 49.9Ωis an important value to set in the scale factor in the LCR measurement. The voltage is measured over the measurement resistor at Ch2 and is calculated as the current. The AC voltage is measured to Ch1 after the DC voltage is blocked at the capacitors.

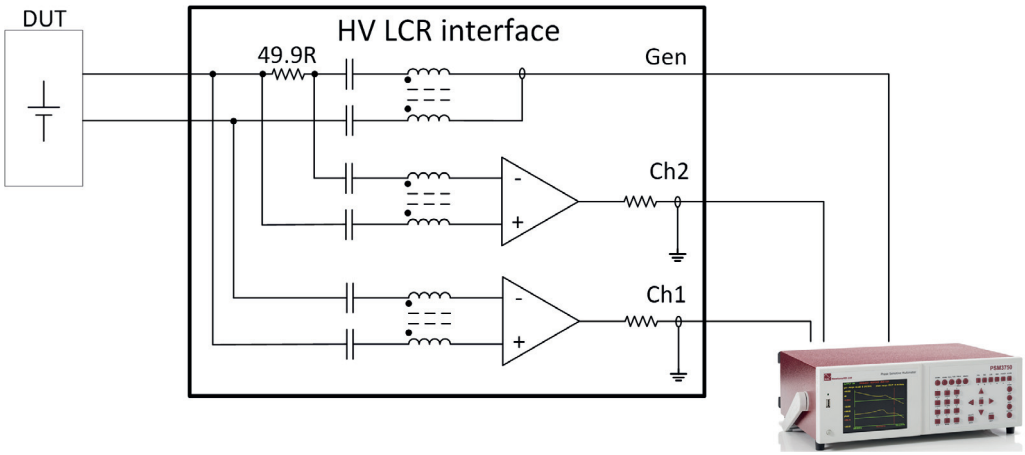

Figure 3.7: HV LCR interface with a BW of approximately 600Hz-1MHz

A battery has a short circuit current that shall be treated with respect and the principal setup in figure 3.7 is not possible in a real measurement. A fuse between the DUT and the HV LCR interface shall be used to protect the wires into the HV LCR interface.

3.1.5 Measuring with a high current supply for DC resistance.

To obtain the DC resistance of the cables a current source is used to deliver a high current. As mentioned earlier in this chapter the LCR method is not accurate at low impedances and the cable resistance is low. The measurement circuit is shown in figure 3.8.

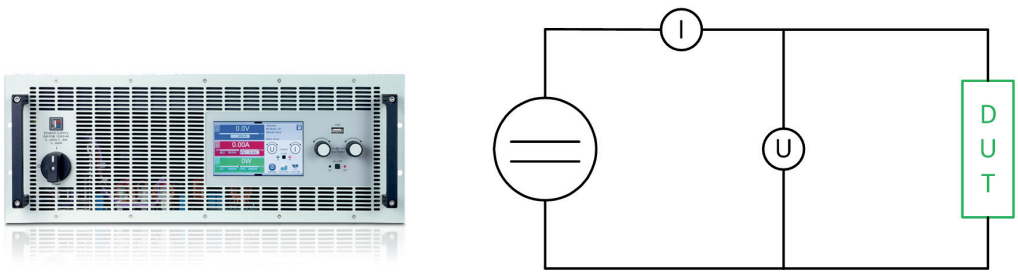

Figure 3.8: Measurement of the DC resistance

The current used for measurement has been varied between 0.5-2A/mm² in order to get a reasonable value of the voltage but still not heat the cable. the variation of resistance is negligible when varying the current. The resistance is obtained by:

$$R_{DUT} = \frac{U}{I} \tag{3.1}$$

3.2 Measurement and modeling of subsystems

The subsystems included in the Volvo vehicles are developed by external companies and the design is protected IP. The circuit diagrams presented here are therefore in an generic format and will not disclose, contain or reveal any IP. Graphs from measurements are shown in its full extent since anyone with access to a vehicle could do the same measurements. All models are developed from suitable LCR measurements as described in section 3.1, which means that the current during measurement is a small signal current and far from nominal current and even further from an overload situation. Since the measurement method is unable to make measurements at operating points corresponding to a high current level, it is almost impossible to create models that cope with a current dependency. Thus, this dependency is left out in this thesis. Inductors and capacitors shall not be overloaded as the life length as well as the electrical characteristics changes at overload. It is also common that the values found in data sheets are from LCR measurements at signal current.

When performing DM simulations, the upper frequency range is around 100kHz. In the experience of the author, it is not possible to represent the complete TVS of a full vehicle in the selected system simulation program. It just does not work for reasons of complexity. This is handled in either of two ways here:

1. For CM, only a reduced part of the vehicle is simulated, in this case the Battery, the DC cables, the EMD and the EM.
2. For DM the full vehicle is simulated, but with sub system models reduced to represent the measurements well up to 100 kHz, by removing parasitic capacitances, small capacitances and stray inductances.

3.2.1 Measurements and modeling of the EMD

The EMD is a four quadrant three phase converter that supplies and brakes the traction electric machines in the vehicle. It is the converter in the vehicle with the highest power rating up to 50 times the rated power of the auxiliary converters. A simplified scheme of the EMD is shown in figure 3.9.

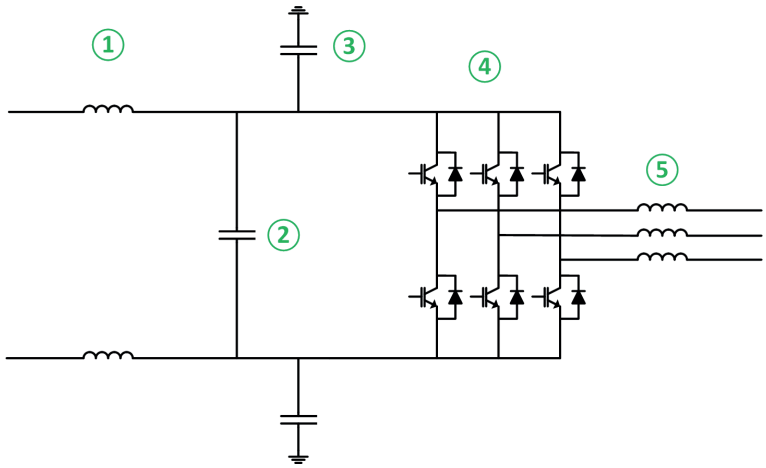

Figure 3.9: EMD main circuit

The included parts in the EMD is:

1. Input CM filter. Reduces the CM currents.
2. DC link capacitor. Supplies and stores the switching power.
3. CM capacitor. Return path for CM currents.
4. Three phase converter bridge. 3 phase legs.
5. Output CM filter. Reduces the CM current to the EM.

The complete model over the EMD is very complex and is not shown here. However, the simulations presented in this thesis are performed with the full model. The complete simulation model in the simulation program PLECS contains over 50 discrete components. A physical capacitor is represented by 5 discrete components. The IGBT model, used in the simulations, is developed in co-operation with the supplier. The IGBT model contains among other properties the rise and fall time, stray inductance and forward voltage drop. PLECS as a system simulation tool prefers to represent the semiconductors as ideal switches, but when simulating the CM currents, a model that corresponds to reality is necessary. Changes in the fall and rise time is directly coupled to the CM currents. There are 3 important measurements, according to figure 3.10,3.12 and 3.14, that shall correspond between the model and the measured values which are:

- The impedance from positive to negative pole, for the DM properties.
- The impedance from positive pole to vehicle chassis, for the CM properties.
- The impedance from negative pole to vehicle chassis, for the CM properties.

It is shown in figure 3.11, figure 3.13 and figure 3.15 that the measured impedance correlates with the model up to 10MHz for both DM and CM. There is a small resonance in the DM graph at 2-3MHz. This resonance comes from capacitive circuit from positive and negative pole to ground, see figure 3.9. The DM impedance is only relevant for the switching frequencies, e.g. up to 100kHZ.

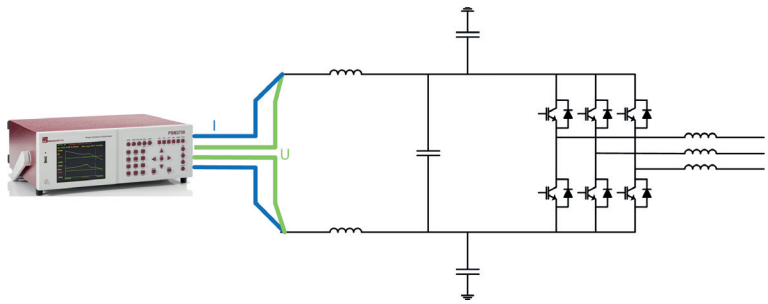

Figure 3.10: LCR measurement for the impedance and phase measured from positive to negative pole.

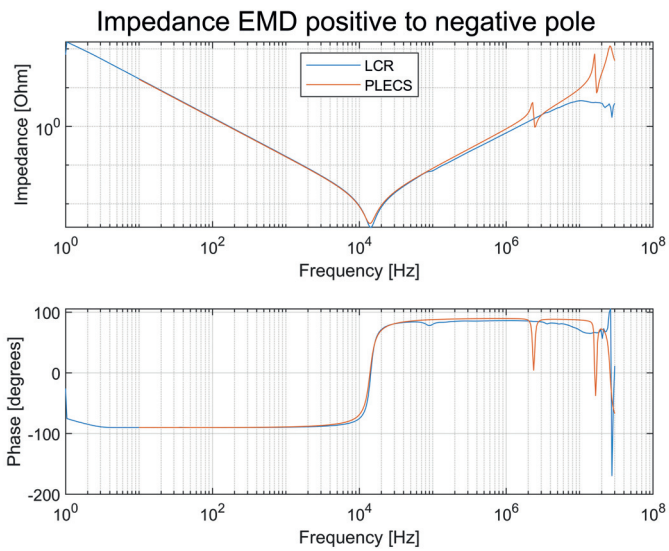

Figure 3.11: Impedance and phase as function of the frequency for the EMD measured from positive to negative pole.

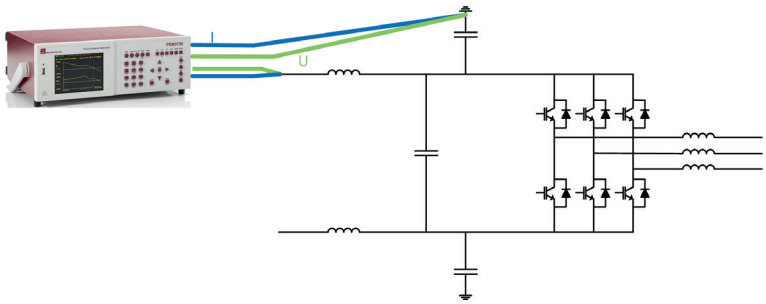

Figure 3.12: LCR measurement for the impedance and phase measured from positive pole to vehicle chassis.

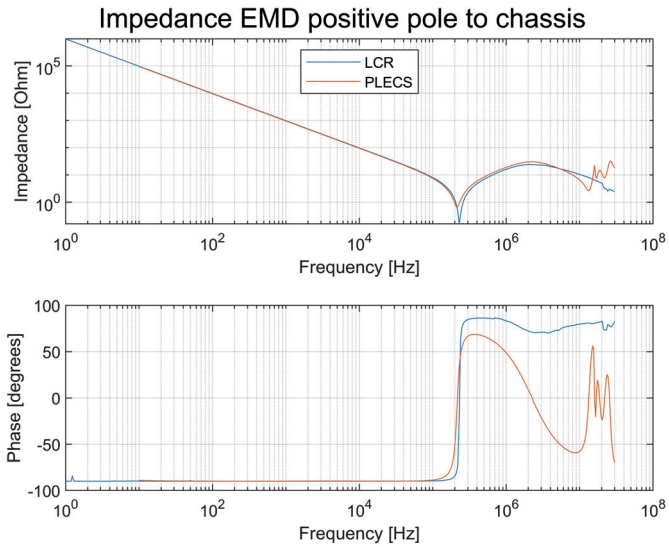

Figure 3.13: Impedance and phase as function of the frequency for the EMD measured from positive pole to vehicle chassis.

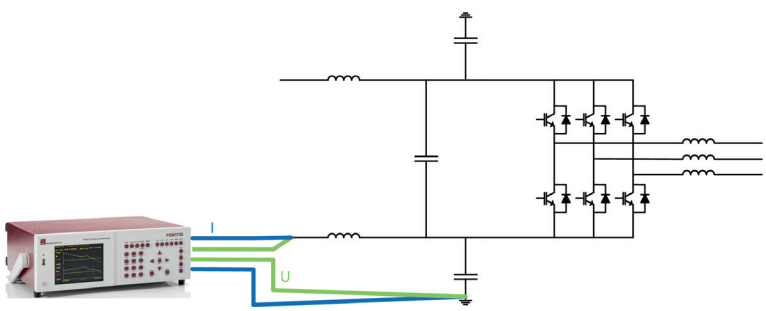

Figure 3.14: LCR measurement for the impedance and phase measured from negative pole to vehicle chassis.

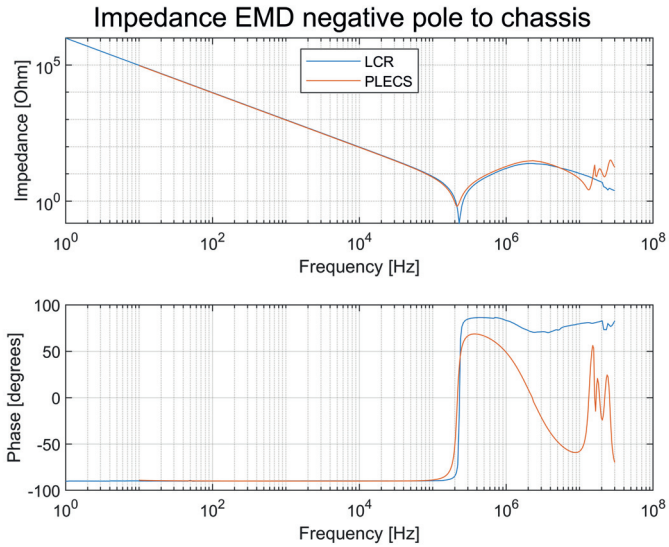

Figure 3.15: Impedance and phase as function of the frequency for the EMD measured from negative pole to vehicle chassis.

3.2.2 Measurements and modeling of the EM

The model for the EM in this section is developed from a CM perspective only. The CM currents leaks out to the chassis via the parasitic winding to core capacitances. Therefore, the parasitic capacitance is of major importance. The characteristics for the EM torque or speed performance is not considered at all due to that that part of the model is not necessary for the CM simulations. An EM has normally three windings that can be connected in a Y- or Delta connection, see figure 3.16. The DUT is a Y connected EM without midpoint accessible. The model developed is shown in figure 3.17. The model is simplified a lot. A more realistic model should include capacitance between each winding-turn and from each conductor to the stator and so on. However, looking at the impedance graph in figure 3.21, the impedance from phase to ground correlates well, even though a resonance is not visible in the model. The absolute impedance value is still quite close. The expected and measured CM currents is in the range of 1-10MHz. The CM capacitances in the EM are considered to be symmetrical, i.e. the same in all three phases. Aging of the winding can cause differences in the capacitance, but these differences are hard to predict. The measurements carried out for modeling purposes, were done on a new machine and the results showed that the parasitic capacitance for all three phases were almost identical.

NB! There are also parasitic capacitances from the stator winding to the rotor. The return path to the chassis/ground is via the bearings or the transmission. When measuring the parasitic capacitances in the EM in this thesis, the EM is at standstill. All capacitances are modeled from winding to chassis.

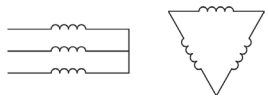

Figure 3.16: EM in a Y or Delta connection

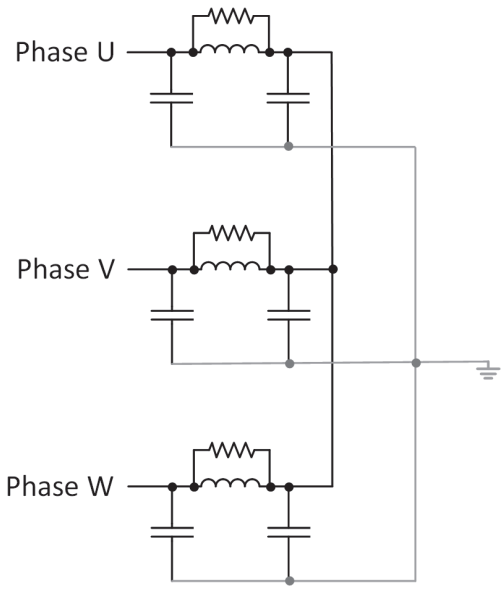

Figure 3.17: EM model structure adapted to the LCR measurement.

The frequency response is measured with the Kelvin and 4-wire method with separate current probe. The results from the Kelvin and ”separate current probe” measurements are used for low and high frequency modeling, respectively. The frequency response is measured in three different ways according to the list below and the results are compared to simulations:

- One phase to ground, see figure 3.18
- Phases to ground (Impedance from the phases to ground when all three phases are short circuited at the terminal and measured to ground), see figure 3.19
- Phase to phase, see figure 3.20

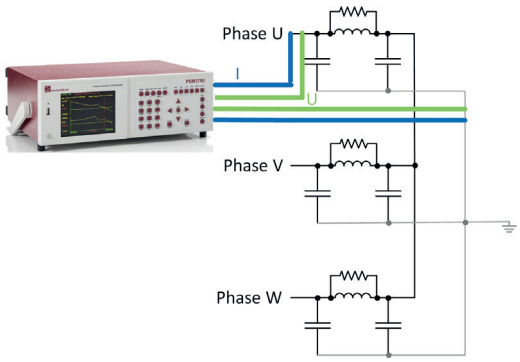

Figure 3.18: EM measured from one phase to ground.

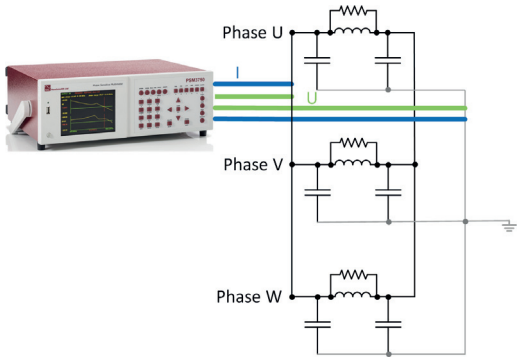

Figure 3.19: EM measured from all phases to ground.

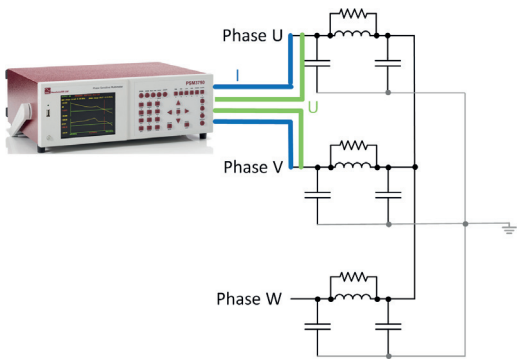

Figure 3.20: EM measured from phase to phase.

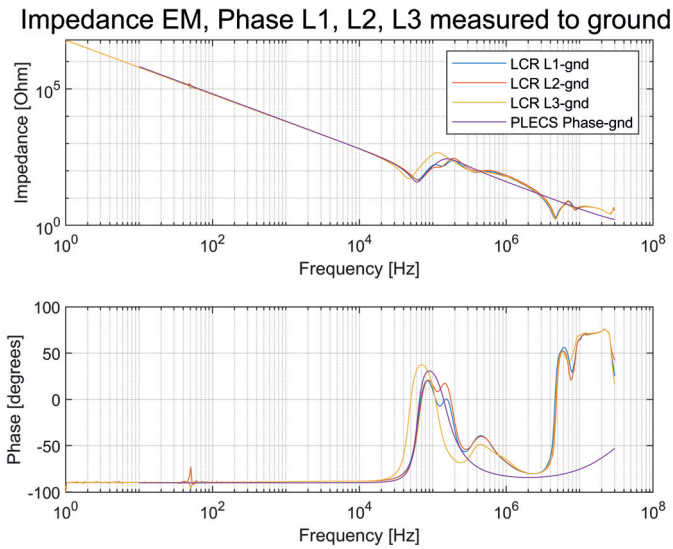

Figure 3.21: EM measured from phase to ground. All three phases L1, L2 and L3 are measured towards ground.

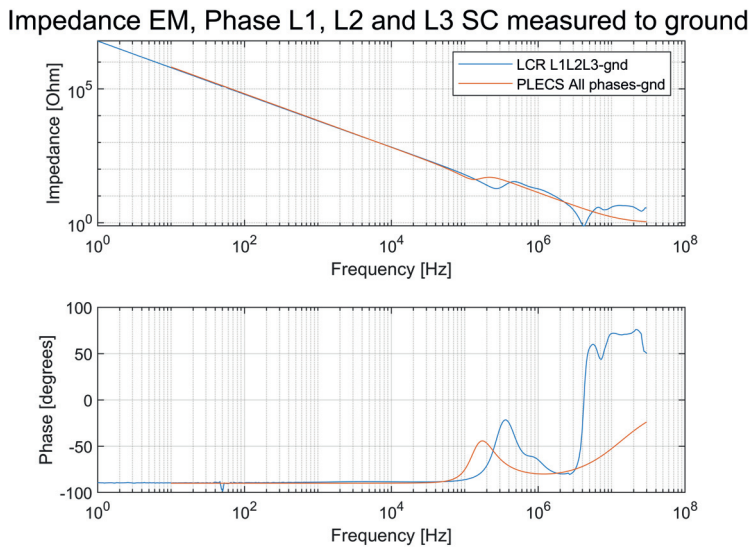

Figure 3.22: EM measured from phases to to ground. Phase L1, L2 and L3 are short circuited and measured towards ground.

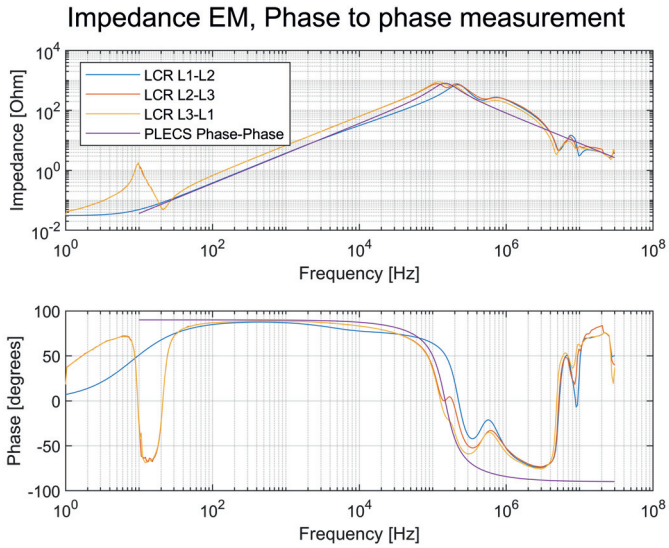

Figure 3.23: EM measured from phase to ground.

In appendix A it is shown how to derive parameters from LCR measurements. Looking at figure 3.21 it is found that the 2 phases are aligned (L1 and L2) and one phase differs. The same is found in figures 3.22 and 3.23. If the rotor is rotated the smallest possible angle, the same pattern will be found, another phase will differ from the other two. The cause for it is not investigated but found repeatable. The parameter that differs is the inductance. The model contains two equal inductances and one that differs. The ”resonance” point at 70kHz results from when the winding impedance dominates and the capacitance after the winding is ”blocked” bye the high impedance in the winding.
The resonance at approximately 4MHz is not found in the model due to the simplified model. However, at this high frequency and that the EM is at standstill the model can be found ”good enough”.

In figure 3.23 a huge deviation is found between 1-20Hz, the cause is not investigated due to that the frequency of interest for CM is in the 100kHz-10MHz range. Different measurement methods were tested and in this case, it was the 4-wire Kelvin method, as can be understood as the sweep starts at 1Hz. To rely on a low contact resistance a manual pressure is attached on the 4-wire Kelvin claws and that might be the cause for this deviation.

3.2.3 Measurements and modeling of the battery

The battery model is developed from both a DM and CM perspective. The interface described in 3.1.4 is used for the measurements. The complete model is developed with knowledge of the schematics from the supplier and a principal schematic is shown in the meas-

urement setup presented in figure 3.24. Measuring from positive pole to negative pole is shown in figure 3.24 and from pole to chassis is shown in figure 3.25. The corresponding impedance graph and frequency response of the developed model is shown for DM in figure 3.26 and for CM in figure 3.27.

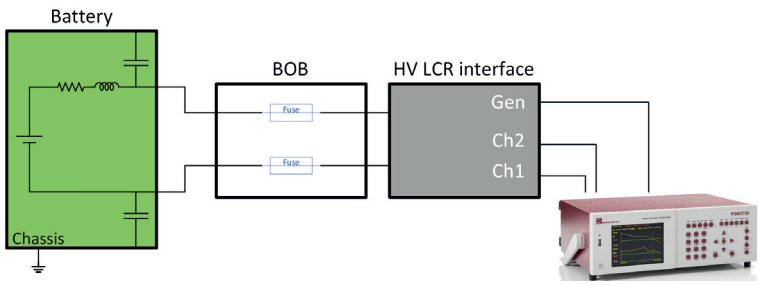

Figure 3.24: Measurement setup of the pole to pole impedance with a principal schematic of the battery.

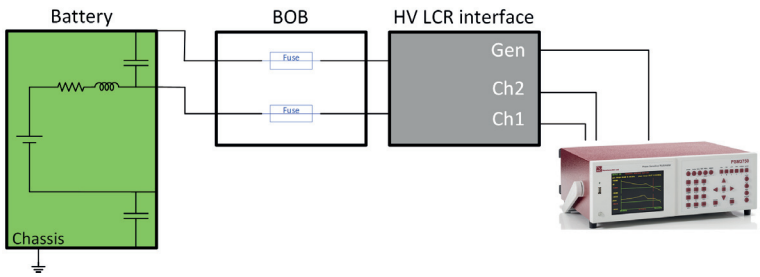

Figure 3.25: Measurement setup of the pole to ground impedance with a principal schematic of the battery.

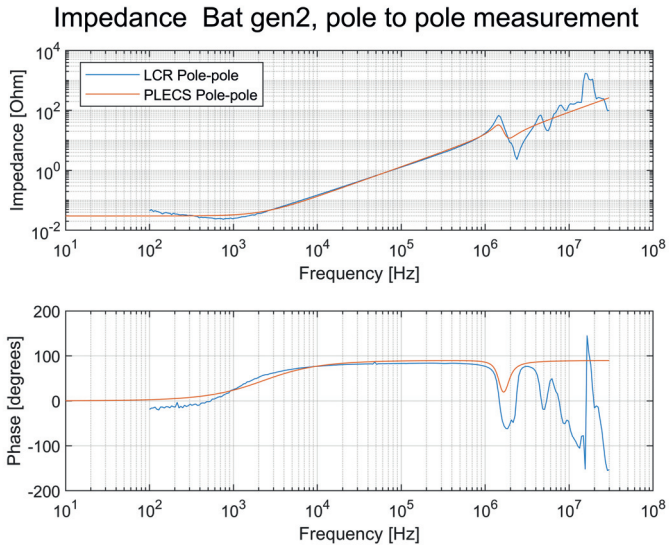

Figure 3.26: Battery gen2 measured from pole to pole.

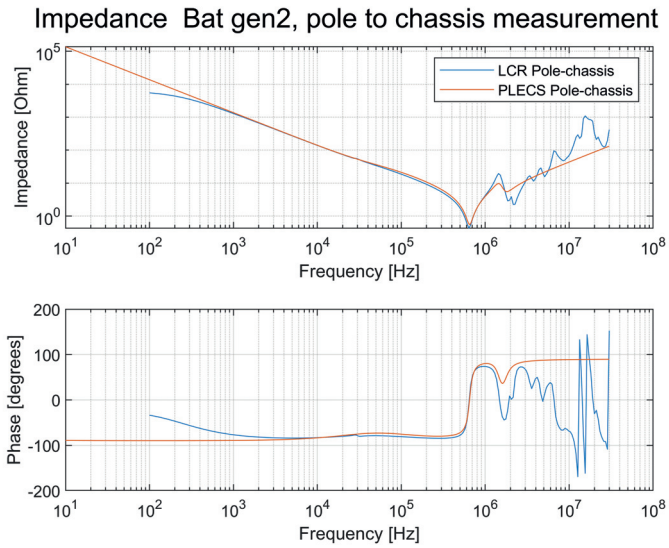

Figure 3.27: Battery gen2 measured from pole to ground.

With the knowledge, from measurements, that the CM currents in the battery is in the frequency range of 100-250kHz the model needs to be valid up to this frequency range. The measurement interface has an upper BW of 1MHz. In this frequency range the model has been developed and do match the measurement good.

The model of the battery, shown in a rough model in the left part of figure 3.24 and 3.25, is derived with support from simulation tools described in appendix A.

3.2.4 DCDC

The DCDC is a one-quadrant converter that supplies the 24 VDC system in the vehicle. The DCDC provides galvanically isolation between the TVS and the 24 VDC system as the 24 VDC system has a direct connection to ground. The power rating is in the range of 7kW. A simplified schematic of the DCDC is shown in figure 3.28.

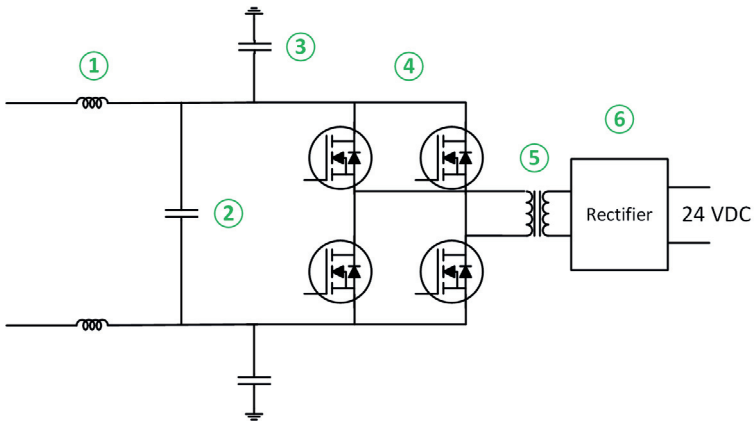

Figure 3.28: DCDC main circuit

The included major parts in the DCDC are:

1. Input filter. Reduces the CM currents.
2. DC link capacitor. Supplies and stores the switching power.
3. CM capacitor. Return path for CM currents.
4. H bridge. 2 phase legs.
5. Transformer that reduces the voltage as well as providing galvanic isolation.
6. Rectifier that rectifies and filter the ac current from the transformer.

The complete model over the DCDC is very complex and will not be shown here, however the simulations were performed with the full model, apart from the H-bridge, transformer and rectifier in figure 3.28. The complete simulation model in PLECS contains over 70 discrete components. The model, used in the simulations, is not used as operative, i.e. the modulation of the H-bridge is not active. There are 3 important measurements, according to figure 3.29,3.31 and 3.33, that shall correspond between the model and the measured values which are:

- Positive to negative pole, for the DM properties.
- Positive pole to vehicle chassis, for the CM properties.
- Negative pole to vehicle chassis, for the CM properties.

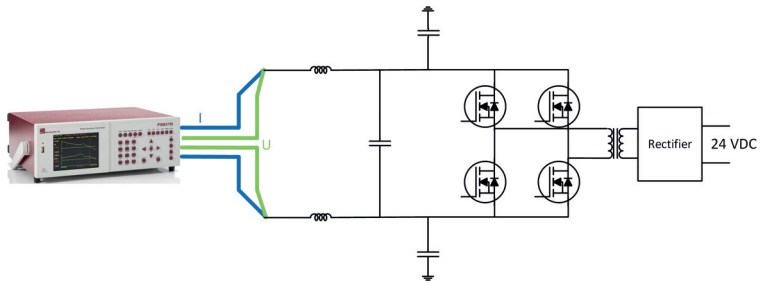

Figure 3.29: LCR measurement for the impedance and phase measured from positive to negative pole.

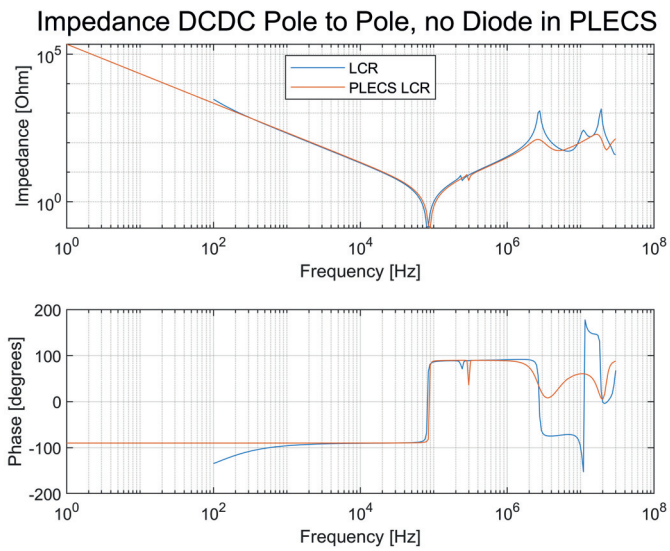

Figure 3.30: Impedance and phase as function of the frequency for the DCDC measured from positive to negative pole.

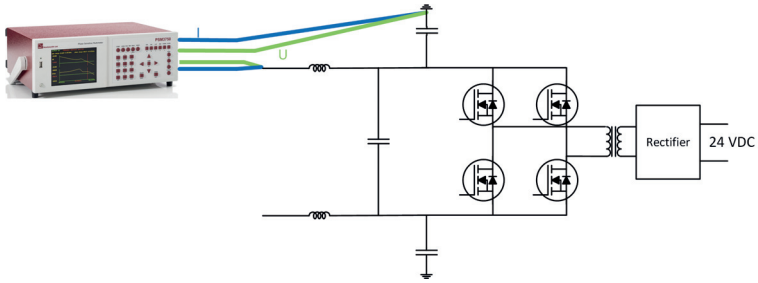

Figure 3.31: LCR measurement for the impedance and phase measured from positive pole to vehicle chassis.

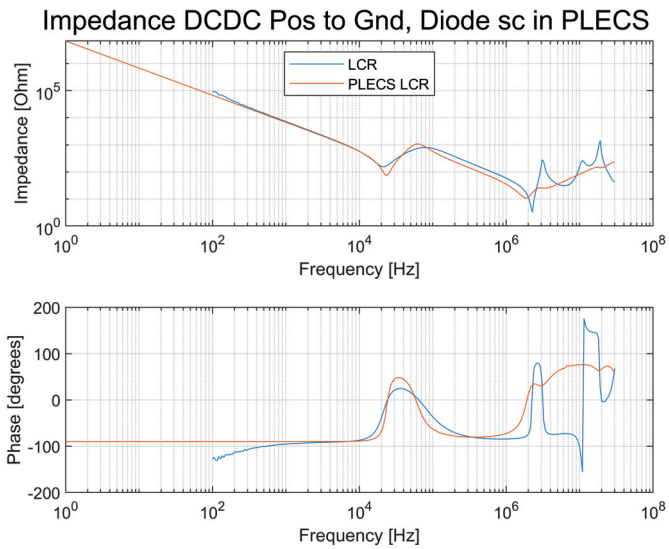

Figure 3.32: Impedance and phase as function of the frequency for the DCDC measured from positive pole to vehicle chassis.

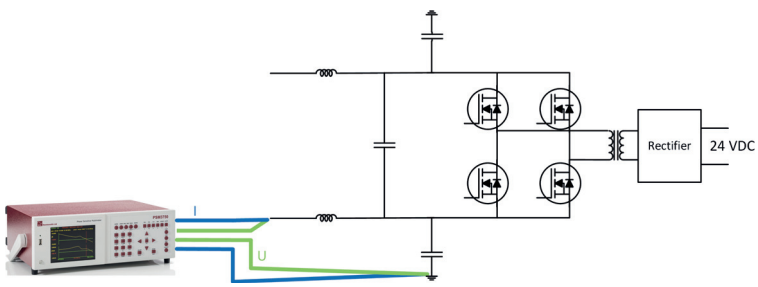

Figure 3.33: LCR measurement for the impedance and phase measured from negative pole to vehicle chassis.

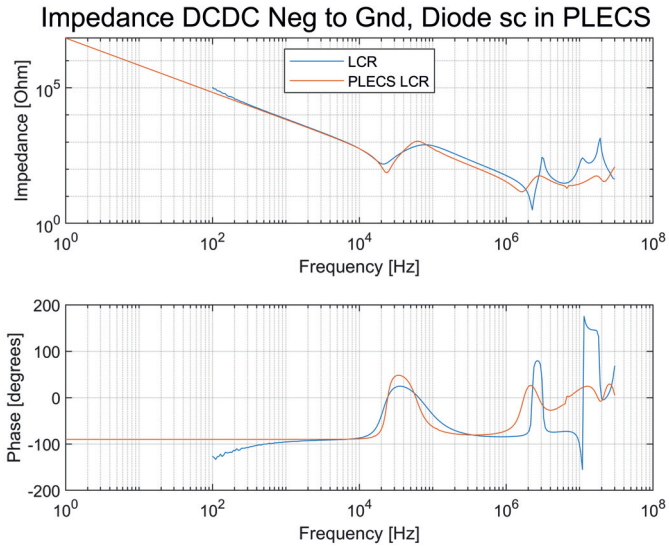

Figure 3.34: Impedance and phase as function of the frequency for the DCDC measured from negative pole to vehicle chassis.

The model of the DCDC, shown in a rough model in the left part of figure 3.28 is derived with support from simulation tools described in appendix A.

It is shown in figure 3.30, figure 3.32 and figure 3.34 that the measured impedance correlates with the model up to 2-3MHz for both DM and CM. Between 70 kHz and 2 MHz the model deviates around 30%.

3.2.5 On Board Charger (OnBC)

The OnBC is a one-quadrant converter that charges the TVS batteries in the vehicle. The OnBC provides galvanically isolation between the TVS and the grid and is only in operation at stand still when the electric traction machine(s) is deactivated. The power rating is in the range of 11kW. In some vehicles there are multiple chargers installed in parallel. A simplified schematic of the OnBC is shown in figure 3.35, note that the power in this picture is flowing from right to left.

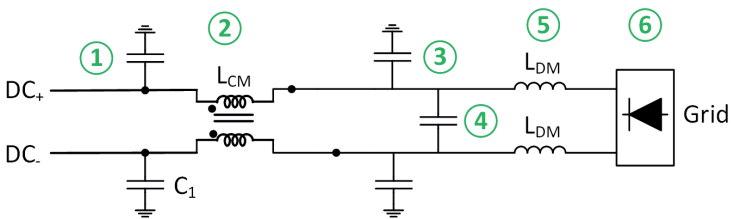

Figure 3.35: OnBC main circuit

The included major parts in the OnBC are:

1. CM capacitor. Return path for CM currents.
2. Output filter. Reduces the CM currents from the TVS to the OnBC.
3. CM capacitor.
4. DC link capacitor. Filter the output voltage.
5. Inductive input filter that smooths the output current.
6. Rectifier from the transformer that isolates the grid from TVS

The complete model over the OnBC is very complex and will not be shown here, however the simulations were performed with the full model, but not including the transformer and rectifier. The complete simulation model in PLECS contains over 120 discrete components. As for the DCDC model, this model is used only as a passive load. There are 3 important measurements of the impedance:

- Positive to negative pole, for the DM properties.
- Positive pole to vehicle chassis, for the CM properties.
- Negative pole to vehicle chassis, for the CM properties.

The connection of the LCR meter is accordingly to previous subsections.

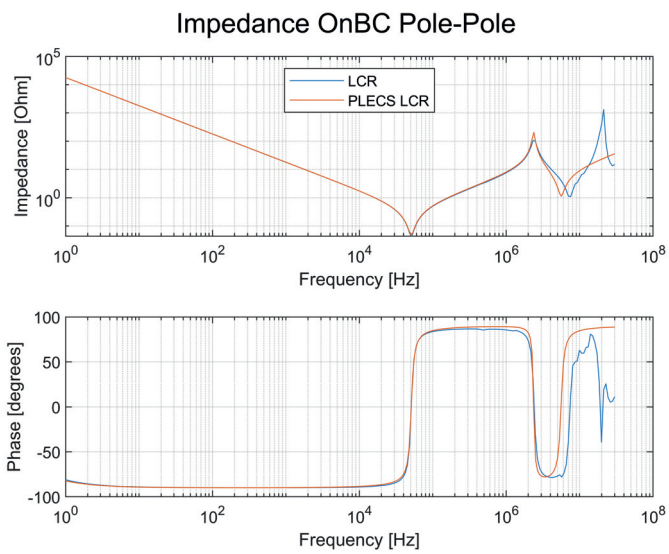

Figure 3.36: Impedance and phase as function of the frequency for the OnBC measured from positive to negative pole.

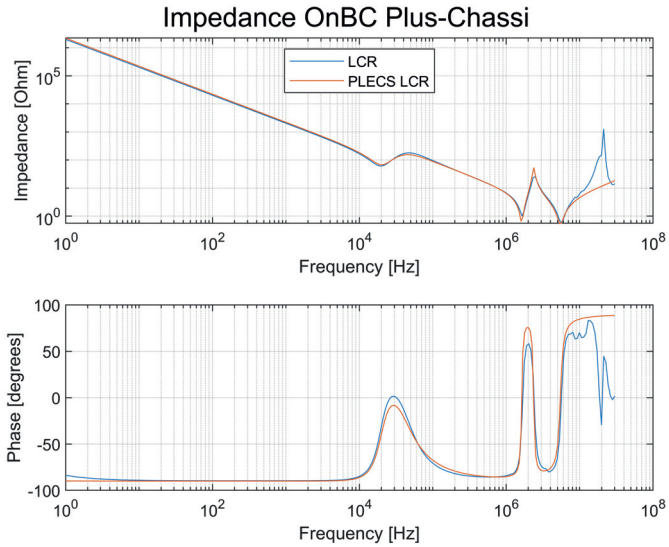

Figure 3.37: Impedance and phase as function of the frequency for the OnBC measured from positive pole to vehicle chassis.

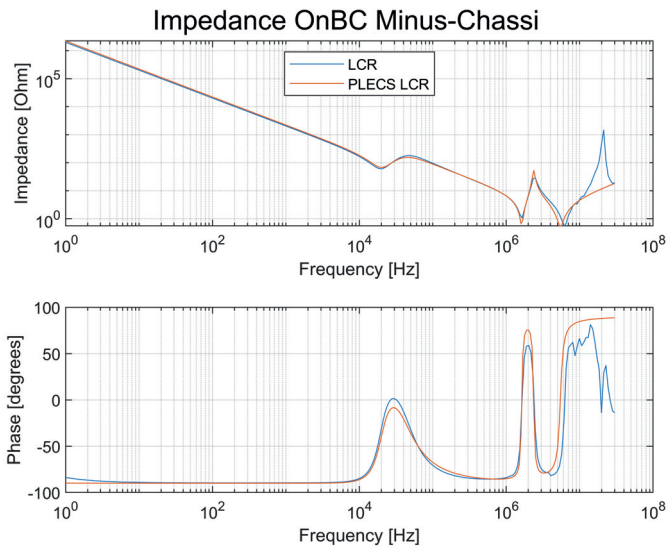

Figure 3.38: Impedance and phase as function of the frequency for the OnBC measured from negative pole to vehicle chassis.

The model of the OnBC, shown in a rough model in the left part of figure 3.35 is derived with support from simulation tools described in appendix A.

It is shown in figure 3.36, figure 3.37 and figure 3.38 that the measured impedance correlates with the model up to 5 MHz for DM and up to 10 MHz for CM. The deviations

above 10 MHz cannot be handled due to the uncertainty in measuring at high frequencies.

3.2.6 Cables

The 600 V cables in the vehicle are either of coaxial or twin-axial type. The twin axial cable supplies the low power loads, and the coaxial cables supplies the high power loads, the cables are shown in figure 3.39.

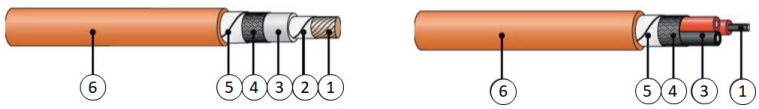

Figure 3.39: Coaxial and multi-core cable from Huber + Suhner. The cable used in the vehicles is with two conductors and the one in the picture has three. Picture from Huber + Suhner.

The cable is built up according to the following list:

1. Conductor
2. Tape
3. Insulation
4. EMC screen
5. Tape
6. Sheath

The investigation of the cable properties is made in a master thesis work during this research, [5]. In the master thesis the aim was to build a cable model that fits with the LCR measurements and to calculate the same parameters by modeling in COMSOL, [4]. The challenge with the models were to find required parameters and to simplify the models to be as small as possible. Simulating the vehicle with all subsystems and cables ends up in a large and very complex model. If all subsystems, including cables, are too detailed the model will not be possible to solve by the simulation program.
In this subsection, a full cable model will be presented together with a simplified model considered to have an acceptable accuracy for further use.

How the different parameters and complete model is built is described in the master thesis, [5].
The full model, see figure 3.40, is built as a PI model where the parameters are divided symmetrically around the inductance and resistance. Therefore, some of the parameters are divided by 2. The model contains the following parameters:

Rc Conductor resistance
Rs Shield resistance
Ccs Capacitance between conductor and shield. parasitic capacitance
Lm Self and mutual inductance of the conductor and shield
Csg Capacitance between shield and ground. parasitic capacitance
Lg Self-inductance of the ground plane
Rdummy Dummy resistance to avoid infinite voltage or current. Rdummy for capacitors is nΩand for

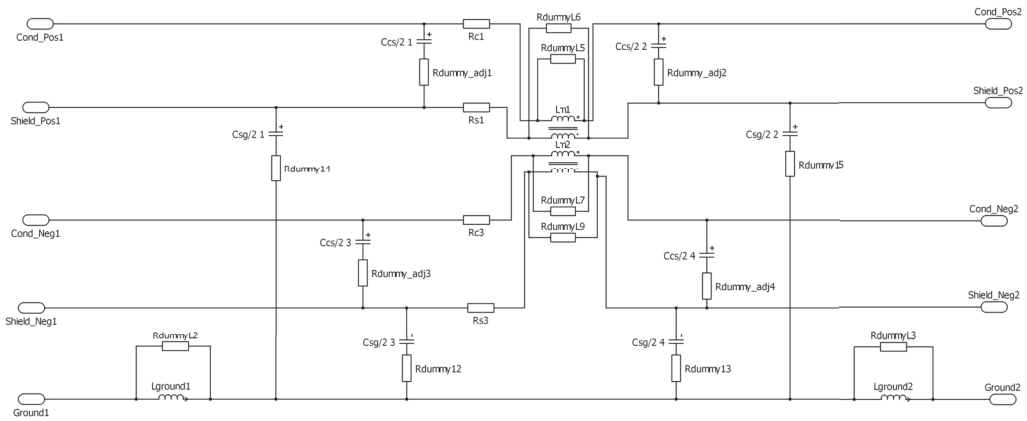

Figure 3.40: Full model of the coaxial cable

Apart from shielding the conductor and reduce emitted disturbances the shield also provides a low impedance return path for CM currents. A common way to build models is to introduce simulation ground connection ”everywhere”. That will shortcut the return path of the shield. This model contains a ground impedance Lg.

Simplifications

The model of figure 3.40 is complex. By comparing parameters in the cable model to the corresponding parameters of the connected subsystems, some simplifications can be made. The measured parasitic capacitance between the shield and ground is in the range of 0.2 nF/m. Assume a large vehicle with 50 m of coaxial cables, the total parasitic capacitance Csg will be in the range of 10nF. The potential of the shield to ground is low and a current flowing in Csg can be assumed to be very low and the Csg can be omitted in a medium simplified model, see figure 3.41.

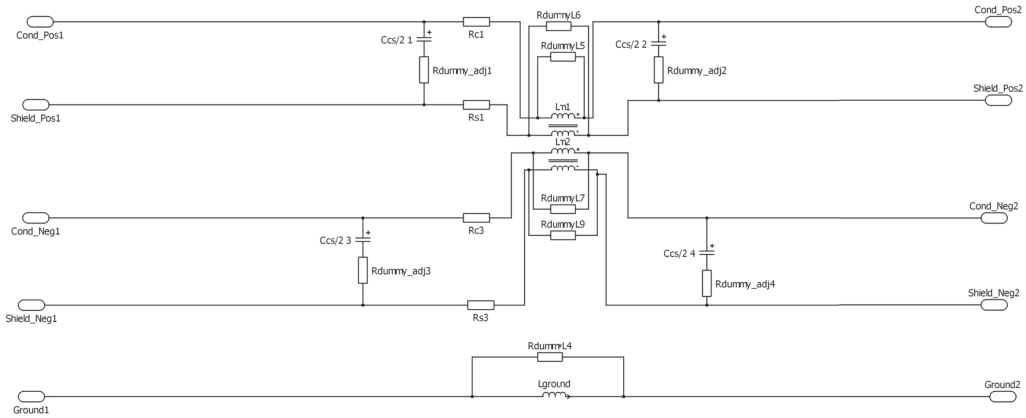

Figure 3.41: Medium model of the coaxial cable, where the C_{sg} is omitted.

The parasitic capacitance between the conductor and the shield is int he range of 0.6nF/m. A typical cable between battery and converter is 1-10m long which gives a total parasitic capacitance from pole to shield of 0.6-6nF. The parasitic capacitance to ground in high power subsystems is in the range of 50-500nF. In comparison the cable parasitic capacitance can also be omitted to even further reduce the model. This will also give the advantage of combining the split Lg as well. The minimum model is shown in figure 3.41.

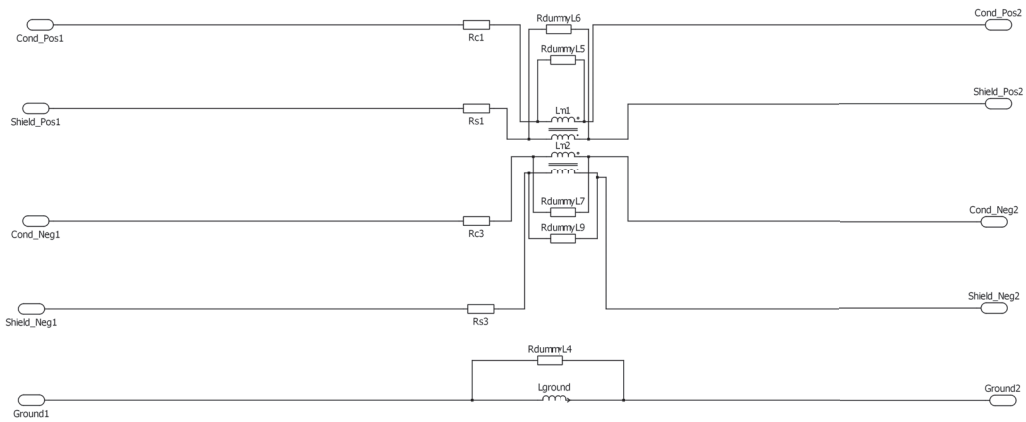

Figure 3.42: Minimum model of the coaxial cable, where the C_{cs} is omitted as well.

Cable measurements - L_{11}

The next step is to compare the different models with the measured data. The first comparison, figure 3.44, is the impedance of the conductor with open shield, L_{11}, see figure 3.43. It is found that the different cable models of figure 3.40-3.42 gives the same result up to 4MHz. Above 4MHz all models deviate to some extent. The minimum model of figure 3.42 do not deviate more than the full model of figure 3.40, up to 10MHz.

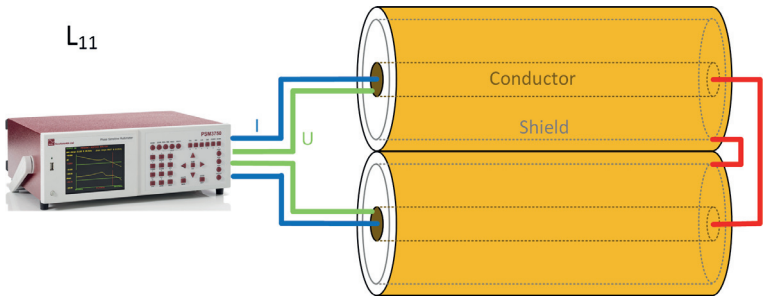

Figure 3.43: Measurement of the conductor impedance.

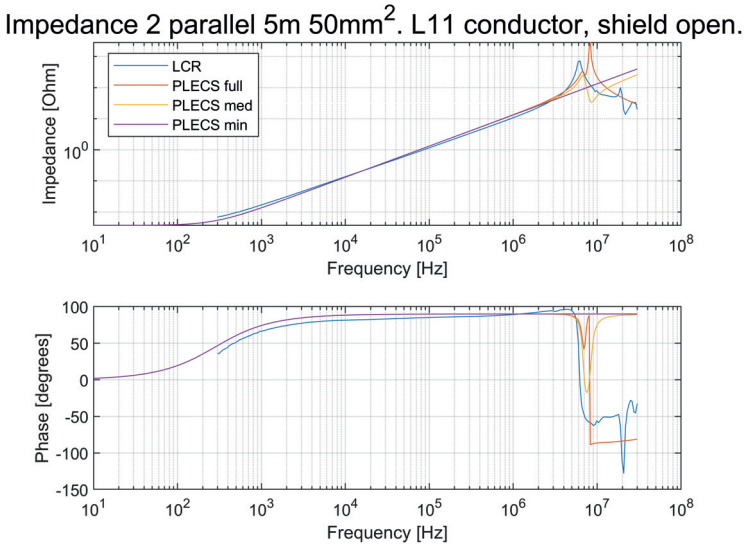

Figure 3.44: Comparison of the impedance from measurement and from the three different models.

Cable measurements - Lc

The second comparison is the self-inductance, figure 3.46 of the conductor, which is obtained when the shield i short circuited, see figure 3.45. It is found that the full model of figure 3.40 and medium model in figure 3.41 gives exactly the same result. The different models give the same result up to 4MHz. The full and medium models are close to the measured graph. This current path is used for DM currents and accuracy up to 1MHz is good enough. This implies that without the minimum model can be used losing to much valuable information.

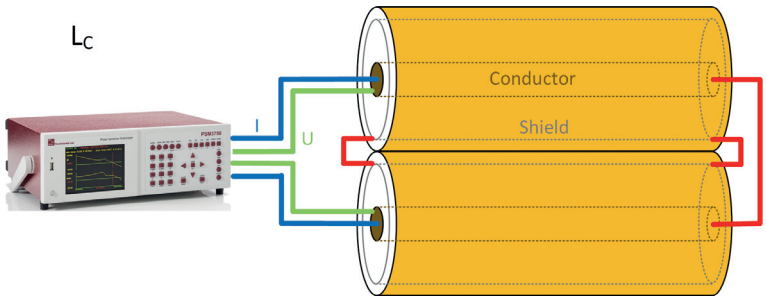

Figure 3.45: Measurement of the conductor self-inductance.

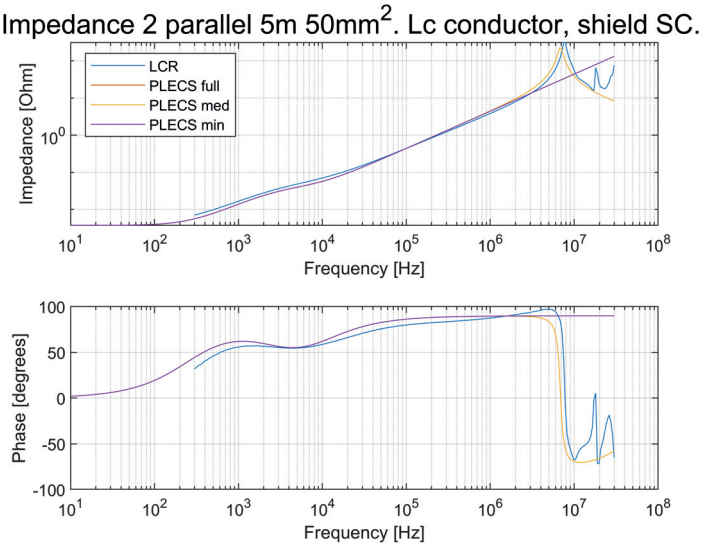

Figure 3.46: Comparison of the impedance from measurement and from the three different models.

Cable measurements - L_{22}

The third comparison is the shield impedance, figure 3.48 of the conductor, which is obtained when the shield i short circuited, see figure 3.47. It is found that the medium and minimum model gives exactly the same result. Above 4MHz both the minimum and full model deviates to some extent from the measured graph. It is still not a bad choice to choose the minimum model.

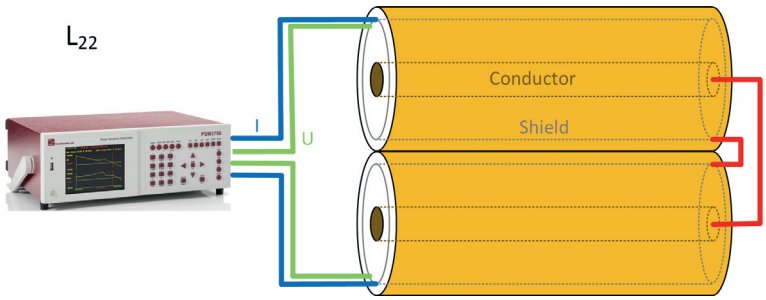

Figure 3.47: Measurement of the shield inductance.

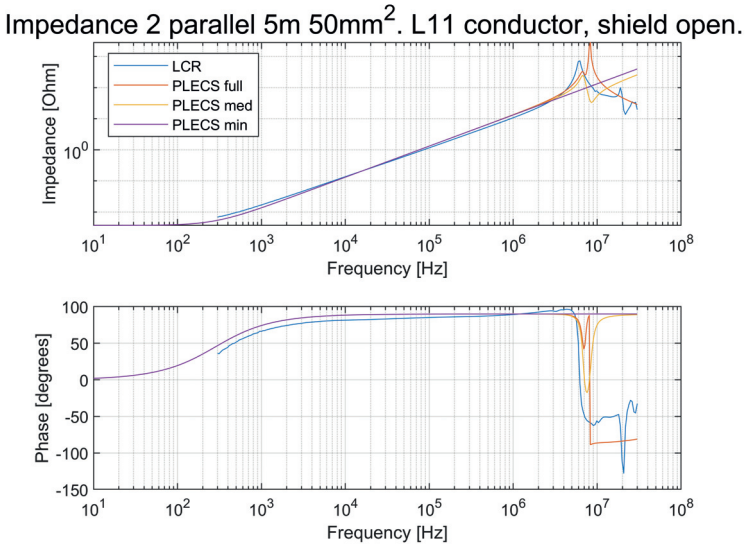

Figure 3.48: Comparison of the impedance from measurement and from the three different models.

Cable measurements - L_{11}-L_{22}

The fourth comparison is the conductor plus the shield impedance, figure 3.50 of the conductor, which is obtained when the shield i short circuited, see figure 3.49. It is found that the full and medium model gives exactly the same result. The different models give the same result up to 1MHz. Between 1-3MHz the minimum model is most accurate. Above 3MHz all models deviate about the same from the measured graph. The minimum model can be chosen here as well.

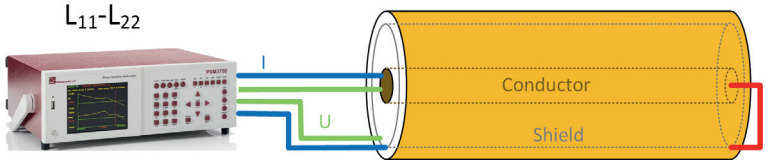

Figure 3.49: Measurement of the shield inductance.

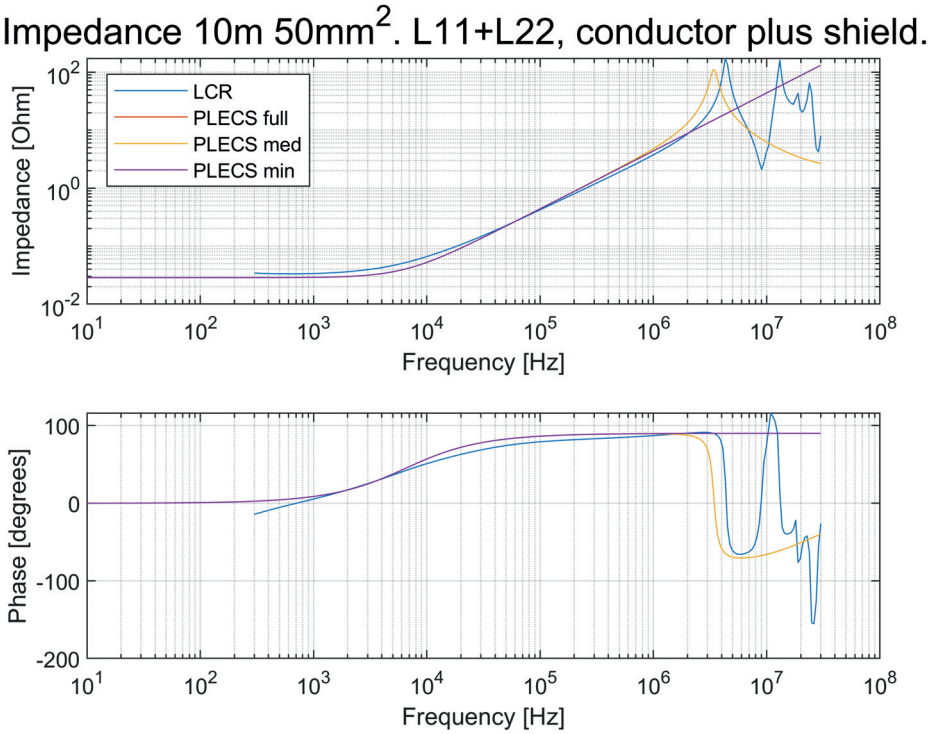

Figure 3.50: Comparison of the impedance from measurement and from the three different models.

Cable measurements - L_{11}+Lg

The fifth comparison is the conductor plus the ground impedance, figure 3.52 of the conductor which is obtained when the shield is connected to ground, see figure 3.51. To show the importance of a separate ground impedance a comparison of the ground and shield impedance is shown in figure 3.53. The different models give the same result up to 2MHz. Above 2MHz the full model is most accurate even though the shape of the graph ha an offset in the frequency. The best choice here is the full model.

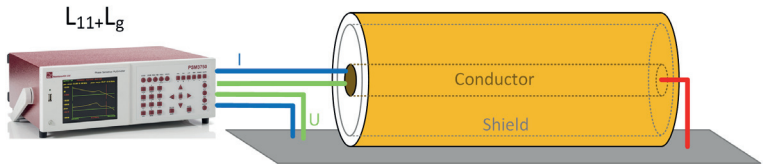

Figure 3.51: Measurement of the ground inductance.

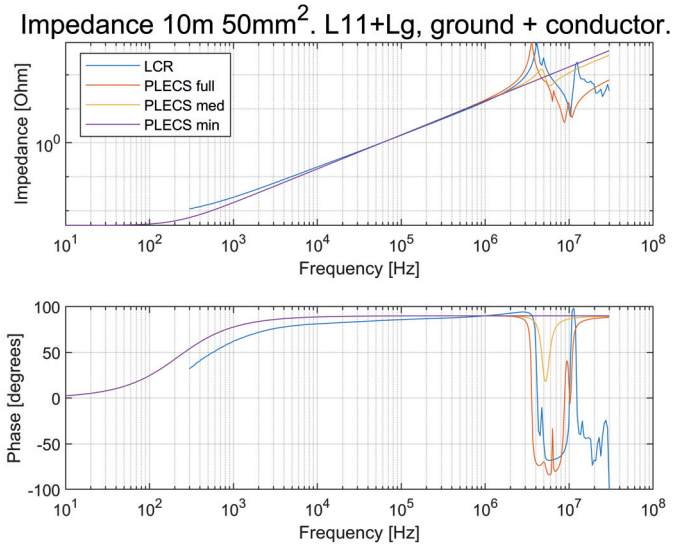

Figure 3.52: Comparison of the impedance from measurement and from the three different models.

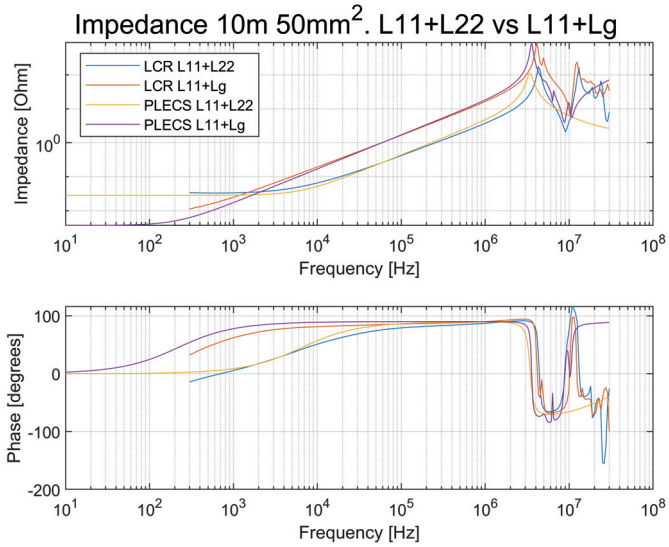

Figure 3.53: Comparison of the impedance between ground and shield impedance.

Cable measurements - Ccs

The sixth and last comparison is the conductor to shield parasitic capacitance in figure 3.54 and figure 3.55. This model is not valid for the minimum model as the Ccs is removed in this model. It is found that the full and medium model gives exactly the same result. It is obvious that the minimum model gives a poor result here as the Ccs is removed from the circuit.

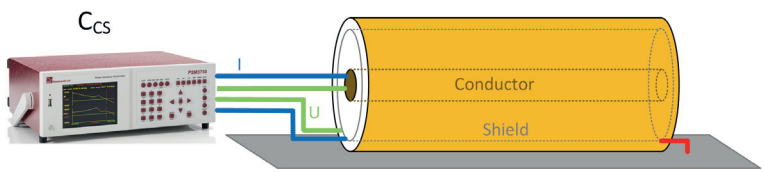

Figure 3.54: Measurement of the shield to conductor parasitic capacitance.

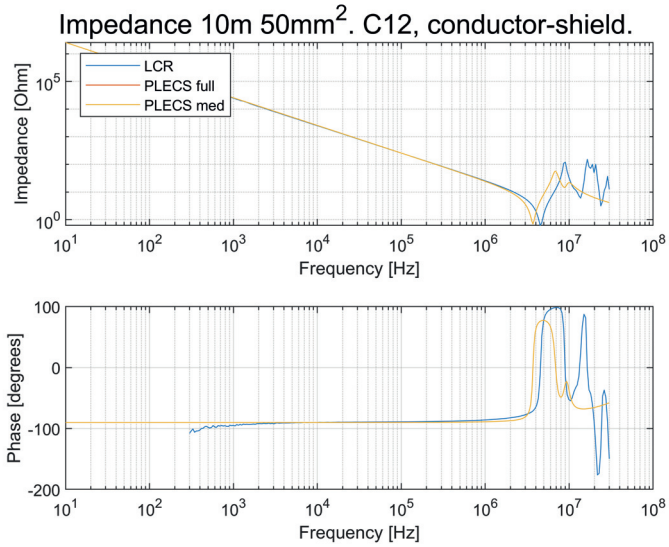

Figure 3.55: Comparison of the impedance from measurement and from the two different models.

Concluding the different models, an attempt to use the less complex model in favor to a more complex model is prioritized. A more complex cable model gives a (too) complex system simulation model and is harder for the simulation program to solve. Also, the simulation time is increased and thereby complicate one of the beauties of simulation; the ability to see relative changes in a model based on numerous gradual changes.

Chapter 4

System simulation

The models for the subsystems are in chapter 3 developed and compared to the LCR measurements to confirm the accuracy. In this chapter, these sub system models are combined to form a bigger part of a TVS and simulated together. The frequency band of interest is, as mentioned before, 100kHz for DM and 10MHz for CM. The system behavior of the CM simulations is very sensitive to small details in the subsystems. Very small changes of values (part of nF and nH) on parasitic capacitances and stray inductances may lead to significant changes in the sub system behavior. The accuracy of the system simulation is in conflict with the detailed resolution of e.g. a semiconductor. During the work with this thesis, it has become obvious that a full vehicle model cannot be simulated with all sub system details represented, not even in days or weeks. It is also found in the simulations and measurements that the HF properties stays within the subsystem. The neighboring subsystems are affected in a lower frequency range by a common mode DC voltage that connect different subsystems via shared impedances in the system.

4.1 Results from CM Simulations

In the simulations presented here the results are limited to reduced system complexity to investigate the cause and effects of the CM mode disturbances caused by the switching of the EMD and how the disturbances best can be reduced.

The PLECS models contain the details mentioned in chapter 3. For the investigation of the distribution of CM currents presented here a simplified system model is used, with a limited set of subsystems. The system contains one traction battery, DC cables, one EMD, three phase cables and one EM. The reason for this limitation is that the full system, according to Fig. 2.1, cannot be simulated with the selected system simulation tool and frequency range, due to too high complexity. The source of the CM disturbances is the interaction between the 3-phase converter and the parasitic capacitances to ground in the 3-phase cables and the EM windings. When the EMD switches, the parasitic capacitances

mentioned are altered between 4 asymmetric states (000, 111, one phase switch up and 2 phase switches up, the sequence of which depends on the modulation method). That also means that the electric potentials of the battery terminals to chassis varies slightly depending on switch state, which drives CM currents through the EM windings. The return paths for the CM current is the CM-capacitances in the EMD, the DC-cable and battery, see Fig. 4.1. The worst case appears when the EMD switches all phases simultaneously, which corresponds to a zero output Voltage of the converter, i.e. state (000) and (111). The CM voltages are defined in Fig. 4.1.

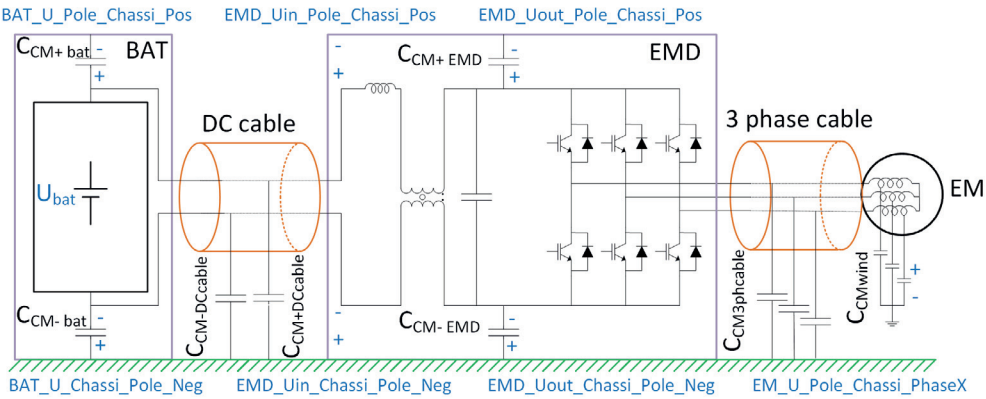

Figure 4.1: Circuit diagram for simulation with CM voltage references. Capacitance definition for the subsystem CM-capacitances.

The return paths for the CM currents are shown in Fig. 4.2. All currents have the same reference direction (from battery to load, from chassis to TVS and load) as it simplifies keeping track of the inbound and outbound currents. The name conventions are shown in the figures.

The battery circuit is modeled as a voltage source with series inductance and resistance and intentional CM-capacitors connected from the positive or negative TVS pole to chassis. The sum of all CM currents (all red arrows in Fig. 4.2) shall be zero which is confirmed in the simulation model.

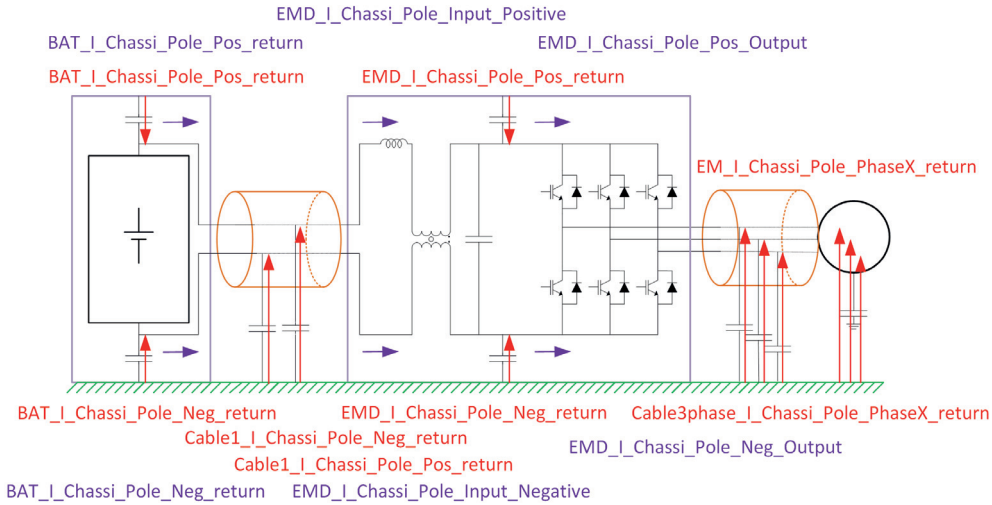

Figure 4.2: Circuit diagram with different CM currents denoted with color coded arrows, used in Fig. 4.7, Fig. 4.8 and Fig. 4.9.

The simulations presented in this thesis shows that the common mode currents are asymmetrically distributed across the positive and negative TVS conductors. The winding-to-core capacitances in the EM are asymmetrically distributed relative to the DC link by means of modulation, i.e. the connection of these parasitic capacitances vary with the switch states. This result in a Common Mode DC voltage (CMDC) which changes level due to the asymmetrically distributed CM-capacitance ($C_{CM3phcable}$ and C_{CMwind} according to Fig. 4.1) and an asymmetrically distributed (between the positive and negative sides of the TVS) CM current, both of which are described in the following subsections.

Fig. 4.3 is an alternative representation of Fig. 4.1 looking at the CM-capacitances.

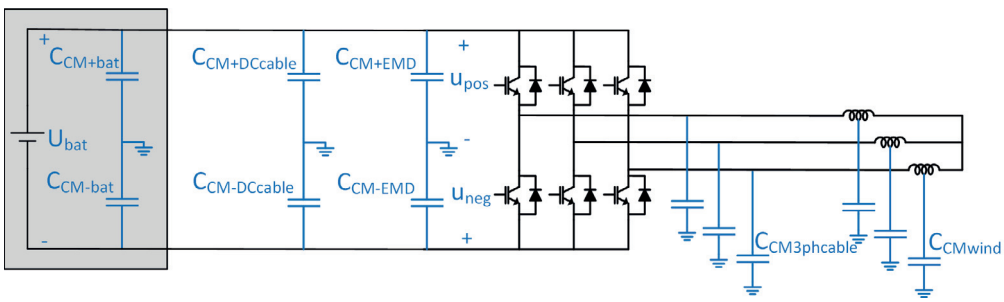

Figure 4.3: Equivalent circuit diagram for the CM-capacitances.

At standstill, with a zero output voltage, the CMDC voltage is a square wave and becomes quasi square waves when the EM rotates or with a system with more than one EM with non-synchronized modulation of the EM drivers. The said CMDC square or quasi square voltage is referred to as the CMDC voltage in this thesis.

4.1.1 CMDC voltage - cause and effect

The CM voltage is defined as follows.

$$u_{cm} = \frac{u_{pos} + u_{neg}}{2} \tag{4.1}$$

The cause for the CMDC voltage is the winding-to-core capacitance of the EM and cable-to-shield capacitance of the three phase cable, denoted as C_{asym}.

$$C_{asym} = C_{CM3phcable} + C_{CMwind} \tag{4.2}$$

As C_{asym} is asymmetric to either the positive or the negative pole of the TVS, the sum of the winding-to-core capacitances and the cable-to-shield capacitances of the three phase cable towards the positive or negative poles of the TVS, is asymmetric relative to the DC link given a certain switch state, see Fig. 4.3. The sum of the CM-capacitances in this example, the battery, in the DC cable and the EMD included but the EM and the three phase cables excluded, is here denoted as C_{pn}.

$$\begin{aligned} C_{pn} = C_{CM+bat} + C_{CM+DCcable} + C_{CM+EMD} = \\ C_{CM-bat} + C_{CM-DCcable} + C_{CM-EMD} \end{aligned} \tag{4.3}$$

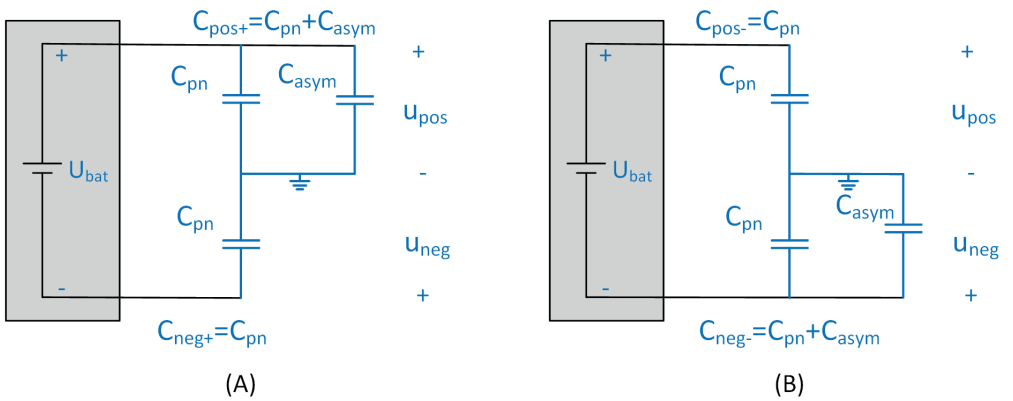

Figure 4.4: Equivalent circuit diagram for the CM-capacitances where (A) C_{asym} is asymmetric to positive or (B) C_{asym} is asymmetric to negative pole of the TVS. C_{pos+} and C_{neg+} are the capacitances at switch state (1,1,1) and C_{pos-} and C_{neg-} at switch state (0,0,0).

Two different configurations are presented below where the CM-capacitances, C_{CM+EMD} and C_{CM-EMD} (see Fig. 4.3) are simultaneously changed with a factor of 10 in the EMD. The CM-capacitance of the EMD is intentionally changed a factor 10 to give a significant but realistic change of the balance between the CM-capacitances of the EMD and EM to

see how the CM voltages changes, see Fig 4.5. The total symmetrical CM-capacitances (C_{pn}, in (4.3), Fig. 4.4) in the system is related to the asymmetrical CM-capacitances (C_{asym}, in (4.2), Fig. 4.4). The ratio between them is:

$$X = \frac{C_{pn}}{C_{asym}} \tag{4.4}$$

The sum of the symmetrical CM-capacitances, in the first configuration, is obtained in an unaltered vehicle and results in $X_1 = 6.9$ using (4.4). In the second configuration, with the 10x increased value of the CM-capacitance in the EMD the corresponding value becomes $X_2 = 37$. When all three phases of the EMD are connected to the positive pole (switch state (1,1,1)) of the TVS the total CM-capacitance towards the positive TVS pole is:

$$C_{pos+} = C_{pn} + \frac{C_{pn}}{X} = C_{pn} + C_{asym} \tag{4.5}$$

and simultaneously the total CM-capacitance towards the negative TVS pole is:

$$C_{neg+} = C_{pn} \tag{4.6}$$

When all phases of the EMD are connected to the negative TVS pole, switch state (0,0,0), the total capacitance from poles to chassis in the TVS swaps asymmetry.
The corresponding voltages when all phases of the EM winding is connected to the positive pole of the TVS are:

$$u_{pos} = \frac{U_{bat}}{C_{pn} + C_{pos+}} * C_{pn} = \frac{U_{bat}}{2 + \frac{1}{X}} \tag{4.7}$$

$$u_{neg} = \frac{-U_{bat}}{C_{pn} + C_{pos+}} * C_{pos+} = \frac{-U_{bat} * (1 + \frac{1}{X})}{2 + \frac{1}{X}} \tag{4.8}$$

The "stationary" CM voltage, when all phases of the EM winding is connected to the positive pole of the TVS are:

$$u_{cm} = \frac{u_{pos} + u_{neg}}{2} = \frac{-U_{bat}}{2} * \frac{1}{2 * X + 1} \tag{4.9}$$

The "stationary" CM voltage, when all phases of the EM winding is connected to the negative side of the TVS are:

$$u_{cm} = \frac{U_{bat}}{2} * \frac{1}{2 * X + 1} \tag{4.10}$$

The CMDC voltage, illustrated for *BAT_U_CM* in Fig. 4.5 but is the same for *EMD_Uout_CM* and *EMD_Uin_CM*:

$$u_{CMDC} = \frac{U_{bat}}{2 * X + 1} \tag{4.11}$$

The CMDC voltage amplitude is illustrated for *EMD_Uout_CM* in Fig. 4.5 and is presented for *EMD_Uout_CM*, *EMD_Uin_CM* and *BAT_U_CM* in Fig. 4.5 for two different simulations. For voltage definitions and references see Fig. 4.1.

In the following graphs the trace color is green for $X_1 = 6.9$ and blue for $X_2 = 37$.

For $X_1 = 6.9$ the $u_{cm} = 20V$ or $u_{cm} = -20V$ depending on switch states which results in a CMDC voltage $u_{CMDC} = 40V$. For $X_2 = 37$ the $u_{cm} = 4V$ or $u_{cm} = -4V$ depending on switch states which results in a CMDC voltage $u_{CMDC} = 8V$. See Fig. 4.5.

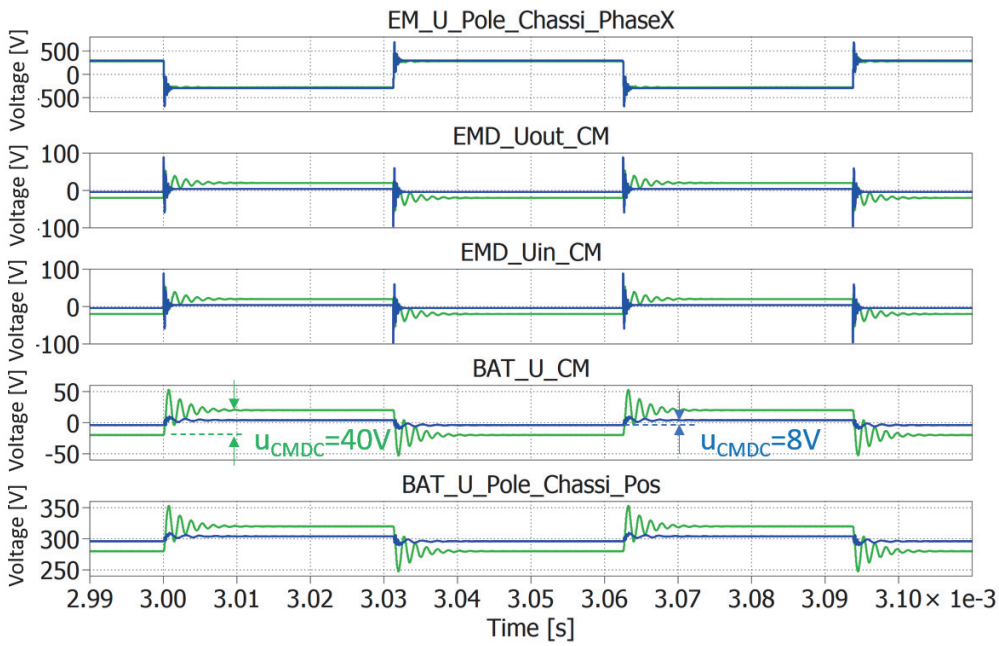

Figure 4.5: CMDC voltage caused by asymmetries where $X_1 = 6.9$ (green) and $X_2 = 37$ (blue)

Comparing the two different simulations in Fig. 4.5 in an expanded view in Fig. 4.6 it is obvious that the peak of the ringing almost disappears when the CMDC voltage is decreased at the battery, see the green and blue arrows in Fig. 4.6. Since the battery should be protected from EMI a proper relationship between the parasitic capacitance in the EM and the CM-capacitance in the EMD must be obtained, see an expanded view in Fig. 4.6. The green graph is when $X_1 = 6.9$ and blue for $X_2 = 37$.

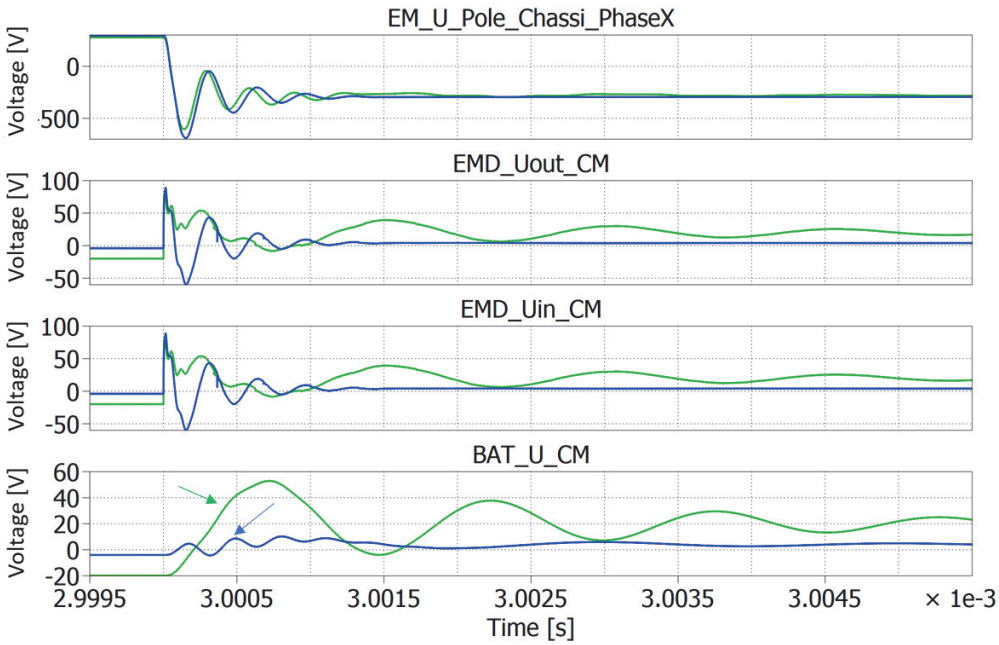

Figure 4.6: Voltage overshoot at the battery. Blue trace for 10x increased CM-capacitance in the EMD.

The real reason for increasing the CM-capacitance in the EMD and not in the battery is that the CM current via the EM shall be returned to the source as close as possible to where it is emitted, i.e. if the CM current leaves the EMD via the EM three phase cable capacitance $C_{CM3phcable}$ and the EM winding-to-core capacitance C_{CMwind} it should return to the EMD capacitance C_{CM+EMD} and C_{CM-EMD}. If the CM-capacitance is increased in the battery instead, the CM current flows a longer distance in the vehicle.

From this observation, with reduced U_{CMDC} and reduced CM current, a rule of thumb for any EMD-EM-combination is that the EMD CM-capacitance to chassis should be at least 50 times higher than the CM-capacitance of the EM as important is that this is valid for any type of TVS. This conclusion aligns with [13]. However, requirements on the maximum total CM-capacitance in the system is regulated by standards [12], [10] and decreases the freedom to arbitrarily chose the CM-capacitances. If this limitation by standards did not exist, the CM-capacitance in each converter could easily be adapted to meet the ratio of X=50. Designing commercial electrical vehicles is a tradeoff to achieve an acceptable level of the CMDC voltage and corresponding peak voltage.

4.1.2 CM currents - asymmetrical CM currents

The same simulations as above are made, with the same color coding of traces, from a CM current return paths and amplitude perspective. The CM currents are in general seen as currents of the same amplitude and direction in the positive as in the negative TVS con-

ductor. More correct is that the CM current is the current in the ground and is returned to the source via the positive and negative TVS conductor but not necessary equally distributed. In Fig. 4.7 it is shown that the CM current in the battery is decreased when the CM-capacitance is increased in the EMD. It is also seen that the difference between the positive and negative CM currents in the battery is not zero, e.g., not equally distributed.

Looking at the CM current from the EMD to the three phase cables and EM, see Fig. 4.9, it is found that the EMD outbound CM currents are more equally distributed in the positive and negative conductor when $X_2 = 37$ than for $X_1 = 6.9$.

It is obvious from the simulations illustrated by Fig. 4.8 and Fig. 4.9 that the CM current in the DC link distributes unevenly between the TVS poles. This is a result of the unsymmetrical load-to-ground capacitances, here mainly due to the EM winding to core capacitances. The means to minimize these currents can be right sizing the EMD CM-capacitance. Active means are also possible [18] as well as passive with CM chokes [17].

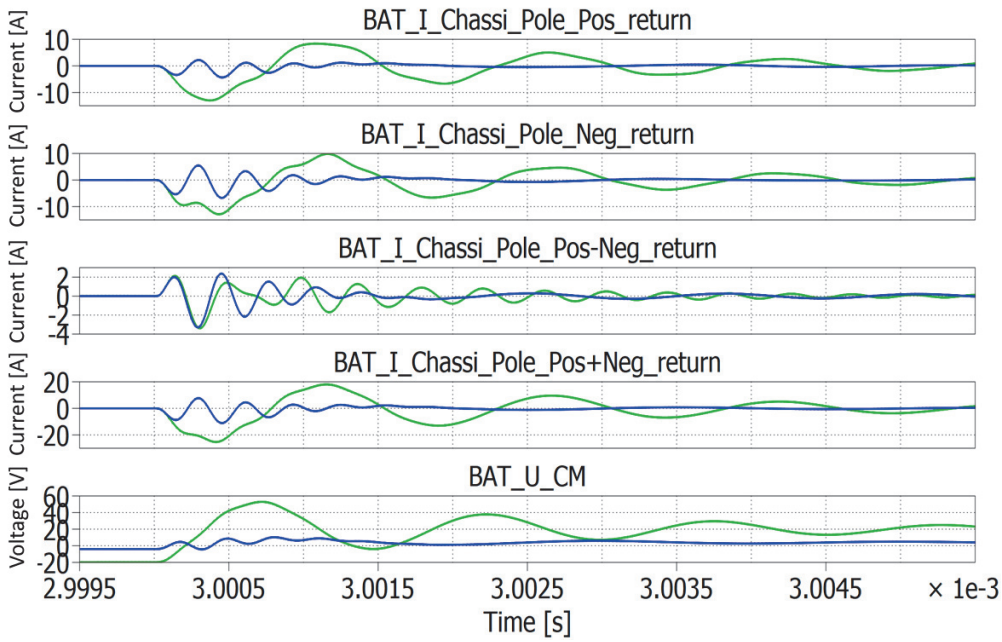

Figure 4.7: Comparison between CM current in the battery for two different CM-capacitance values in the EMD. Green graph is for $X_1 = 6.9$ and blue for $X_2 = 37$. The increase of C_{pn} is made by increase of the CM-capacitance in the EMD. NB! The 3rd diagram from the top shows that the CM currents to the battery are asymmetrically distributed.

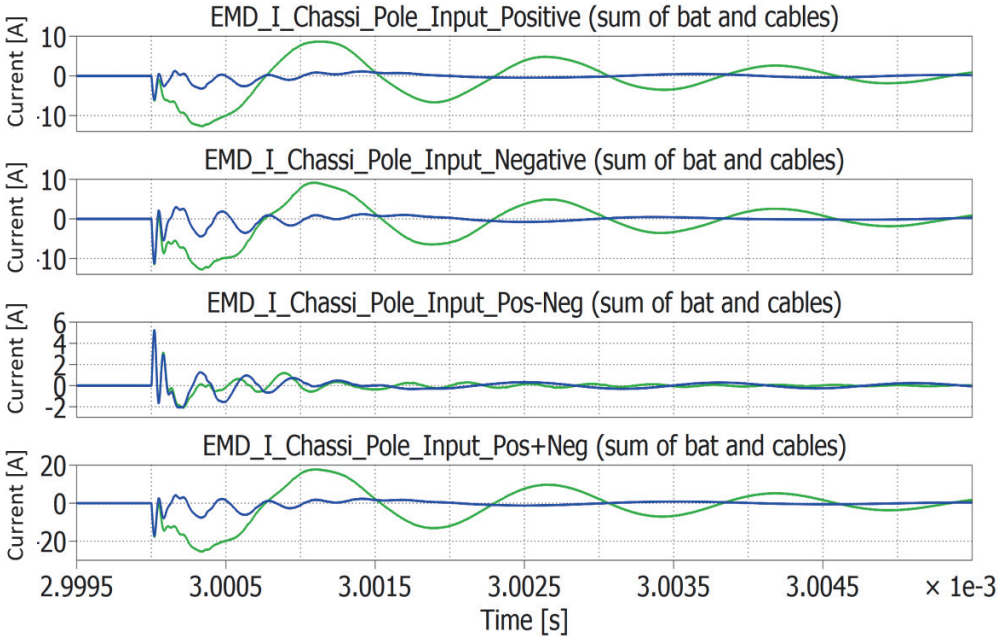

Figure 4.8: Comparison between inbound CM current to the EMD for two different CM-capacitance values in the EMD. Green graph is for $X_1 = 6.9$ and blue for $X_2 = 37$.

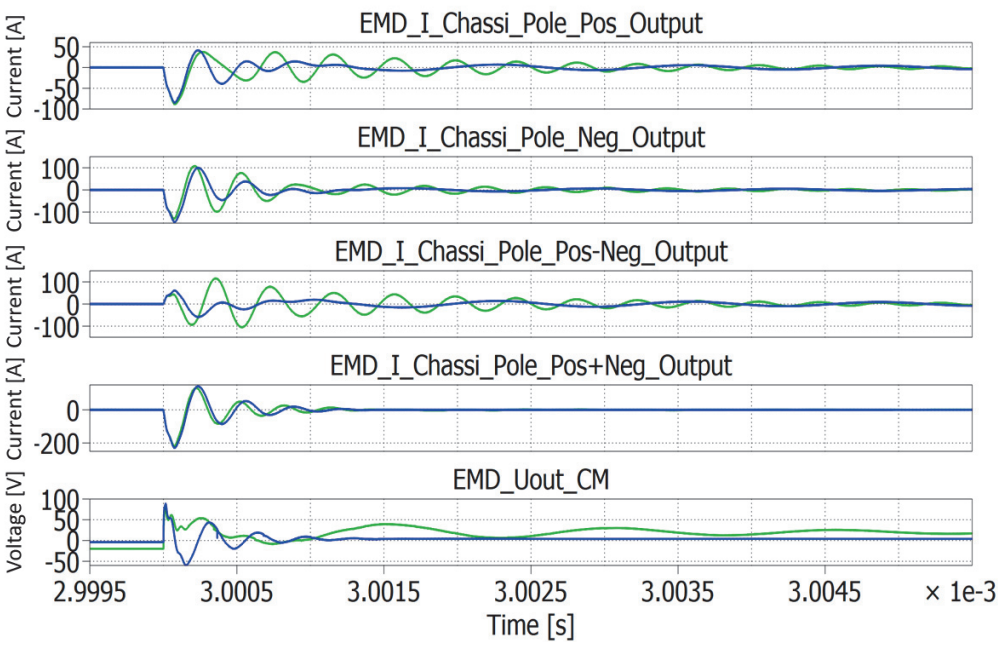

Figure 4.9: Comparison between outbound CM current from the EMD for two different CM-capacitance values in the EMD. Green graph is for $X_1 = 6.9$ and blue for $X_2 = 37$.

4.2 Conclusions from the system simulation

The simulations shows that the theory described in subsection 2.4.4 is validated.
The introduced factor X shows the importance of the ratio between CM capacitors and the asymmetrical parasitic capacitance. This chapter also shows the importance of where the CM capacitances are located to avoid CM currents in the vehicle.

Chapter 5

Vehicle measurement system

The purpose of the vehicle measurement system is to perform simultaneous measurements of several electric quantities on many nodes of the TVS a large commercial vehicle in real-time. In order to do so, around 100 measurement points are needed which are physically distributed over up to 30 m along the vehicle. In a laboratory setup, frequencies for the common mode current has previously been observed up to 7 MHz. The characteristics of the disturbances are different at different speeds and traction powers and to somewhat capture that a complete acceleration and retardation shall be recorded. The measurement system can perform one single measurement up to 5 minutes and the can store measurements, on the hard drive, up to 1 hour. This sets the requirements on the measurement system, from the sensors to the data acquisition system. The requirements on measurements system is set for the worst case which is a articulated bus. Worst case, at this time, in terms of number of measurement point and physical distribution. That is the cause for showing a bus in this chapter.

To get a sense of the physical distribution of the nodes, a bus is shown in figure 5.1. Note that most of the TVS and its subsystems are distributed along the roof and in the rear end of the bus.

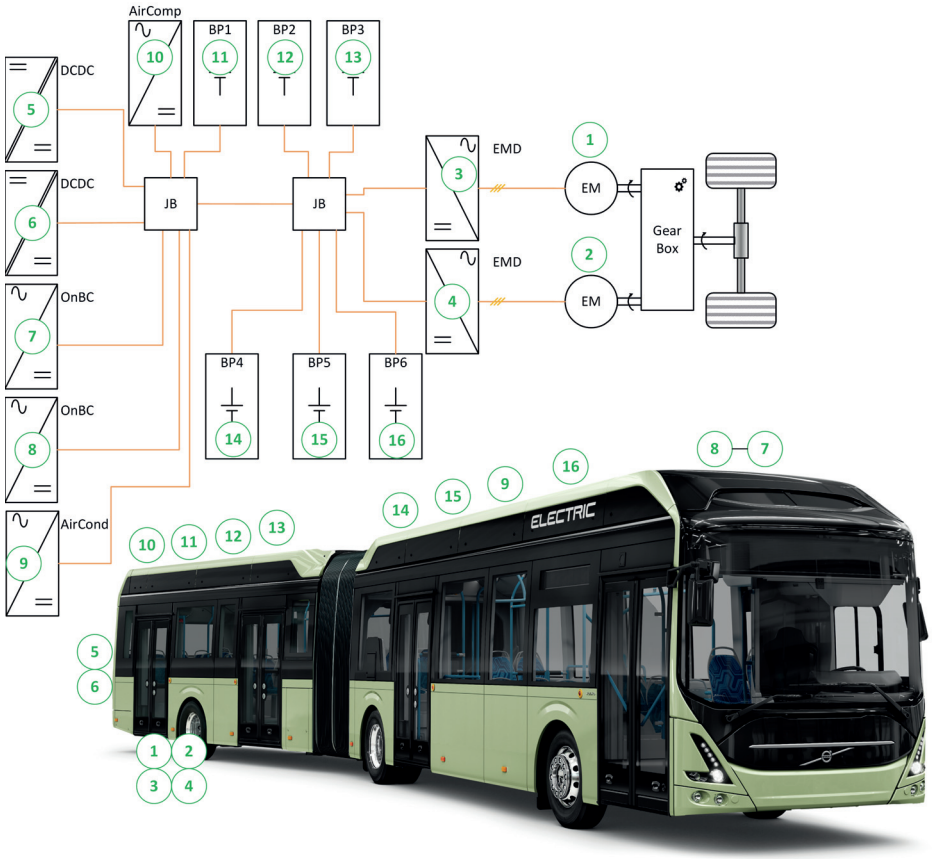

Figure 5.1: Distributed TVS on an articulated bus. This vehicle is around 24m in length.

The goal of the measurement system ability is to measure all required TVS quantities, DM and CM currents, DM and CM voltage) simultaneously on a large commercial vehicle with 20 TVS nodes. These requirements imply:

- Frequency band DC - 30 MHz (which implies a sampling rate of 60 MSamples/sec).
- Physically distributed sensors. Up to 30 meters in a bi-articulated bus.
- 100 channels. 20 nodes x (2DC potential [(1)] + 1 DC current + 1 DM current + 1 DC current)
- Compensation for signal delay in the cables.
- Easy and safe connection of measurement sensors.
- Low frequency and DC current measurement [I_{DC}]. (This quantity is not handled in this thesis.)

- High frequency Common Mode current measurement [I_{cm}].
- High frequency Differential Mode current measurement [I_{dm}].
- High frequency Common Mode voltage measurement (1) [U_{cm}].
- High frequency Differential Mode voltage measurement (2) [U_{dm}].
- CAN signals to be recorded and to be presented as analogue signals.
- Data analysis of all signals.
- Long measurement time for driving cycles, total recording time 1 hour.
- Operation shall be as with an oscilloscope with live view, trigger, scaling, zoom and so on.
- Weatherproof for outdoor use.

(1) According to equation 2.1 the common mode voltage cannot be measured. It is obtained by measuring the positive and negative potential to ground/chassis.
(2) To save sensors this quantity can be as $u_{dm}=u_{pos}-u_{neg}$.

At the time of starting the development of the measurement system, no oscilloscope or measurement system available on the market fulfilled the requirements. Therefore, development of a measurement system was necessary. Hardware from National Instrument (NI) was chosen as base for the development.

In the evaluation of possible solutions there are some of the requirements above that was not fulfilled.

- BW DC - 30 MHz (60 MSamples/sec). For DM mode the requirement is not fulfilled due to that the DM current is measured with the sensor formed like an ”8”, according to the later shown figure 5.3 and equation 5.2, which for the Rogowski current sensor reduces the BW. However, the higher BW is not that important for DM but for CM. The lower frequencies of the DM current is measured with a low frequency and DC current sensor. Deviation from requirement is OK.
- Operation shall be as with an oscilloscope with live view, trigger, scaling, zoom and so on. Looking at all traces in real-time is not possible due to hardware performance of the system. A deviation that causes negative impact of handling the measurement system.
- Weatherproof for outdoor use. Neither the NI system or the sensors are weatherproof and a decision to perform all the tests in a vehicle DYNO, rolling road, was taken. It is better to perform the test in DYNO since this increases the repeatability of the tests.

5.1 Measurement system overview

The measurement system is primarily to be used on vehicles but also in laboratory rigs. The vehicle to be measured is shown in figure 2.1. This vehicle is equipped with Break Out Boxes, that hosts the sensors, and the NI oscilloscope, see figure 5.2. The connection of sensors in the BoB to the NI oscilloscope are not shown.

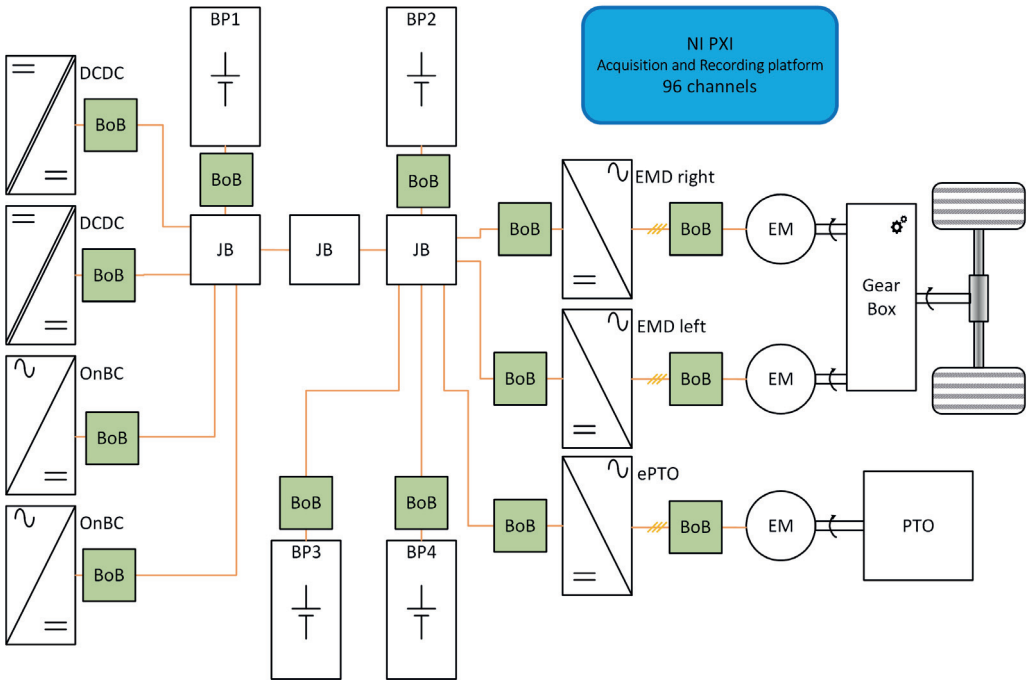

Figure 5.2: Volvo truck FE280 with Break Out Boxes and NI Oscilloscope.

5.2 Break out Boxes

The purpose with a break out box (BoB) is to break the circuit and insert a box with sensors between the supply and device under test (DUT) in a way that is feasible for the vehicle, affect the measurement as little as possible as well as secure personal safety.
The demands on the BoB is to measure the DC current, common mode and differential mode current as well as the voltage from pole to chassis and pole to pole. In laboratory setup, the frequencies for the common mode current are seen up to 7MHz. The target is to measure up to 30MHz for all quantities. In figure 5.3 the schematics of the BoB is shown. Each quantity and sensor is further described in the following subsections for each sensor.

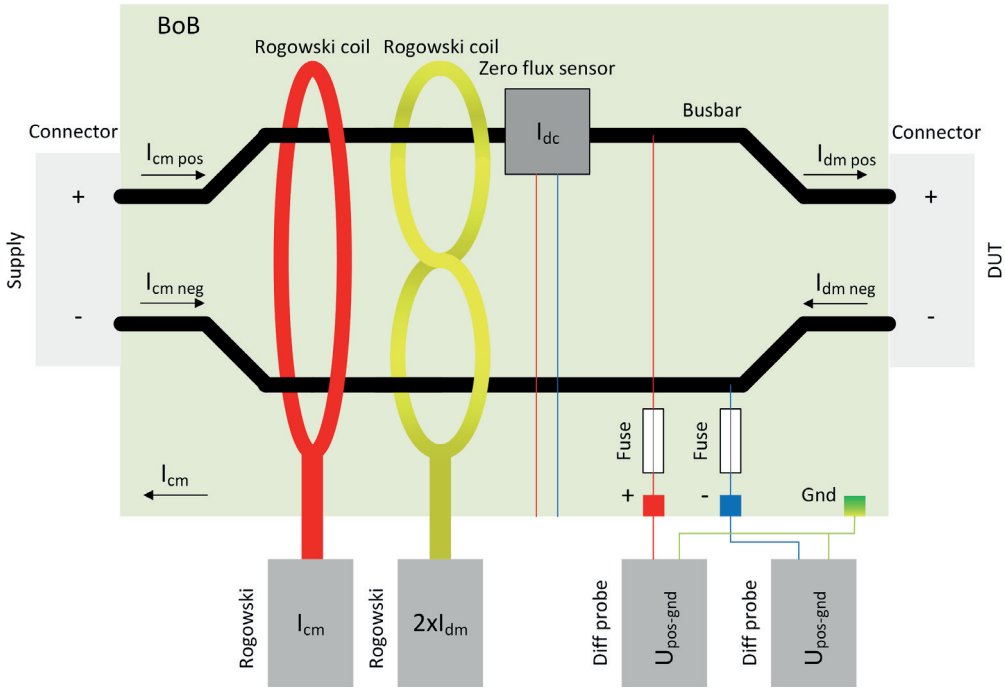

Figure 5.3: BoB with sensors for I_{cm}, I_{dm} and I_{dc} as well as fused outlets for voltage measurements.

5.2.1 CM Current Sensor Rogowski Coil

The common mode current is the current that flows in the ground plane. In the conductors it is divided between positive and negative but does not have to be evenly distributed between these. The common mode current is measured as:

$$I_{cm} = I_{cm\ pos} + I_{cm\ neg} \tag{5.1}$$

In practice, the current is measured with the Rogowski coil around both conductors, see the red coil in figure 5.3. The chosen Rogowski coil CWTHF 015x/B/2.5/300 is supplied from PEMUK. For the CM current measured between the EMD and the EM a Rogowski coil with higher current rating is chosen.

- BW (-3dB) 300Hz to 30MHz
- Traceable accuracy to ±0.2% and with conductor central in the loop
- Variation to position in the coil loop ±1%
- Sensitivity 200mV/A
- Coil length 300mm

- 10kV insulation
- 8.5mm thickness

Figure 5.4: PEMUK CWT Rogowski coil. Picture from PEMUK

5.2.2 DM Current Sensor Rogowski Coil

The differential mode current is the current that flows in the positive conductor and returns in the negative. In reality the differential mode current, if measured in one conductor, will contain the common mode current as well. To reduce the effect of common mode current the differential current is measured in both conductors as:

$$I_{dm} = \frac{I_{dm\ pos} + I_{dm\ neg}}{2} \tag{5.2}$$

This will eliminate the common mode current if it is equal in both conductors. This is however not true at all times.

In practical, the differential mode current is measured with the Rogowski coil formed like an eight around both conductors, see the yellow coil in figure 5.3.

The chosen Rogowski coil CWTMiniHF 03/B/2.5/400/5 is supplied from PEMUK. For the DM current measured between the EMD and the EM a Rogowski coil with higher current rating is chosen.

- BW (-3dB) 100Hz to 12MHz
- Traceable accuracy to ±2% and with conductor central in the loop
- Sensitivity 100mV/A
- Coil length 400mm
- 5kV insulation
- 4.5mm thickness

5.2.3 Differential Voltage Probe

The voltage is measured with a differential voltage probe. Apart from the BW requirements the probe shall be connected to the oscilloscope with a BNC connector. The chosen sensor is a TT-SI 9010 from TESTEC. Some key ratings according to [24]:

- BW (-3dB) DC to 70MHz
- Attenuation x100/x1000
- Accuracy ±2%
- Input impedance 10MΩ, 10 pF
- Input Voltage Differential Mode x100 ±700V (DC + peak AC) or 700 V_{rms}
- Input Voltage Differential Mode x1000 ±7000V (DC + peak AC) or 2500 V_{rms}

Figure 5.5: Testec TT-SI-9010 differential voltage probe.

5.3 NI Oscilloscope-Acquisition and Recording platform PXI

The measurement signals from all the BoBs needs to be collected and sampled in a synchronous way. For this purpose a signal sampling system is needed, like a 100-channel oscilloscope. For that purpose, the modular instrumentation platform PCI eXtensions for Instrumentation (PXI) is selected. It is a rugged platform that offers high-performance

measurement and control capabilities. Integrated timing and triggering features in the PXI back plane provide precise inter-module synchronization. The developed oscilloscope measurement system can be used with up to 96 channels at a sampling rate at 60MS/s with 4 PXI chassis connected according to figure 5.6

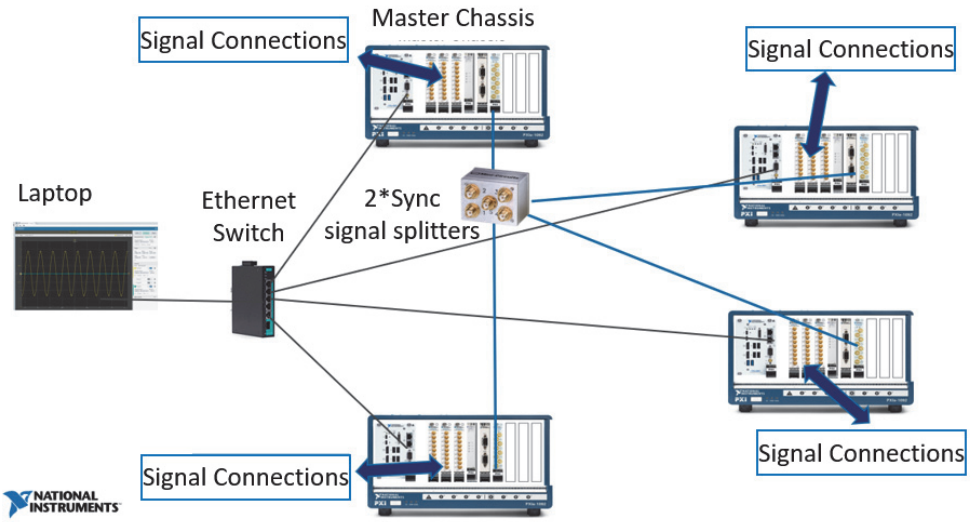

Figure 5.6: PXI solution architecture with 4 PXI, signal synchronization switch, Ethernet hub and laptop.

5.3.1 PXI chassis and included modules

The PXI chassis (PXIe 1092) in figure 5.7 contains the following parts from the left:

- PXI controller (PXIe-8861)
- 4 oscilloscope modules with 8 channels each (PXIe-5105). 12 bits of resolution synchronized using the same sampling clock at a max of 60 MS/s/ch*.
- Timing module (PXIe-6674T). Analog channels are inter-module synchronized within each chassis as well as to an external master clock in order to enable multi-chassis recording
- 4TB SSD disk (PXIe-8267)
- 6 Channel X-NET board (PXI-8510) equipped with 5 pc CAN adapters (TRC-8542)
- Adapter plate for the CAN adapters.

*Each module is streaming data to the PXI back-plane using a dedicated PCIe x4 Gen1 lane (1 GB/s in theory). In practice that bandwidth is less than 1GB/s and that limits the

continuous streaming module bandwidth to cope with only 6 channels running in full speed. That is why 4 analog input modules are used.

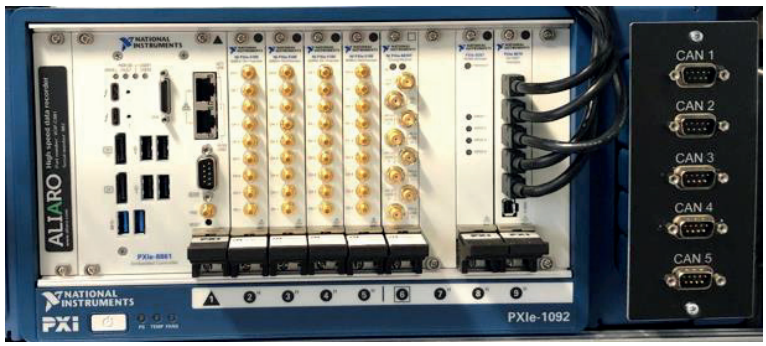

Figure 5.7: PXI back-plane with mounted modules.

5.3.2 Streaming rate

The key goal of the streaming architecture it to transmit data from an instrument fast enough to maintain a continuous generation or acquisition. When performing an acquisition task, the data produced by the instrument is transmitted through the PCIe bus to the host computer to place into memory. The required bandwidth is 30MHz which means a sampling frequency of in >60 MSamples every second. A 12-bit sample is stored on disk as 2 bytes. This implies s data stream at maximum >120 MB/s per channel. With 24 channels running in full speed a total data rate of 2.9 GB/s is required. The chassis used PXIe-1092 has a total bandwidth of 24 GB/s.

In order to store continuous data a fast storage device with required disk size of 4 TB is used. The PXIe-8267 can record in 5 GB/s for a total of 4 TB. If maximum sampling rate is used on all 24 channels, 22 minutes of recording can be performed. The sensors for DC require much slower sampling which implies that some channels can record on lower sampling rate.

5.3.3 Synchronization and system architecture

With PXI timing and synchronization modules advanced multi-device synchronization by using the trigger bus, star trigger, and system reference clock features of PXI can be implemented, see figure 5.8. With an NI PXI signal-based timing and synchronization architecture, clocks and triggers are physically connected between subsystems which then synchronize the sample clocks of individual modules. This generates the highest precision of synchronization and is required in this case to reach below 1 ns of synchronization between sample, see figure 5.9. With the timing and synchronization capabilities built in to the PXI platform, you can distribute a 10 MHz and/or 100 MHz system reference clock on

the back-plane to achieve synchronization across modules within a PXI chassis. Likewise, you can distribute the 10 MHz reference clock between chassis back-planes to synchronize modules in multiple PXI chassis, see figure 5.10.

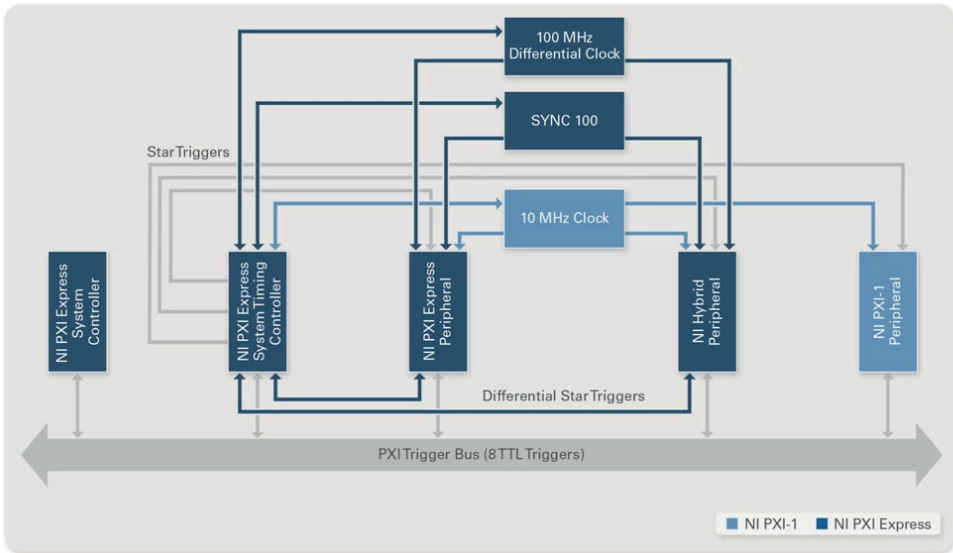

Figure 5.8: PXI timing and synchronization modules

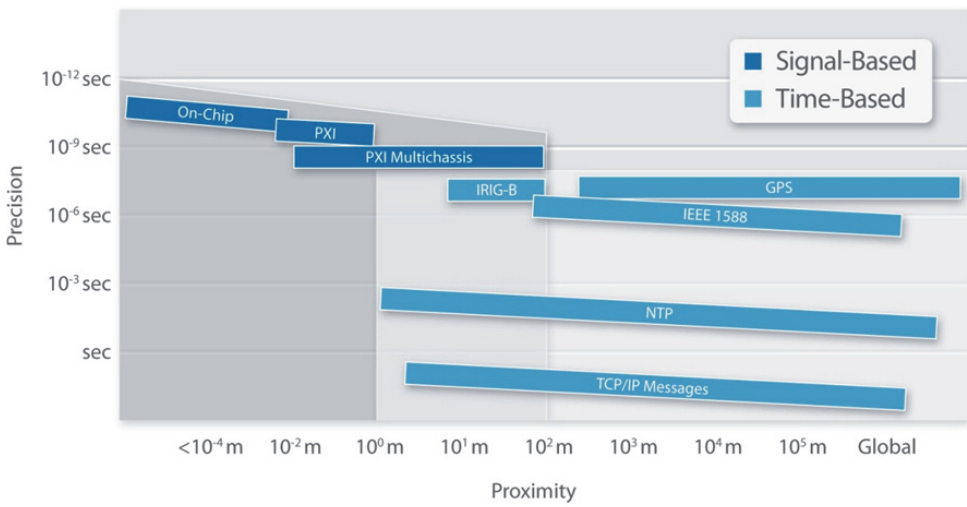

Figure 5.9: PXI precision vs. proximity for signal-based and time based synchronization.

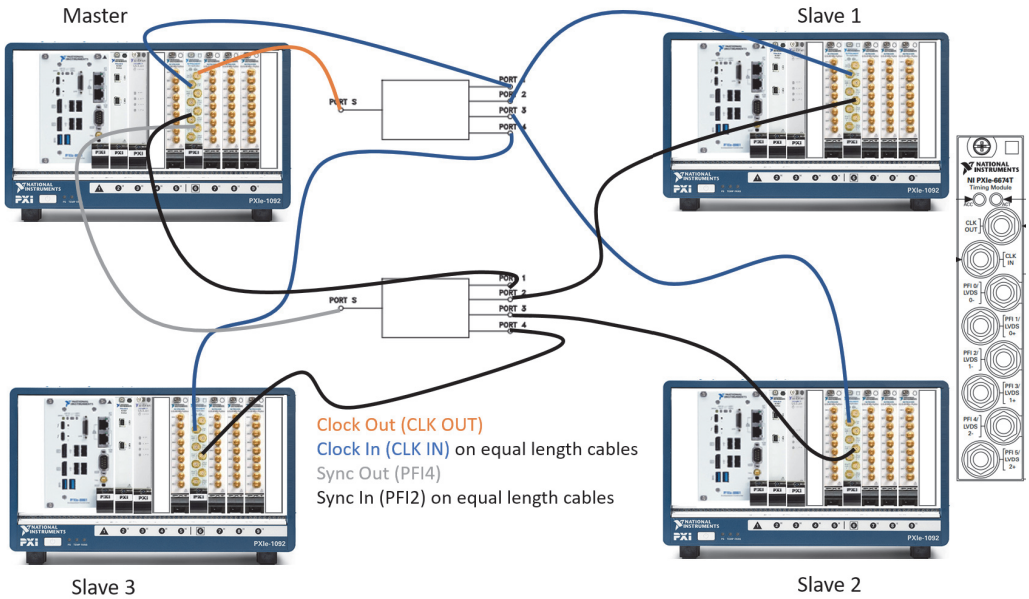

Figure 5.10: Synchronization of multiple PXI. The PXI can be used standalone, 2 PXI, 3 PXI or 4 PXI.

5.3.4 Accuracy

The differential voltage probes and Rogowski coils are all connected to the oscilloscope at 1MΩinput impedance. In table 5.1 the accuracy for the DC measurements is listed and in table 5.2 the accuracy for the AC measurements is listed. The tables origin from [9].

Table 5.1: Accuracy for DC measurements

Input Impedance	Input Range ($V_{pk\text{-}pk}$)	DC Accuracy, Warranted
50 Ω	All	±(1% × *Reading* + 0.25% of FS + 600 µV)
1 MΩ	0.05 V	±(1% × *Reading* + 0.25% of FS + 600 µV)
	0.2 V, 1 V, and 6 V	±(0.65% × *Reading* + 0.25% of FS + 600 µV)
	30 V	±(0.75% × *Reading* + 0.25% of FS + 600 µV)

Table 5.2: Accuracy for AC measurements.

Input Impedance	Input Range (V_{pk-pk})	AC Amplitude Accuracy
50 Ω	All	±0.1 dB (±1.2%) of *Reading*
1 MΩ	0.05 V	±0.2 dB (±2.3%) of *Reading*
	0.2 V and 1 V	±0.13 dB (±1.5%) of *Reading*
	6 V and 30 V	±0.4 dB (±4.7%) of *Reading*

In practice the accuracy for AC measurements, will be according to table 5.2 last row, ±4.7% of reading.

5.3.5 Bandwidth BW

The corner frequency) is defined as the frequency when the input signal is attenuated to -3dB or 70.7 percent of the original amplitude. This will normally occur at a lower frequency (f_1) and the upper frequency (f_2).

$$-3dB = 20log\frac{V_{out}}{V_{in}}. \tag{5.3}$$

The center frequency is defined as:

$$f_0 = \sqrt{f_1 f_2}. \tag{5.4}$$

Finally, the bandwidth is defined as:

$$BW = f_2 - f_1. \tag{5.5}$$

5.3.6 Nyquist Sampling Theorem

The Nyquist sampling theorem explains and states the relationship between the sampling frequency and the frequency of the signal. This signal is referred to as the Nyquist frequency f_N :

$$f_s > 2 * f_N \tag{5.6}$$

The following figure 5.11 is found in [8].

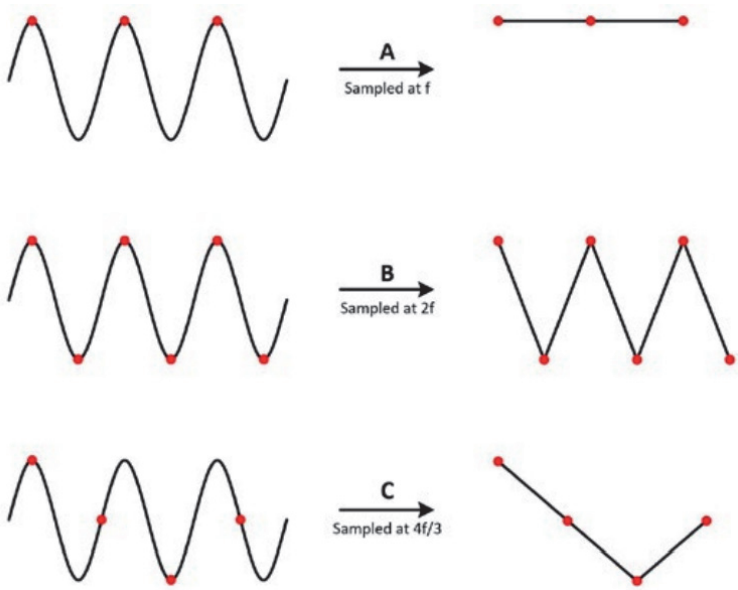

Figure 5.11: Too low sample rate can cause an incorrect waveform. Figure from [8]

This subsection is just a teaser or repetition of the subject. It is not meant to be exhaustive.

5.3.7 Anti-aliasing filter

The NI oscilloscope offers an anti-aliasing filter at 24MHz. It can be set either on or off. As shown in 5.3.6 a too low sampling frequency can cause an incorrect waveform. If the measured signal is sampled at a frequency lower than twice the Nyquist frequency, false lower frequencies can appear in the sampled data. This phenomenon is called aliasing. An example of this is shown in figure 5.12.

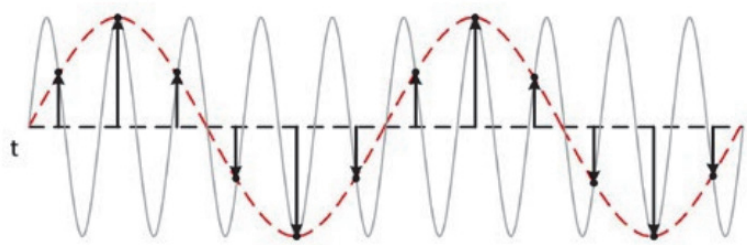

Figure 5.12: Aliasing caused by too low sample rate. Figure from [8]

In practice, it leads to that the anti-aliasing filter is needed for sampling frequencies f_s <48MHz which is 60MSamples/s on the PXI.

The next lower sampling rate that can be used is 30MSamples/s. This requires an anti-aliasing filter of 15MHz which is not available on the PXI. Another possible way to reduce the f_s is if the BW of the sensor is reduced.

If the anti-aliasing filter is not used there is a risk of aliasing. The alias frequency can, according to [8], be calculated as:

$$f_a = |n * f_s - f| \tag{5.7}$$

n closest integer multiple of the sample frequency

A few examples is shown in figure 5.13

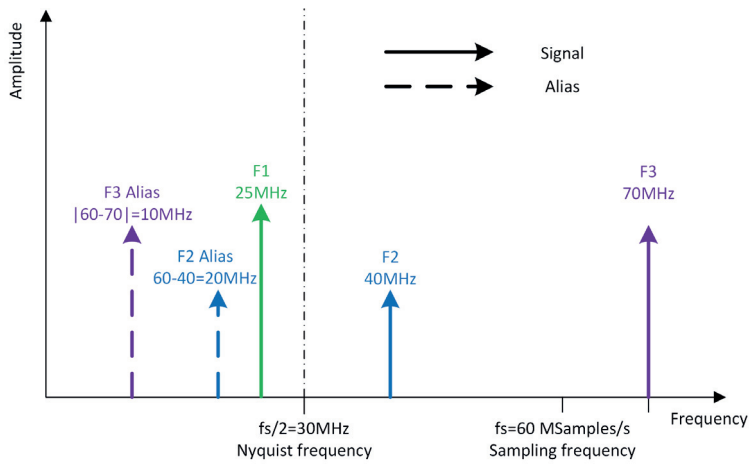

Figure 5.13: Alias frequencies

The same applies here as for the previous chapter that this subsection is just a teaser or repetition of the subject. It is not meant to be exhaustive.

5.3.8 Anti-aliasing filter in measurements

According to 5.2.2, 5.2.1 and 5.2.3 the BW for the sensors is:

- BW (-3dB) 300Hz to 30MHz for CM current sensor.
- BW (-3dB) 100Hz to 12MHz for DM current sensor.
- BW DC to 70MHz for differential voltage sensor.

This leads to that the lowest possible f_s is:

- 60MSamples/s for the CM current.

- 30MSamples/s (e.g., 2*12MHz) for the DM current.
- 60MSamples/s for the for the differential voltage.

A small loss can be obtained for the CM current above 24MHz. But using the anti-aliasing filter at all times will reduce the risk of aliasing.

5.3.9 Resolution

The 8 channels oscilloscope modules (PXIe-5105) have 12 bit of resolution, 2^{12} or 4096 levels of the measured signal. Assume that an input channel is set to the range of 30V. The resolution of the measured signal is thus 30/4096 or 7.3mV. Assume a measurement scenario with a voltmeter x100 attenuation is used. The test object delivers a voltage of 50-700V. This result in a signal to the oscilloscope of 0.5-7V. The possible input ranges are 30V, 6V, 1V, 0.2V and 0.05V. And the input divided on ±range, e.g. for 30V range the available measurement is ±15V. This is the range that can be used. This equals to a ±1500V range on the sensor (in this example the differential voltage probe), the lower range 6V is to narrow as it will be ±300V. The resolution of the 30V range is 3000V/4096 or 0.73V. A little rough but necessary to know. The noise in this range is digital noise.

5.4 Post Processing

Post processing of the huge amount of data that is collected with the measurement system is a challenge. Each oscilloscope card in the PXI saves the data to the internal 4 GB SSD disc. The file size is always the same which implies that the length of the file differs depending on the number of channels recorded and the sampling rate. When the data has reached the set size a new consecutive file is created. An illustration of a few channels is shown in figure 5.14.

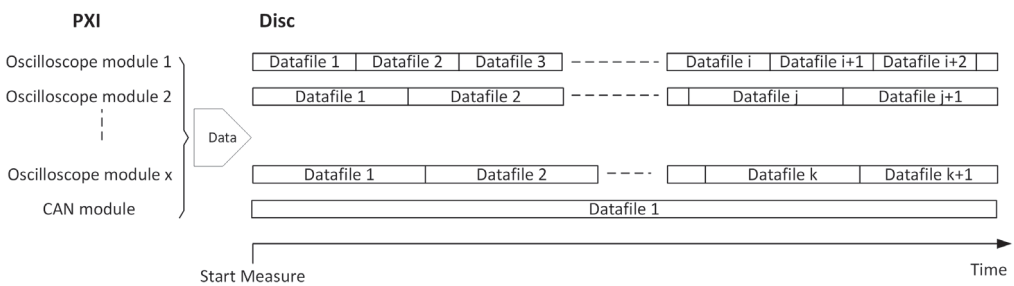

Figure 5.14: Data files stored at disc. For high sampled channels, many consecutive files are created and for a low sampled channel it might be only one datafile.

Assume that a specific time interval is of interest, see figure 5.15.

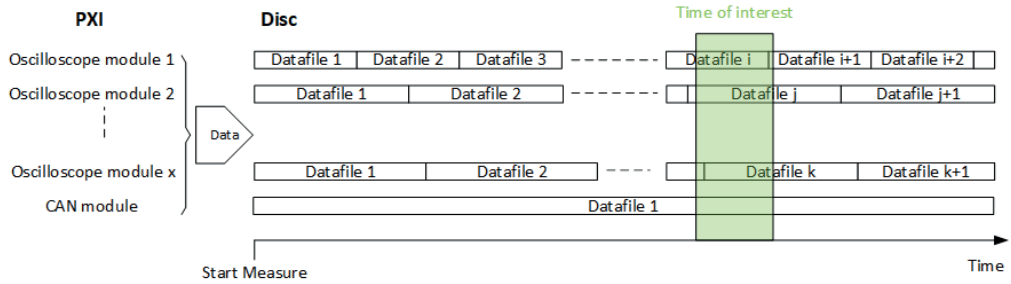

Figure 5.15: Specific time interval of interest for analyze

It is impossible to open correlating files to view the in a synchronized manner.

A post processing tool is developed that index all the files. Each channel is treated as one file. See figure 5.16

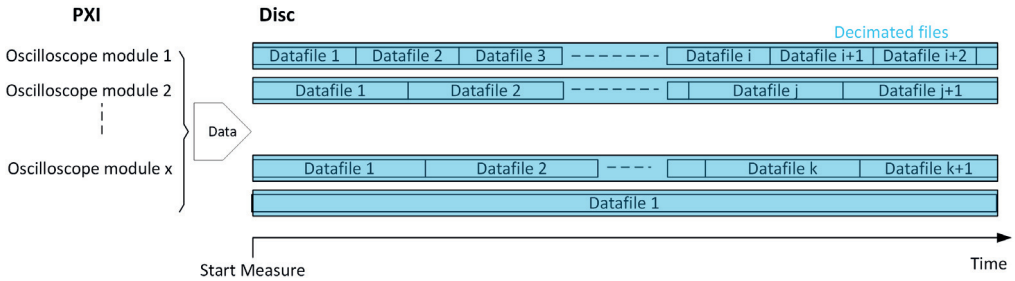

Figure 5.16: Indexed file

Each channel of interest can be evaluated and when a interesting phenomenon is found all channels or specified channels can be exported to a new file, containing the specific time interval and ALL channels. See figure 5.17

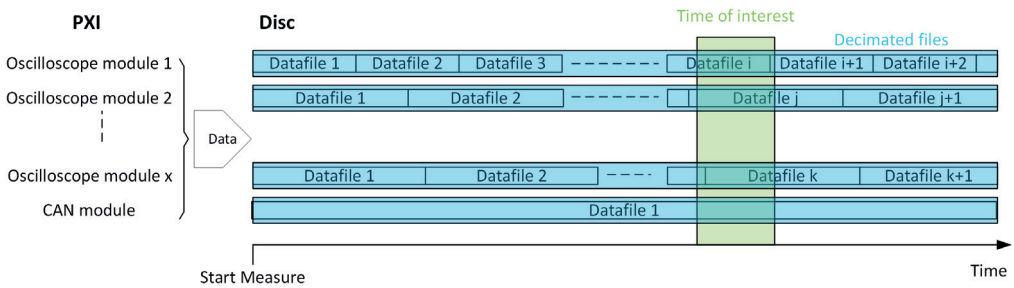

Figure 5.17: New file, created from the indexed file, containing all channels

This file can be evaluated in for example DIADEM. DIADEM is a data analyzing software from National Instrument that can analyze data and create reports.

If a full measurement system is used with 4 PXI chassis and CAN boards each PXI can create 5 parallel files and in total 20 parallel files for 4 PXIs. To illustrate the challenge a long measurement of 600 seconds for one channel is shown in figure 5.18. The complete data in this view is 72 consecutive files. For all files measured it is 72 files per board x 5boards/PXI x 4 PXI = 1440 files. The data in the view is decimated as the 60MS/sec cannot be obtained anyway. In the middle of the measurement an interesting phenomena is found. The post processing tool can now export just this time span with all measured channels or a few selected channels to a new file that is synchronized between channels with full resolution. From the 144 data files the post processing tool can create one data file with the channels and time span of interest.

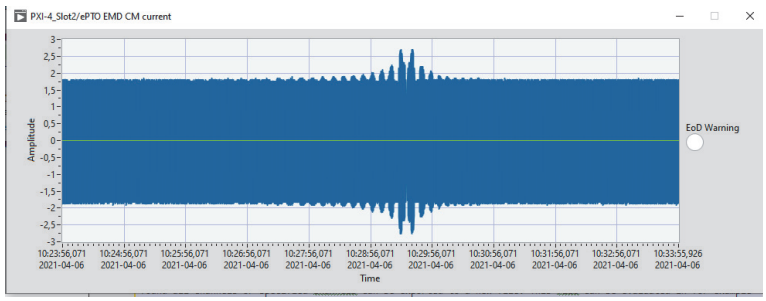

Figure 5.18: One channel measured for 600seconds. The measurement is divided into 72 chopped files which the post processing tool has indexed and can show in a decimated format.

5.4.1 Total accuracy for HF (Common Mode)

According to 5.3.4 the AC accuracy for the oscilloscope is 4.7% at 50kHz. No note from NI states what can be treated as DC or AC.
According to subsections 5.2.1, 5.2.2 and 5.2.3 the accuracy for the sensors are 1%, 2% and 2% respectively.
The total accuracy for HF for oscilloscope and sensor will then be the product of the accuracy.

I_{cm} 1.047*1.01=±5.7%

I_{dm} 1.047*1.02=±6.8%

U_{cm} 1.047*1.02=±6.8%

The accuracy may seem poor at first glance but the phenomenon with common mode EMI is more of an understanding than a exact verification. Requirements hardly do not exist for the conductive EMI. However, CM currents generates radiated EMI where legal requirements and requirements from standards have to be fulfilled. The important is to understand how EMI reacts on changes of the system and filters. If changing one parameter, e.g. filter or vehicle layout, in the system - what effect will it result in for the CM currents?

This shall be seen in simulations as well. The relative difference is more important than if the accuracy is 1% or 7%.

5.4.2 Measured parameters from direct measuring or post-processing.

Some of the quantities of interest in this thesis are directly measured by the system described in this chapter, some a indirectly calculated from the measured quantities. The quantities to measure or calculate are:

U_{cm} Common Mode Voltage, calculated by post processing as in equation 5.8.

I_{cm} Common Mode Current, measured as the difference in equation 5.9.

I_{dm} Differential Mode Current, measured as the sum in equation 5.10.

u_{dm} Differential Mode Voltage, measured directly.

$$U_{cm} = \frac{U_{pos} + U_{neg}}{2}. \tag{5.8}$$

$$I_{cm} = I_{pos} - I_{neg} \tag{5.9}$$

$$I_{dm} = \frac{I_{pos} + I_{neg}}{2} \tag{5.10}$$

Chapter 6

Common Mode Measurements on a truck

In this chapter CM mode measurements on a FE280 truck are presented. In the previous chapter 5, the measurement system was developed with a bus in mind. However, the objective is also including the truck. But since the bus has a wider physical distribution of nodes, the truck can be seen as a bus of less complexity. To achieve differential mode measurements i.e., to make the vehicle draw power to the wheels, it is required that the truck is running on a rolling road, called DYNO, where speed and load can be varied. A DYNO has not been available in the time frame for the thesis. Thus, only CM measurements on a truck standing still are presented here. The truck measured has been described earlier in chapter 2 and the measurement system in chapter 5. Common mode current is a source for disturbances in the vehicle but also outside the vehicle by radiated or conductive coupled disturbances. If disturbances are found after a vehicle is designed and the first prototype is produced it can be complicated and expensive to deal with the root cause. The importance of understanding the disturbances and a correct design cannot be underestimated. The measurements shown in this chapter are comparative measurements to show that the theory from chapter 2 and in particular section 2.4 is valid.

6.1 Results from CMDC voltage measurements on a truck

The simulation model theory [25], described in section 4.1 is compared to measurements in a truck. The system level schematic is shown in figure 6.1.

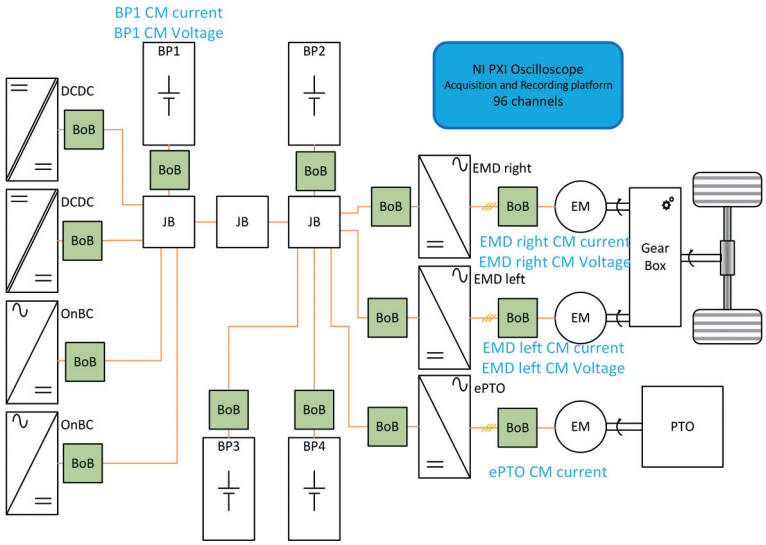

Figure 6.1: Measured parameters are shown in the schematic for the Volvo FE280 truck with converters (DCDC, EMD, ePTO EMD), chargers (OnBC), batteries, junction boxes (JB) and Break Out Boxes (BoB).

The measurements performed are made on a truck standing still with no torque on the traction machines and thus a zero voltage output to the EM, described in subsection 2.4.3.

The common mode measurements in this section shows:

- The CMDC voltage compared to theory and simulations with variation of the factor X, see subsection 6.1.1.
- The CMDC voltage and current elimination at simultaneous 180° phase shifted switching of the modulation of the two EMD's, subsection 6.1.2.
- Measured CM current maximum due to simultaneous switching in phase, subsection 6.1.3.

The following four figures shows the possible combinations of the zero voltage that can happen when switching with two converters. The switch state in:

- both converters are (0,0,0), see figure 6.2
- the top converter is (0,0,0) and the lower converter (1,1,1), see figure 6.3
- the top converter is (1,1,1) and the lower converter (0,0,0), see figure 6.4
- both converters are (1,1,1), see figure 6.5

In subsection 6.1.1 the converters are phase shifted and the switching pattern is:
(top converter) (lower converter)
(0,0,0)(0,0,0), (1,1,1)(0,0,0), (1,1,1)(1,1,1), (0,0,0)(1,1,1), ...

In subsection 6.1.2 the converters are phase shifted 180°, and the switching pattern is:
(top converter) (lower converter)
(0,0,0)(1,1,1), (1,1,1)(0,0,0), ...

In subsection 6.1.3 the converters are in phase (0°), and the switching pattern is:
(top converter) (lower converter)
(0,0,0)(0,0,0), (1,1,1)(1,1,1), ...

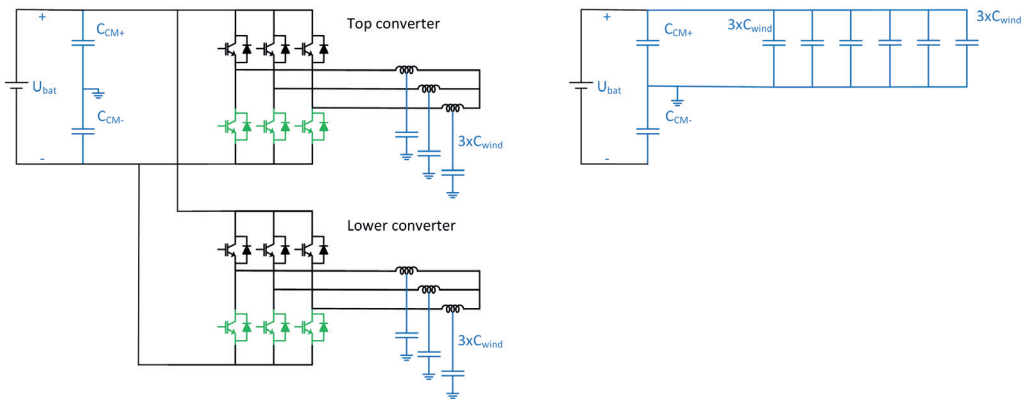

Figure 6.2: The switch state in both converters are (0,0,0)

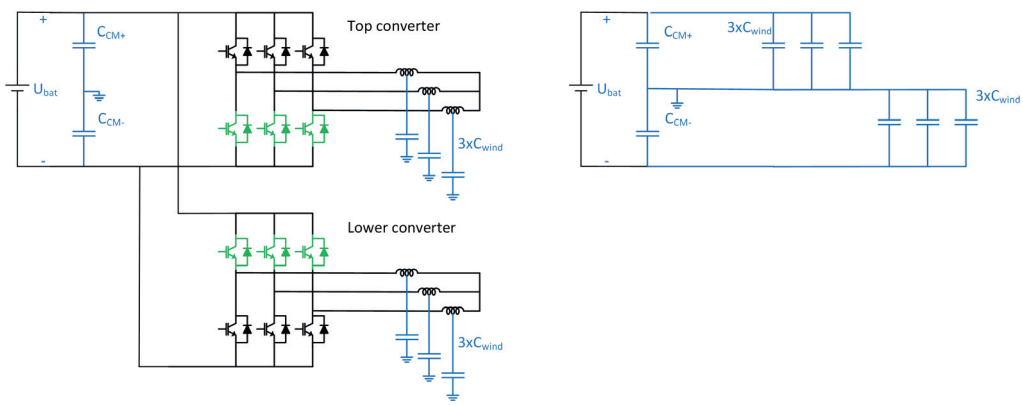

Figure 6.3: The switch state in the top converter is (0,0,0) and the lower (1,1,1)

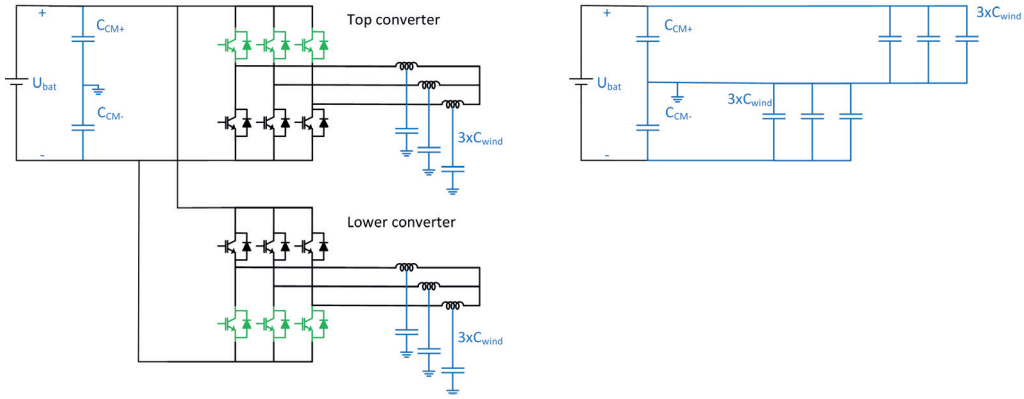

Figure 6.4: The switch state in the top converter is (1,1,1) and the lower (0,0,0)

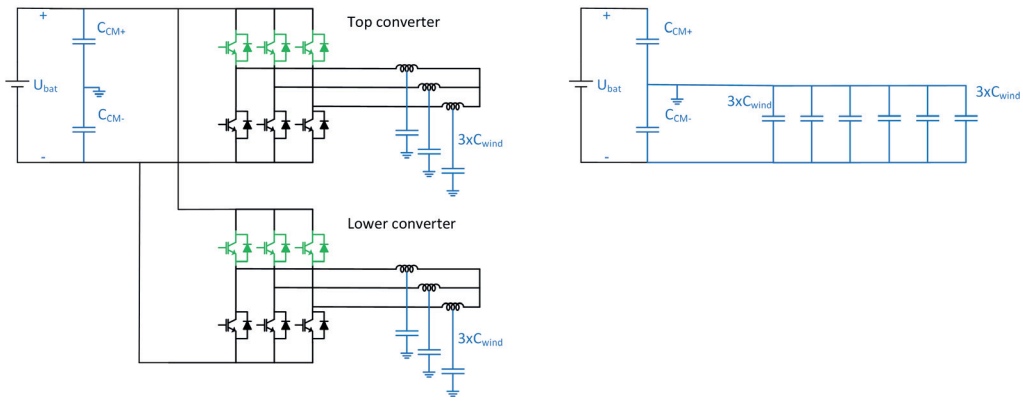

Figure 6.5: The switch state in both converters are (1,1,1)

6.1.1 CMDC voltage compared to theory and simulations with varied factor X.

To verify the statement in equation 2.17 the CMDC voltage that appears in the system shown in figure 2.1 is measured with two different X values. The added capacitance, to change the factor X, is added in the BoB between the EM and EMD for both the left and right EMD. NB! The simulated system in the beginning of this thesis is made on a reduced system model whereas the measurements are made on a full electric truck. That is why the X values of the measured system (X_3 & X_4) are different from the X values of the simulated system (X_1 & X_2). The battery voltage is 650V and $X_3 = 11.5$ and $X_4 = 31.1$. The corresponding CMDC voltage according is:

$$u_{CMDC} = \frac{U_{bat}}{2 * X_3 + 1} = \frac{650}{2 * 11.5 + 1} = 27V \tag{6.1}$$

$$u_{CMDC} = \frac{U_{bat}}{2 * X_4 + 1} = \frac{650}{2 * 31.1 + 1} = 10.3V \tag{6.2}$$

The corresponding measured CMDC voltage $u_{CMDC} = 30.4V$ and $u_{CMDC} = 11.9V$, shown in the top graphs *BP1 CM voltage* in figure 6.6 and 6.7 respectively. The difference between the CMDC voltage from measurements and by formula is within 10%. As the model is complex and contributing parasitics affects the values, a difference between measurement and calculation is acceptable. The importance is the understanding of the affecting parameters. There is one difference in the behavior comparing the graphs in figure 4.5 with figure 6.6 and 6.7 which is that in figure 4.5 there is only one motor drive switching and in the later graphs there are two motor drives that are not switching on the exact same frequency, nor have the exact same phase of the modulation carrier wave. They both have their own control and even though the switching frequency is the "same", the switching frequency can differ just a little. That results in that the switching compared to each other will drift. This results in that the CM capacitances of the traction machines C_{asym} occasionally are connected to the same pole of the TVS and occasionally to different poles of the TVS. In the latter case the asymmetries of the two different C_{asym} evens out. The wave form becomes here quasi square waved as described in subsection 4.1.

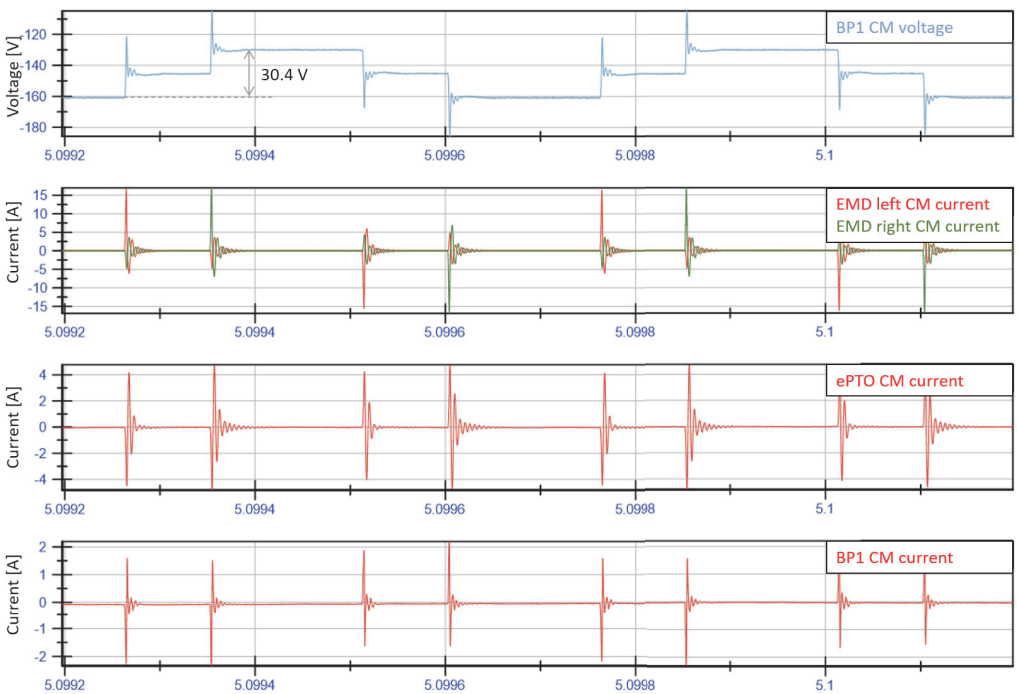

Figure 6.6: Original configuration with $X_3 = 11.5$

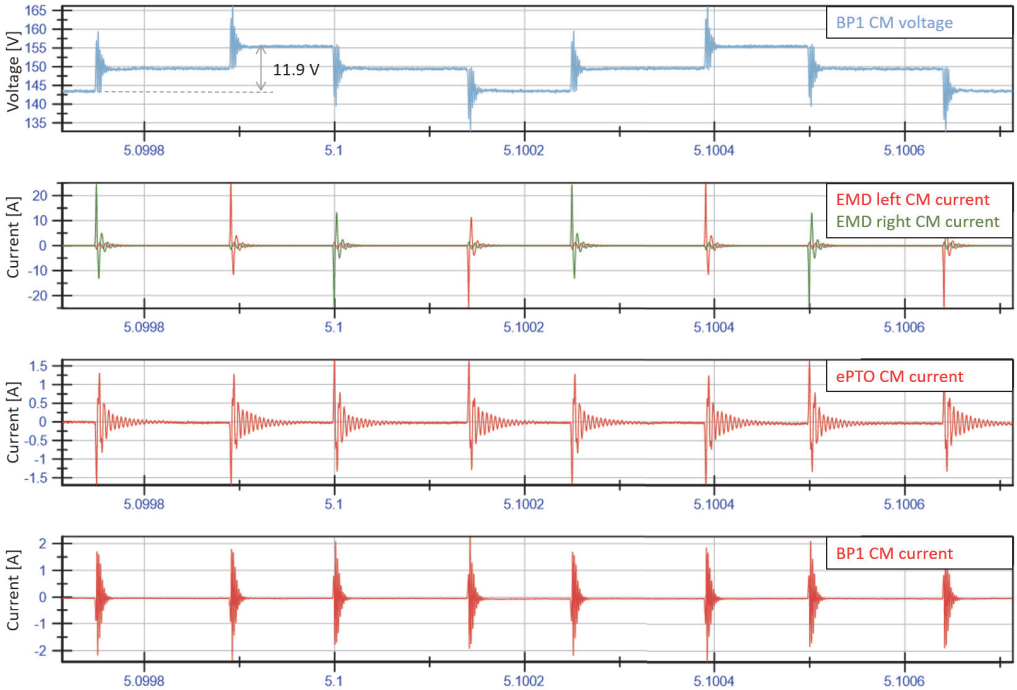

Figure 6.7: Configuration with added CM-capacitance and $X_4 = 31.1$

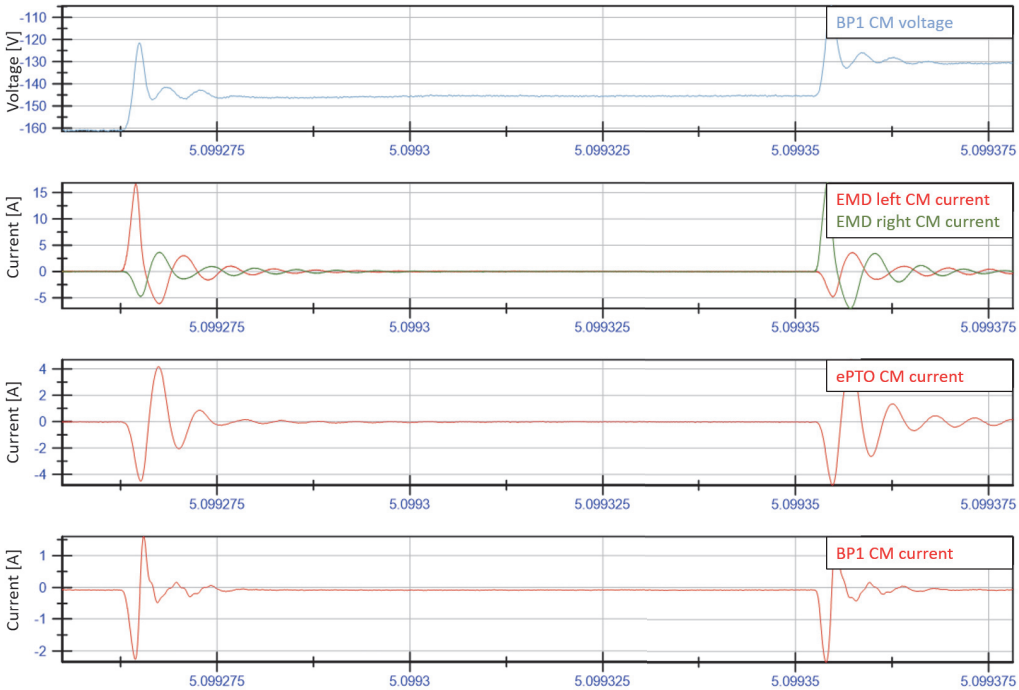

Figure 6.8: Original configuration with $X_3 = 11.5$

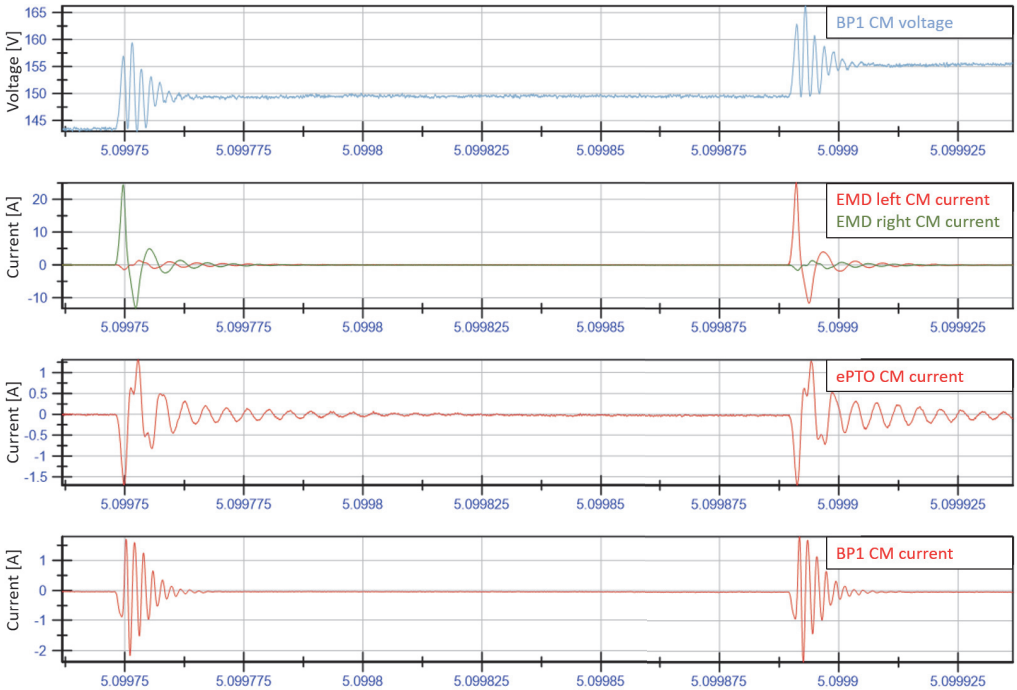

Figure 6.9: Configuration with added CM-capacitance and $X_4 = 31.1$

6.1.2 CMDC voltage and current elimination at simultaneous 180° phase shifted switching.

Unless the modulation of two EMD's are intentionally synchronized, it is likely that the two converters are not synchronized in terms of switching. In the previous subsection 6.1.1 it was shown that the upper and lower EMD are not switching at the same time. Looking at the CM currents for the right EMD, left EMD and the ePTO EMD, with reference to figure 6.1 for a time period of approximately 8 seconds, see figure 6.10, it is shown that the switching is drifting between the left and right EMD.

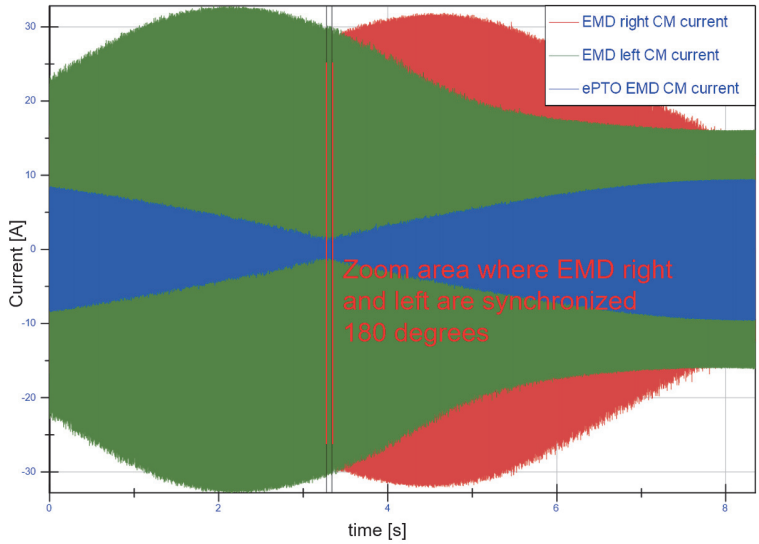

Figure 6.10: Current in the right EMD, left EMD and ePTO EMD according to figure 6.1. The ePTO EMD is not switching. The left and right EMD is switching where the phase shift is drifting. At the cursor the phase shift is is 180°. The marked area with the two red cursors can be found in the zoomed figure 6.11

The area for the cursor is expanded in figure 6.11 where the right and left EMD is switching 180° phase shifted. This results to that the CM current in the system is ”eliminated” as the asymmetric switching for the two EMDs will cancel out. The switching is according to figure 6.3 and 6.4

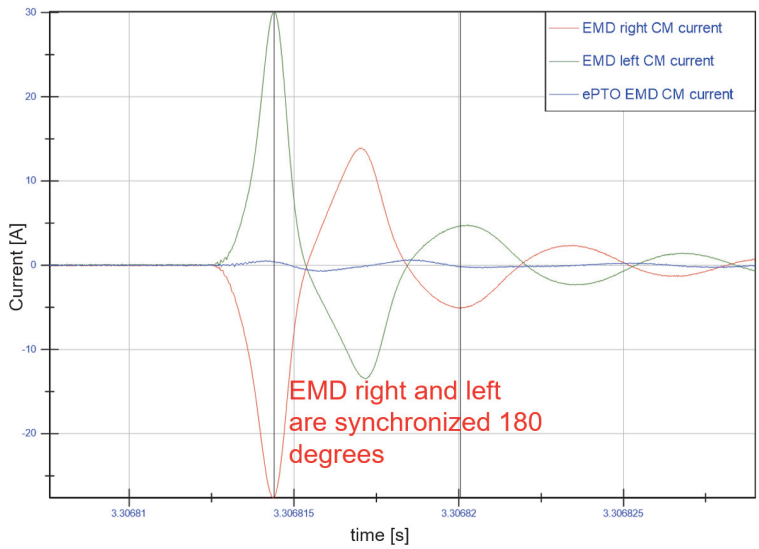

Figure 6.11: Both converters are switching simultaneous 180° phase shifted and the resulting CM current in the ePTO EMD is almost 0.

This is an optimal switching synchronization at zero voltage as the CM disturbances is as low as it can be with varied switching pattern.

6.1.3 Measured CM current maximum due to simultaneous switching in phase.

Looking at the CM currents for the right EMD, left EMD and the ePTO EMD, with reference to figure 6.1 for a time period of approximately 8 seconds, see figure 6.12

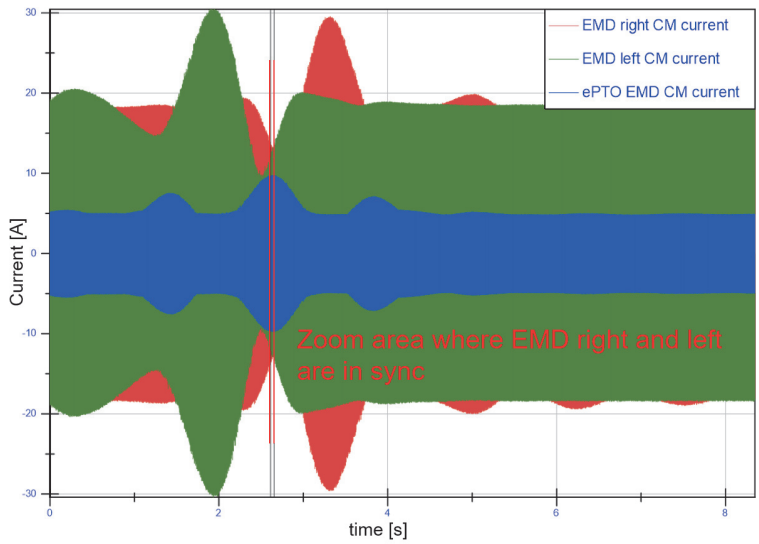

Figure 6.12: Current in the right EMD, left EMD and ePTO EMD according to figure 6.1. The ePTO EMD is not switching and the left and right EMD are switching synchronized.

The area for the cursor is expanded in figure 6.13 where the right and left EMD is synchronized. This results to that the CM current in the system is increased as the two converters are performing maximum asymmetry at the same time. The switching is according to figure 6.2 and 6.5

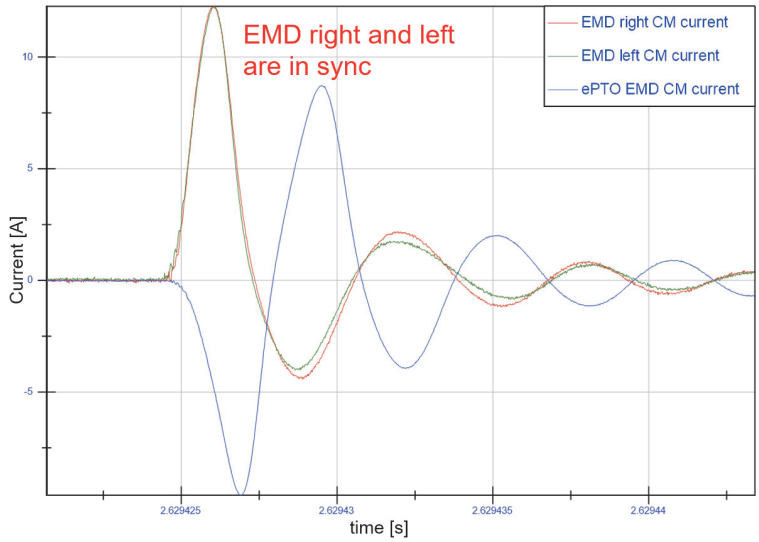

Figure 6.13: Both converters are switching synchronized and the resulting CM current in the EMD is as high as it can be.

6.1.4 Conclusion from the CM measurements.

It is shown that the CMDC voltage can be varied by the factor X and that it is crucial for the CM current in the system. It is also shown that the theoretical dependency for the CMDC voltage and factor X can be proven by measurements.
The timing of switching is of importance. If the synchronization is performed properly the switched asymmetry can be eliminated and the CM currents reduced to a minimum. In the other hand if the switching is done randomly, the switching will maximized at some times or even worse, all the time.

Chapter 7

Conclusion and recommendations

7.1 Conclusions

In addition to the conclusions given at the end of each chapter, this section provides a shorter and overall summary. Firstly, my own reflection is that the depth of this thesis is the width. At least for the author the normal research is more in the depth, investigation in all details rather than the holistic view. Reaching this point, it is clear that as soon as one thing is investigated in the holistic view, it is more or less required to go in details. One example is the simulations. System simulations are in general simulated with ideal switches and ideal components. But if the CM shall be simulated, it is required with a detailed model and switches that behaves like real semiconductors. Suddenly the scope is wide and deep! Another example is the measurements system. Looking at performance during driving requires many channels and extensive recording time. The CM recordings requires high sampling rate.

When the simulation models are developed with high accuracy and merged to a vehicle system in the simulation program, it is more or less impossible to run the simulation due to the complexity. Understanding of what is critical to have and not to include in the system simulation is crucial. But also, how to decrease the complexity of the models without affecting the desired results.

Interesting finding to highlight is the importance of introducing a non-perfect ground plane in the simulation model. The ground plane has higher impedance than the shield in the coaxial or twin axial cables. If this is not considered in the simulations, the results will be misleading.

The CMDC voltage and the relation of CM current in the loop of the EMD-EM vs. system is clear. A symmetrical CM capacitor has to be located close to the asymmetrical parasitic capacitances, i.e., the parasitic capacitance in the electric machine. The ratio X

between the said capacitances shall be kept as high as possible, a target of 50 is a recommended value.

7.2 Discussion

As the topic of EMC and EMI is not a black and white science, it is hard to get design rules. Projects want to have clear choices. ” If we don´t implement the improvement, what is the risk and cost of failure?”. System standards on conducted EMI is rare, at least not found by the author. Subsystems are sometimes sourced from suppliers which make a change more difficult and expensive, but otherwise the improvements do not have to be expensive at all. But for sure, it is expensive to solve after the problem occurred.

7.3 Future work

Firstly - measurements and more measurements on different vehicles. It is crucial that the findings in this thesis is repeatable in other vehicles.
Secondly - to decrease the complexity of the models. At this time a set of simulation has been running for a week with DM simulations with varied duty cycles and other parameters varied. Each simulation takes approximately 30hours. The beauty with simulations is to get a fast response.

Appendix A

Simulation tools - Zview, PLECS and Matlab

To build models, tools in terms of software are required besides the measurement equipment. The two main tools used in this thesis are, PLECS [20] and Zview [27]. PLECS is used to model the system and Zview is used to derive the parameters in the models.

A.1 How to derive the parameters in the models from measurements with Zview

Zview is a tool to derive parameters from measurements. When a component is measured with the LCR meter and an impedance and phase vs. frequency is achieved, the measurements has to be transferred to a model. In this section one example will be shown for a measurement on a capacitor. An equivalent model of a capacitor is shown in figure A.1.

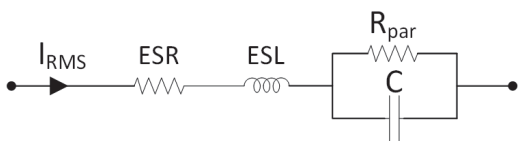

Figure A.1: Equivalent model of a capacitor.

An example of impedance and phase vs. frequency measurement is shown in figure A.2. In this graph a clear resonance point is found at around 1MHz. Before the resonance point the graph is capacitive and after it is inductive. In higher frequencies above 10MHz, new resonances is found in the graph but cannot be found in the model. As described in chapter 3 it is hard to get measurements correct and thereby models accurate above 10MHz.

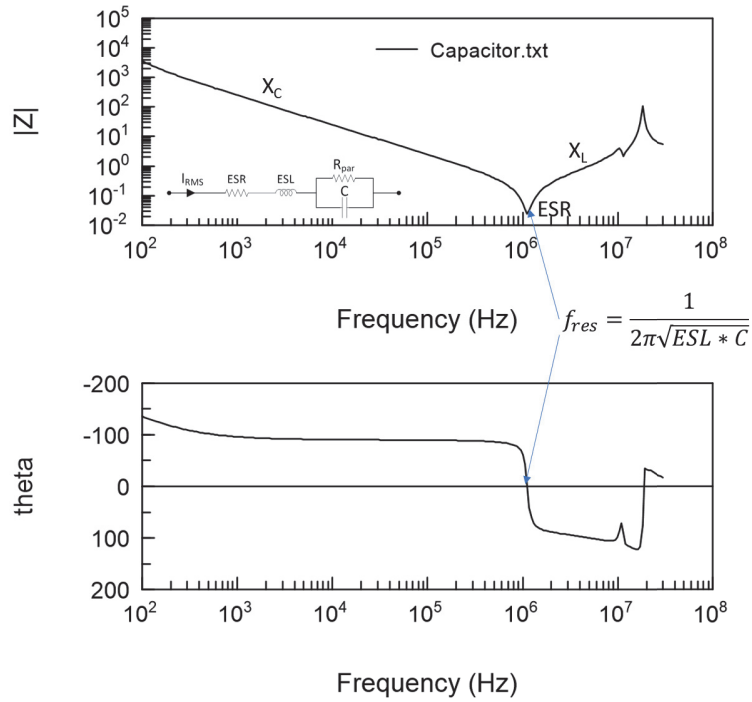

Figure A.2: Measured capacitor with a frequency sweep from 100Hz - 30MHz.

Start with Zview to find the parameters. The model is built in Zview according to figure A.3. Zview is set to "run fitting" in the frequency range 100Hz -10MHz and a simulation was performed. The equivalent parameters that responds to the equivalent circuit is found below the circuit.

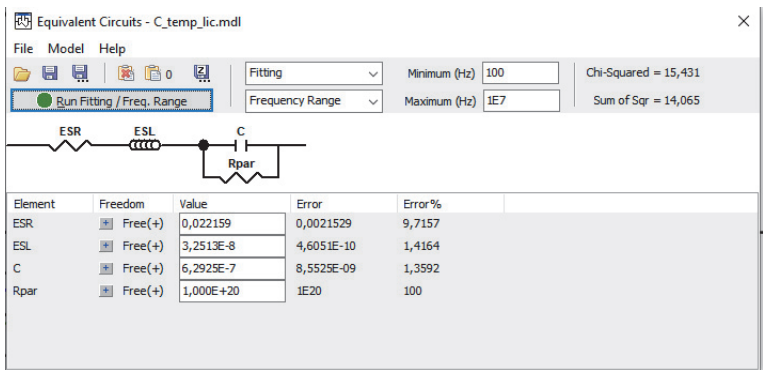

Figure A.3: Equivalent model in Zview with the parameters that responded to the "run fitting"

The resulting graph can be shown together with the measured graph which is shown in figure A.4 and a simulation up to 30MHz in figure A.5. To get the later graph Zview

needs to be set to simulation, otherwise it will try to fit the resonances as well. In the lower frequencies the LCR meter is not accurate as described in 3.1.3. For frequencies above 1kHz it is more or less a perfect match up to 10MHz.

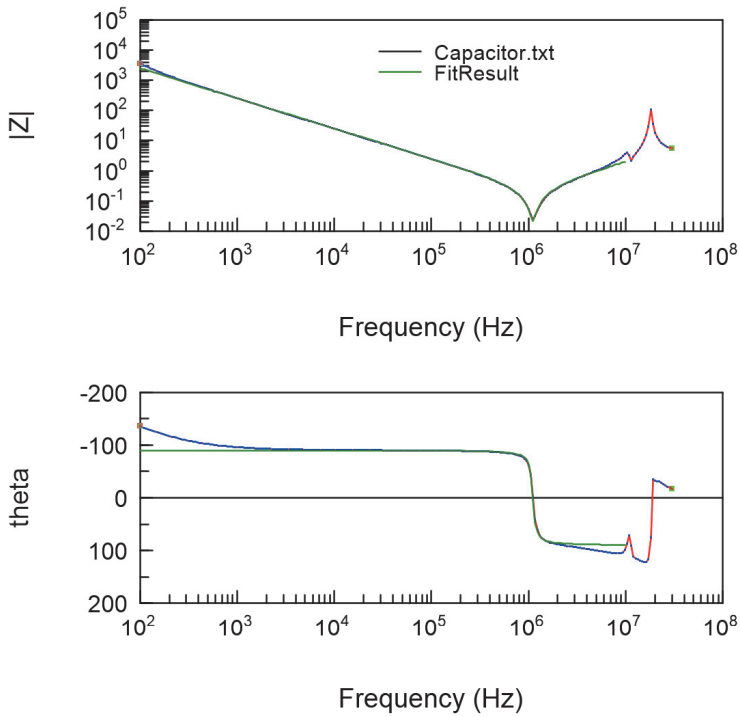

Figure A.4: Equivalent model simulated and shown together with the measured values."

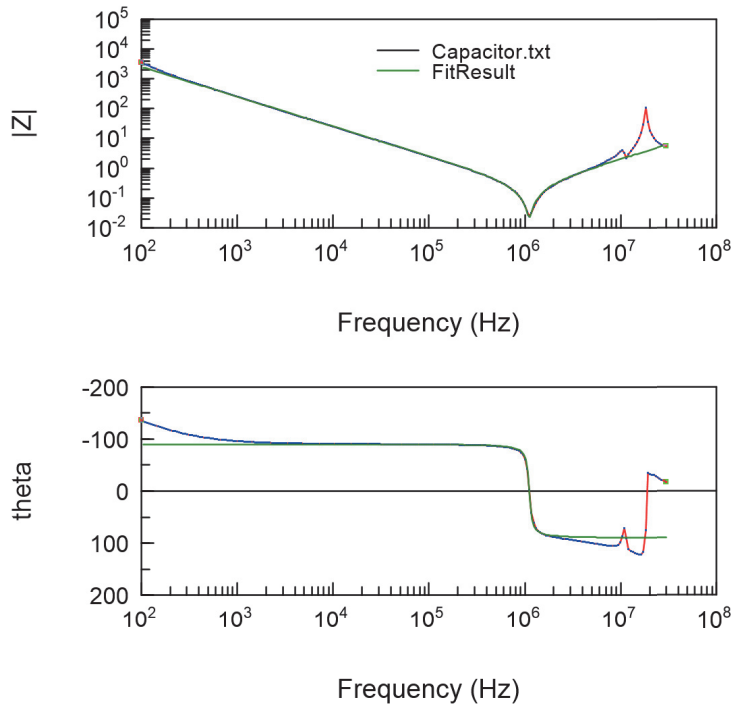

Figure A.5: Equivalent model simulated up to 30MHz and shown together with the measured values."

A.2 System simulation tool - PLECS

The simulation software PLEXIM's PLECS standalone [20] is used in this report. PLECS is possible to run inside the Matlab/Simulink environment but can also be used as a separate tool, hence called "standalone". PLECS is chosen for the user friendly interface in system simulations. In the real simulation work compromises have to be made on the complexity of the sub system models in order to make the whole system simulation run. PLECS prefers to simulate systems with ideal semiconductors. It has the possibility to store the models developed in a library and use them as templates. Frequency sweep measurements can also be performed and is a good tool for comparison with the subsystems measurements with the LCR meter. Scripting is possible to perform subsequent simulations with changed parameters.

A.3 Matlab

Matlab has only been used to plot graphs. Where measured data and simulated data is shown in the same graph, matlab is the tool to combine the data in the same graph.

References

[1] Mats Alaküla, Per Karlsson and Hans Bängtsson. *Power Electronics Devices, Converters, Control and Applications*. 2019th ed. 2019. URL: https://www.iea.lth.se/kel/2020/Power%20Electronics%202019.pdf.

[2] Sabine Alexandersson. 'Automotive Electromagnetic Compatibility Prediction and Analysis of Parasitic Components in Conductor Layouts'. In: (). URL: http://www.iea.lth.se.

[3] Alexander Bessman et al. 'Aging effects of AC harmonics on lithium-ion cells'. In: *Journal of Energy Storage* 21 (Feb. 2019), pp. 741–749. ISSN: 2352-152X. DOI: 10.1016/J.EST.2018.12.016. URL: https://www.sciencedirect.com/science/article/pii/S2352152X18307035.

[4] *COMSOL Multiphysics® Software - Understand, Predict, and Optimize*. URL: https://www.comsol.com/comsol-multiphysics.

[5] Alan Cordic and Azka Wanitwijan. 'Cable modelling for electric vehicle drivetrains'. In: (2020). URL: https://odr.chalmers.se/handle/20.500.12380/304256.

[6] Pearson Electronics. *PEARSON CURRENT MONITOR MODEL 2877*. 1999. URL: http://pearsonelectronics.com/pdf/2877.pdf.

[7] Norbert Hanigovszki et al. 'An EMC evaluation of the use of unshielded motor cables in AC adjustable speed drive applications'. In: *IEEE Transactions on Power Electronics* 21 (1 2006), pp. 273–280. ISSN: 08858993. DOI: 10.1109/TPEL.2005.861182.

[8] National Instruments. *Acquiring an Analog Signal: Bandwidth, Nyquist Sampling Theorem, and Aliasing*. 2016. URL: http://download.ni.com/evaluation/pxi/Acquiring_Analog_Signal.pdf (visited on 27/09/2021).

[9] National Instruments. *SPECIFICATIONS PXIe-5105*. URL: https://www.ni.com/pdf/manuals/374398d.pdf (visited on 22/09/2021).

[10] ISO. *Electrically propelled road vehicles – Safety specifications –Part 3: Electrical safety (ISO 6469-3:2018, IDT)*. URL: https://www.sis.se/api/document/get/80007276.

[11] ISO. *ISO - ISO 6469-3:2018/Amd 1:2020 - Electrically propelled road vehicles — Safety specifications — Part 3: Electrical safety — Amendment 1: Withstand voltage test for electric power sources*. 2011. URL: https://www.iso.org/standard/76885.html (visited on 18/05/2021).

[12] ISO. *Standard - Electrically propelled road vehicles - Conductive power transfer - Safety requirements (ISO 17409:2020) SS-EN ISO 17409:2020 - Swedish Institute for Standards, SIS*. Mar. 2020. URL: https://www.sis.se/en/produkter/road-vehicles-engineering/electric-road-vehicles/ss-en-iso-174092020/.

[13] Avinash Kishore et al. 'Investigation of common mode noise in electric propulsion system high voltage components in an electrified vehicle'. In: *2016 IEEE Transportation Electrification Conference and Expo, ITEC 2016* (July 2016). DOI: 10.1109/ITEC.2016.7520263.

[14] M Moon et al. 'Modeling and analysis of return paths of common mode EMI noise currents from motor drive system in hybrid electric vehicle'. In: 2015, pp. 82–85.

[15] Newtons4th. *IAI2 Impedance Analyzer - 10uHz to 50MHz*. URL: https://www.newtons4th.com/products/impedance-analysis-interface-2/.

[16] Newtons4th. *PSM3750 Frequency Response Analyzer: 10μHz–50MHz – High Performance - Newtons 4th | Power Analyzers and Frequency Analyzers*. URL: https://www.newtons4th.com/products/frequency-response-analyzers/psm3750/.

[17] Satoshi Ogasawara and Hirofumi Akagi. 'Modeling and damping of high-frequency leakage currents in PWM inverter-fed AC motor drive systems'. In: *Conference Record - IAS Annual Meeting (IEEE Industry Applications Society)* 1 (1995), pp. 29–36. ISSN: 01972618. DOI: 10.1109/IAS.1995.530280.

[18] M C Di Piazza, G Tine and G Vitale. 'An Improved Active Common-Mode Voltage Compensation Device for Induction Motor Drives'. In: *IEEE Transactions on Industrial Electronics* 55 (4 2008), pp. 1823–1834.

[19] Maria Carmela Di Piazza, Antonella Ragusa and Gianpaolo Vitale. 'Effects of common-mode active filtering in induction motor drives for electric vehicles'. In: *IEEE Transactions on Vehicular Technology* 59 (6 July 2010), pp. 2664–2673. ISSN: 00189545. DOI: 10.1109/TVT.2010.2047661.

[20] PLEXIM. *PLECS Standalone | Plexim*. URL: https://www.plexim.com/products/plecs/plecs_standalone.

[21] Stefan Quabeck, Vivien Grau and Rik W. De Doncker. 'Modeling and Mitigation of Bearing Currents in Electrical Traction Drives'. In: Institute of Electrical and Electronics Engineers Inc., Nov. 2020, pp. 1101–1106. ISBN: 9784886864192. DOI: 10.23919/ICEMS50442.2020.9290879.

[22] *RIFEL - Ripple and Electromagnetic Fields in Electric Vehicles*. URL: https://research.chalmers.se/publication/504008#.

[23] Michele Sclocchi. 'Input Filter Design for Switching Power Supplies'. In: (2010). URL: www.national.com.

[24] TESTEC. *Instruction manual Testec - Differential probe TT-SI 9010*. 2021. URL: https://www.testec.de/en/assets/pdf/TT-SI/TT-SI-9010_Manual_EN.pdf (visited on 23/09/2021).

[25] Per Widek and Mats Alakula. 'Modeling of electric power system in electric vehicles'. In: Institute of Electrical and Electronics Engineers Inc., June 2020, pp. 293–298. ISBN: 9781728170190. DOI: 10.1109/SPEEDAM48782.2020.9161884.

[26] Per Widek and Mats Alaküla. 'CM current measurements in traction systems for electric vehicles'. In: *Under review for possible publication in IEEE* ().

[27] *ZView® For Windows - Scribner Associates*. URL: https://www.scribner.com/software/68-general-electrochemistr376-zview-for-windows/.

Printed by Media-Tryck, Lund 2022 NORDIC SWAN ECOLABEL 3041 0903

Lund University
Faculty of Engineering
Department of Biomedical Engineering
Division of Industrial Electrical Engineering and Automation

ISBN: 978-91-985109-2-8 (print)
ISBN: 978-91-985109-3-5 (pdf)
CODEN: LUTEDX/(TEIE-1094)/1-125/(2022)